Development of Novel Naphthobischalcogenadiazole-based Polymers and Their Application for Organic Photovoltaics

（新規ナフトビスカルコゲナジアゾール系ポリマーの創製と有機薄膜太陽電池への応用）

March, 2016

Kazuaki Kawashima

Department of Applied Chemistry, Graduate School of Engineering

Hiroshima University

Contents

Chapter 1

General Introduction

1-1. Semiconducting polymers

There have been intensive research activities on the development of organic semiconducting materials in the field of organic electronics. In particular, semiconducting polymers are attracting considerable attention owing to their use as cost-effective, light-weight and flexible electronic and optoelectronic device applications, including organic light-emitting diodes (OLEDs),[1] organic photovoltaics (OPVs),[2] organic field-effect transistors (OFETs),[3] and polymeric sensors.[4] Moreover, they allow an easier and a better modification of the polymer′s functional properties by making small structural changes in molecular/monomeric units, unlike typical inorganic materials.[5] Indeed, these properties are dependent not only on the nature of the polymeric backbone but also on the presence of covalently attached functional groups.

For the past fifty years, inorganic semiconductors such as silicon and gallium arsenide silicon dioxide insulators, and metals such as aluminum and copper have been the backbone of the semiconductor industry.[6] However, in 1977, Shirakawa, MacDiarmid and Heeger et al. reported the first high conducting polymer, chemically doped polyacetylene,[7, 8] which demonstrated that polymers could be used as electrically active materials as well. They received the 2000 Nobel Prize in Chemistry for "The discovery and development of conductive polymers". From that milestone, a great deal of reaearch activities on conjugated organic materials have been developed all over the world. In the earlier time, the performance, proceaasbility and stability of organic semiconductors were very poor. However, since poly(p-phenylenevinylene) (PPV)[9] and polythiophenes[10] were reported and drastically improved in the synthesis and processing of new classes of molecular materials in the 1990s, the prospects of commercially applications like OLEDs, OFETs and OPVs are now greater than ever. To date, OLEDs have become commercially available with good performance, and OPVs have reached high efficiency, over 10% in lab-scale devices.[11-14] Simplicity in manufacturing and lower costs of organic devices have been the primary

reasons driving these devices towards commercialization.

1-2. Organic photovoltaics

OPVs have promising potential to offer clean and renewable energy due ease of fabricating them onto large areas of lightweight flexible substrates by solution processing at a low cost.[15] However, the power conversion efficiency (PCE) of these cells is very low as compared to inorganic devices due poor charge carrier generation and unbalanced charge transport.[16] So, it is necessary to understand basic principles of process of charge transfer in organic photovoltaic cell and develop new organic materials to achieve high efficiencies. The fundamental mechanism of organic photovoltaic cells is shown the next section.

1-3. Fundamental mechanism of OPV[17-19]

In an OPV device, carriers can only be collected at their corresponding electrodes, meaning that only one direction of current flow is allowed. Therefore, a photovoltaic device behaves like a diode and has J–V characteristics as Figure 1-1. Photovoltaic parameters of devices are extracted from the J–V characteristics.
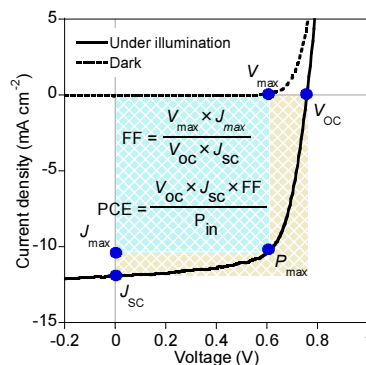

Figure 1-1. J–V characteristics of photovoltaic device.

The short circuit current density (J_{SC}), open circuit voltage (V_{OC}), and fill factor (FF) of the devices are indicated in the Figure 1-1. J_{max} and V_{max} used in the calculation of FF are the current density and voltage

values with maximum $J \times V$ on the J–V curve. The PCE of the OPVs is proportional to J_{SC}, V_{OC}, and FF, where the energy of incident light (P_{in}) is usually 100 (mW) *i.e.*, 1 sun, in case of AM 1.5G. In this case, PCE is determined by the following equal 1.

$$PCE~(\%) = J_{SC} \times V_{OC} \times FF ~~ \cdot ~ \cdot ~ \cdot ~ (1)$$

In OPV cells, sunlight is absorbed by the photoactive layers composed of donor (p-type) and acceptor (n-type) organic semiconducting materials to generate photocurrents. The p-type material donate electrons and transports holes, and the n-type material accept electrons and transports electrons. As shown in Figure 1-2, fundamental mechanism of photoelectric conversion can be divided into five processes; (1) light absorption and exciton generation, (2) excitons diffusion to the p/n interface, (3) charge transfer and exciton dissociation, (4) charge transport of holes and electrons through p- and n-phase, respectively (5) charge extraction at the respective electrodes interfaces. Therefore, the improvement of the efficiency of these fundamental processes leads to the improvement of overall PCE of the corresponding cell.
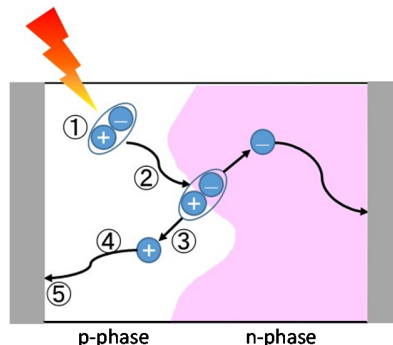
Figure 1-2. Schematic illustration of photoelectric conversion in OPVs.

1-3-1. Guiding principles for the efficiency improvement by tuning the electronic structure

The J_{SC} depends on the efficiencies of the light absorption of the active layer, the rate of the photogenerated charge separation process, and suppression of the recombination of hole and electron. Widening the range of absorption wavelengths is proposed, to increase absorbance. So far poly(3-hexylthiophene-2,5-diyl) (P3HT) has been a commonly used p-type semiconductor material. However,

P3HT absorbs wavelengths of up to about 650 nm, so that the incident light with long wavelengths is not used effectively for power generation. Thus, investigation of polymers with long wavelength absorption, *i.e.*, the polymers with narrow bandgap is necessary to obtain high J_{SC}. For this purpose, polymers were designed by placing electron rich (donor) and poor (acceptor) units alternately in a polymer chain. Such a configuration causes frontier orbital mixing, reducing the bandgap, which in turn enables the polymers to absorb longer wavelength irradiation.

V_{OC} is mostly proportional to the energy level difference (ΔE_{HL}) between the highest occupied molecular orbital (HOMO) of the p-type material and the lowest unoccupied molecular orbital (LUMO) of the n-type material.[20] For the purpose of increasing V_{OC}, the development of p-type semiconductor materials with a deep HOMO level and n-type semiconductor materials with a shallow LUMO level are required.

FF is related to the series and parallel resistances of the devices. Utilizing high carrier mobility materials in the active layer, decreasing the resistance at the interface of each layer, and increasing the parallel resistance of PV equivalent circuits by removing defects in layers are all effective in increasing the FF value.

The J_{SC} and V_{OC} have been maximized by optimizing the energy level alignment and light absorption of the p-type and n-type materials. Recently, this has been refined in accordance with the state picture by replacing ΔE_{HL} with the energy of the charge transfer (CT) state, E_{CT}, which contains information on the structures at the p/n interfaces and the relaxation of the charged molecular structures.[21-23] The energy difference (ΔE_{LL}) between the LUMOs of the p-type materials and the n-type serves as the main driving force for CT, and $\Delta E_{LL} \geq 0.3$ eV is necessary to keep this process efficient.[20] Therefore, when the energy levels of the materials are manipulated, the compromise between ΔE_{HL} and ΔE_{LL} leads to the trade-off between J_{SC} and V_{OC} in OPVs, which ultimately limits device performance.[24, 25] Therefore, molecular designers/synthetic chemists are required to carefully control both the HOMO and LUMO energy levels of the polymers.
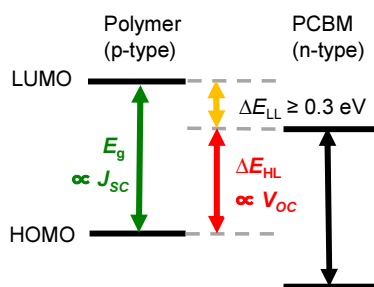
Fig 1-3. Schematic energy diagram of a polymer/PCBM system.

1-3-2. Charge transport[26]

One of the most important functions of semiconducting polymers is charge carrier transport, which largely influences the OPV performances. Charge carrier transport in semiconducting polymer thin films is apparently governed by an intramolecular pathway along the π-conjugated backbone and an intermolecular pathway along the $\pi-\pi$ overlaps between the face-to-face $\pi-\pi$ stacked backbones.[27] Therefore, in order to promote the efficient charge carrier transport, the backbones must be as co-planar as possible and as closely $\pi-\pi$ stacked each other as possible.[28, 29] which is referred to as a high crystalline structure. On the other hand, as OPV has a vertically stacked structure, carrier transport of out-of-plane direction to the substrate plane is necessary.[30] Thus, the direction of the backbone $\pi-\pi$ stacking is desired to be normal to the substrate plane, *i.e.*, the backbone lies flat on the substrate plane, which is so-called "face-on" orientation (Figure 1-4b). In addition, a structure with the $\pi-\pi$ stacking is parallel to the substrate plane is called "edge-on" orientation (Figure 1-4a), which facilitates the in-plane carrier transport and thus suitable for OFETs.[27]
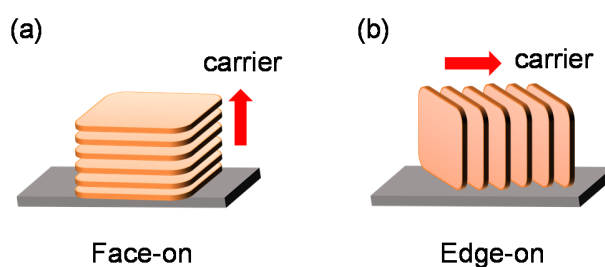

Figure 1-4. Schematic structures of polymer orientation, face-on orientation (a) edge-on orientation (b).

1-3-3. Development of semiconducting polymers

Taking into account the above-mentioned working mechanism of OPVs, the following four properties should be kept in mind when designing semiconducting polymers.

(1) Narrow E_g

(2) Deep HOMO energy level

(3) High crystallinity

(4) Face-on orientation

The use of electron-rich (donor; D) and electron-poor (acceptor; A) units to form donor−acceptor (D−A) backbone is a promising strategy to develop such polymers. A number of electron-rich groups, which consist of thiophene- and/or related heteroaromatic-based substructures have been explored and developed and employed in the D-A polymer. Compared to the D units, on the other hand, the number of A units are relatively limited: for example, 2,5-diketopyrrolo[3,4-c]-pyrrole-1,4-dione (DPP),[31-33] benzo[c]-[1,2,5]thiadiazole (BTz),[34-36] thiazolo[5,4-d]thiazole (TzTz),[37, 38] thieno[3,4-c]pyrrole-4,6-dione (TPD),[39, 40] 1,4,5,8-naphthalenedicarboximide (NDI),[41] and so on (Figure 1-5). Therefore, the development of novel A units incorporated in the polymer backbone is a crucial issue.
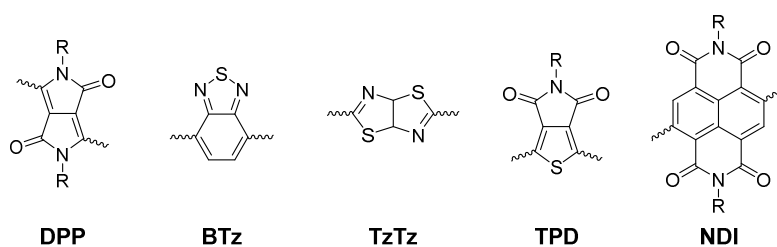
Figure 1-5. Typical π-electron deficient building units.

1-4. Naphtho[1,2-c:5,6-c′]bis[1,2,5]chalcogenadiazole (NXz)

Naphtho[1,2-c:5,6-c′]bis[1,2,5]thiadiazole (NTz)[42] can be viewed as a doubly BTz-fused tetracyclic system and classified into heteroaromatic-fused compounds. In fact, 1,2,5-thiadiazole fused in the NTz framework is of isoelectronic structure with thiophene, the most frequently used heteroaromatic

compound, and interestingly the aromaticity of 1,2,5-thiadiazole is known to be greater than that of thiophene.[43] The electronic nature of 1,2,5-thiadiazole, however, is strikingly different from that of thiophene, owing to the presence of two electron deficient nitrogen atoms similar to that in pyridine. As a result, the calculated energy levels of 1,2,5-thiadiazole (E_{HOMO}: –6.53 eV, E_{LUMO}: –2.30 eV) are lower than those of thiophene (E_{HOMO}: –6.34 eV, E_{LUMO}: –0.21 eV), and in particular the LUMO energy level of the former is markedly stabilized. The theoretical calculations also predict that the dipole moment of 1,2,5-thiadiazole (1.54 Debye) is significantly larger than that of thiophene (0.63 Debye). These electronic characteristics of 1,2,5-thiadiazole contribute to the unique properties of NTz in combination with its planar and centrosymmetric C_{2h} molecular structure: e.g., low-lying HOMO and LUMO energy level (E_{HOMO}: –6.45 eV, E_{LUMO}: –2.85 eV, theoretical calculations), locally polarizable nature, and pseudo quinoidal structure in the naphthalene moiety. All these characteristics of NTz can be useful in the development of electronic materials, in particular semiconducting polymers. In addition, replacement of the sulfur atom of NTz by the oxygen and selenium atoms, resulting in naphtho[1,2-*c*:5,6-*c'*]bis[1,2,5]oxadiazole (NOz) and naphtho[1,2-*c*:5,6-*c'*]bis[1,2,5]selenadiazole (NSz) is also expected similar effect to that of NTz (Figure 1-6).
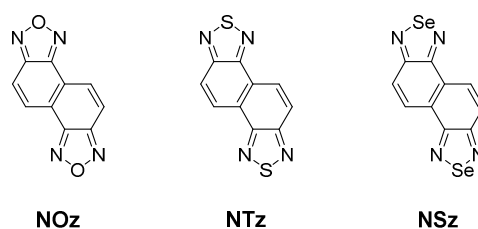
Figure 1-6. Chemical structures of naphthobischalcogenadiazoles (NXz). NOz = naphtho[1,2-*c*:5,6-*c'*]bis[1,2,5]oxadiazole, NTz = naphtho[1,2-*c*:5,6-*c'*]bis[1,2,5]thiadiazole, NSz = naphtho[1,2-*c*:5,6-*c'*]bis[1,2,5]selenadiazole.

1-5. This thesis

In this thesis, I will describe the design and synthesis of a series of naphthobischalcogenadiazole (NXz)-based semiconducting polymers and their application to the organic solar cells (OPVs). This thesis

consists of five chapters including the general introduction as chapter 1 and concluding remarks as chapter 5.

In chapter 2, I focus on NTz-based polymer (PNTz4T), which has been originally developed in our group in 2012. PNTz4T shows highly crystalline structure and face-on orientation and PCE of 6.3%. I aimed to synthesize PNTz4T by a Suzuki-Miyaura coupling reaction. I also aimed at the further improvement of performance by careful control of processing conditions and device architectures to well-match the backbone orientation.
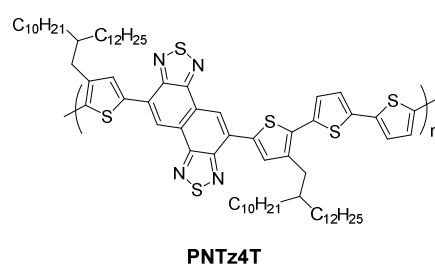
Figure 1-7. Chemical structure of PNTz4T.

In chapter 3, I show the synthesis of PNTz4T with fluorine atoms on thiophenes (PNTz4TF2 and PNTz4TF4), to obtain deep HOMO level and thus high V_{OC} as compared to PNTz4T. I discuss the effect of the fluorine substitutions on the properties of polymers and OPV performance.
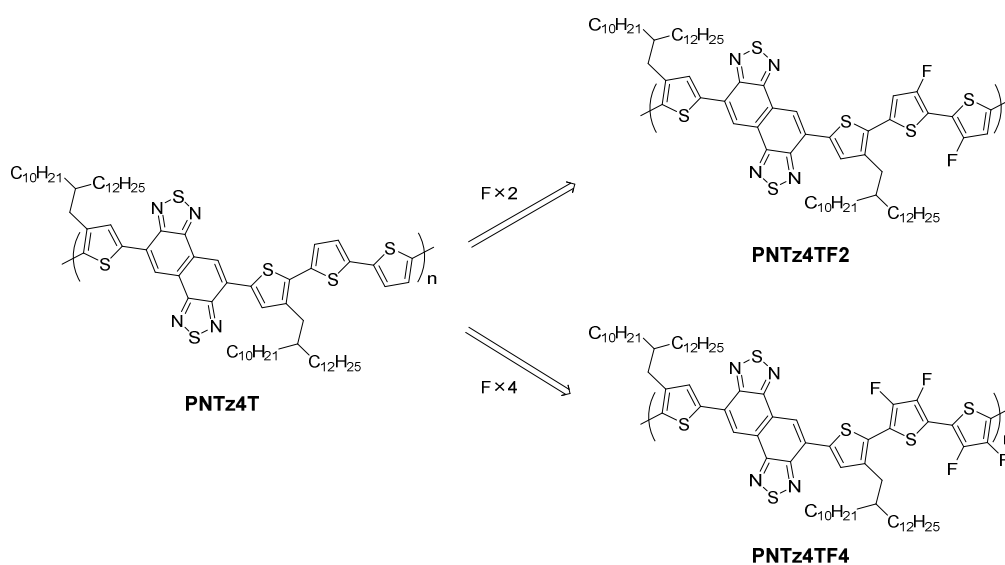
Figure 1-8. Chemical structures of PNTz4TF2 and PNTz4TF4.

In chapter 4, I focus on novel oxygen and selenium analogues of PNTz4T, namely PNOz4T and PNSz4T. I discuss the effect of chalcogen atom on the properties of polymers and device performance.

Figure 1-9. Chemical structures of PNOz4T and PNSz4T.

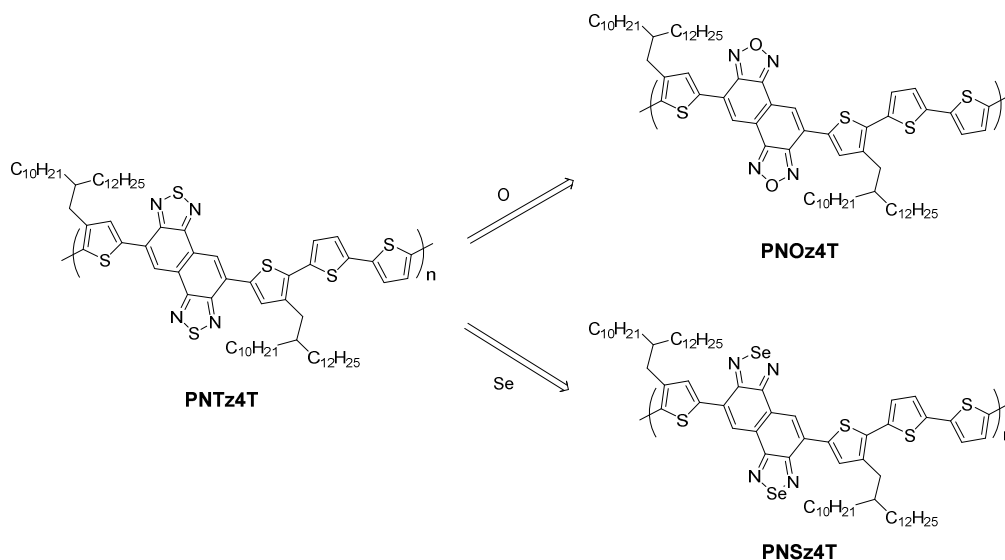In chapter 5, I will summarize this thesis and mention future perspectives.

1-6. References

1) Grimsdale, A. C.; Chan, K. L.; Martin, R. E.; Jokisz, P. G.; Holmes, A. B. *Chem. Rev.* **2009**, *109*, 897–1091.

2) Boudreault, P.-L. T.; Najari, A.; Leclerc, M. *Chem. Mater.* **2011**, *23*, 456–469.

3) Facchetti, A., *Chem. Mater.* **2011**, *23*, 733–758.

4) McQuade, D. T.; Pullen, A. E.; Swager, T. M. *Chem. Rev.* **2000**, *100*, 2537–2574.

5) Roncali, J. *Chem. Rev.* **1997**, *97*, 173–206.

6) Li, L.; Kosina, H. "Organic Electronics" Springer, *Adv. poly. Sci.* **2010**, *223*, 301–323.

7) Chiang, C. K.; Fincher, C. R.; Park, Y. W.; Heeger, A. J.; Shirakawa, H.; Louis, E. J.; Gau, S. C.; MacDiarmid, A. G. *Phys. Rev. Lett.* **1977**, *39*, 1098–1101.

8) Shirakawa, H.; Louis, E. J.; MacDiarmid, A. G.; Chiang, C. K.; Heeger, A. J. *J. Chem. Soc., Chem. Commun.*, **1977**, *16*, 578-580.

9) Burroughes, J. H.; Bradley, D. D. C.; Brown, A. R.; Marks, R. N.; Mackay, K.; Friend, R. H.; Burns, P. L.; Holmes, A. B. Nature, **1990**, *347*, 539–541.

10) Shaw, J. M.; Seidler, P. F. *IBM J. Res. Dev.*, **2001**, *45(1)*, 3–10.

11) Liao, S.-H.; Jhuo, H.-J.; Yeh, P.-N.; Cheng, Y.-S.; Li, Y.-L.; Lee, Y.-H.; Sharma, S.; Chen, S.-A. *Sci. Rep.* **2014**, *4*, 6813.

12) Liu, Y.; Zhao, J.; Li, Z.; Mu, C.; Ma, W.; Hu, H.; Jiang, K.; Lin, H.; Ade, H.; Yan, H. *Nat. Commun.* **2014**, *5*, 5293.

13) Chen, J.-D.; Cui, C.; Li, Y.-Q.; Zhou, L.; Ou, Q.-D.; Li, C.; Li, Y.; Tang, J.-X. *Adv. Mater.* **2015**, *27*, 1035–1041.

14) Liu, C.; Yi, C.; Wang, K.; Yang, Y.; Bhatta, R.-S.; Tsige, M.; Xiao, S.; Gong, X. *ACS Appl. Mater. Interfaces* **2015**, *7*, 4928–4935.

15) Kaltenbrunner, M.; White, M. S.; Glowacki, E. D.; Sekitani, T.; Someya, T.; Sariciftci, N. S.; Bauer, S. *Nat. Commun.* **2012**, *3*, 770.

16) Wohrle, D.; Meissner, D. *Adv. Mater.* **1991**, *3*, 129–138.

17) Li, Y. *Acc. Chem. Res.*, **2012**, *45*, 723–733.

18) Sekine, C.; Tsubata, Y.; Yamada, T.; Kitano, M.; Doi, S. *Sci. Technol. Adv. Mater.* **2014**, *15*, 034203.

19) Lu, L.; Zheng, T.; Wu, Q.; Schneider, A. M.; Zhao, D.; Yu, L. *Chem. Rev.* **2015**, *115*, 12666–12731.

20) Scharber, M. C.; Muhlbacher, D.; Koppe, M.; Denk, P.; Waldauf, C.; Heeger, A. J.; Brabec, C. J. *Adv. Mater.* **2006**, *18*, 789–794.

21) Vandewal, K.; Tvingstedt, K.; Gadisa, A.; Inganäs, O.; Manca, J. V. *Nat. Mater.* **2009**, *8*, 904–909.

22) Veldman, D.; Meskers, S. C. J.; Janssen, R. A. J. *Adv. Funct. Mater.* **2009**, *19*, 1939–1948.

23) Zhong, Y.; Tada, A.; Izawa, S.; Hashimoto, K.; Tajima, K. *Adv. Energy. Mater.* **2014**, *4,* 1301332.

24) Hoke, E. T.; Vandewal, K.; Bartelt, J. A.; Mateker, W. R.; Douglas, J. D.; Noriega, R.; Graham, K.

R.; Frechet, J. M. J.; Salleo, A.; McGehee, M. D. *Adv. Energy Mater.* **2013**, *3*, 220–230.

25) Nuzzo, D. D.; Wetzelaer, G.-J. A. H.; Bouwer, R. K. M.; Gevaerts, V. S.; Meskers, S. C. J.; Hummelen, J. C.; Blom, P. W. M.; Janssen, R. A. J. *Adv. Energy Mater.* **2013**, *3*, 85–94.

26) Osaka, I.; Takimiya, K. *Polymer* **2015**, *59*, A1–A15.

27) Sirringhaus, H.; Brown, P.; Friend, R.; Nielsen, M. *Nature*, **1999**, *401*, 685–688.

28) McCullough, R. D.; Tristram-Nagle, S.; Williams, S. P.; Lowe, R. D.; Jayaraman, M. *J. Am. Chem. Soc.* **1993**, *115*, 4910–4911.

29) McCullough, R. D. *Adv. Mater.* **1998**, *10*, 93–116.

30) Guo, J.; Liang, Y.; Szarko, J.; Lee, B.; Son, H.-J.; Rolczynski, B. S.; Yu, L.; Chen, L. X. *J. Phys. Chem. B*, **2010**, *114*, 742–748.

31) Nielsen, B.; Turbiez, M.; McCullich, I. *Adv. Mater.* **2013**, *25*, 1859−1880.

32) Li, W.; Hendriks, K. H.; Roelofs, W. S. C.; Kim, Y.; Wienk, M. M.; Janssen, R. A. J. *Adv. Mater.* **2013**, *25*, 3182−3186.

33) Homyak, P.; Liu, Y.; Liu, F.; Russel, T. P.; Coughlin, E. B. *Macromolecules* **2015**, *48*, 6978−6986.

34) Peet, J.; Kim, J. Y.; Coates, N. E.; Ma, W. L.; Moses, D.; Heeger, A. J.; Bazan, G. C. *Nat. Mater.* **2007**, *6*, 497−500.

35) Blouin, N.; Michaud, A.; Leclerc, M. *Adv. Mater.* **2007**, *19*, 2295−2300.

36) Zhang, M.; Gu, Y.; Guo, X.; Liu, F.; Zhang, S.; Huo, L.; Russell, T. P.; Hou, J. *Adv. Mater.* **2013**, *25*, 4944−4949.

37) Osaka, I.; Sauvé, G.; Zhang, R.; Kowalewski, T.; McCullough, R. D. *Adv. Mater.* **2007**, *19*, 4160−4165.

38) Osaka, I.; Saito, M.; Mori, H.; Koganezawa, T.; Takimiya, K. *Adv. Mater*, **2012**, *24*, 425-430.

39) Guo, X.; Ortiz, R. P.; Zheng, Y.; Kim, M.-G.; Zhang, S.; Hu, Y.; Lu, G.; Facchetti, A.; Marks, T. J. *J. Am. Chem. Soc.* **2011**, *133*, 13685−13697.

40) Cabanetos, C.; Labban, A. E.; Bartelt, J. A.; Douglas, J. D.; Mateker, W. R.; Fréchet, J. M. J.;

McGehee, M. D.; Beaujuge, P. M. *J. Am. Chem. Soc.* **2013**, *135*, 4656−4659.

41) Zhan, X.; Facchetti, A.; Barlow, S.; Marks, T. J.; Ratner, M. A.; Wasielewski, M. R.; Marder, S. R. *Adv. Mater.* **2011**, *23*, 268−284.

42) Mataka, S.; Takahashi, K.; Ikezaki, Y.; Hatta, T.; Tori-I, A.; Tashiro, M. *Bull. Chem. Soc. Jpn.* **1991**, 64, 68–73.

43) Balaban, A. T.; Oniciu, D. C.; Katritzky, A. R. *Chem. Rev.* **2004**, *104*, 2777–2812.

Chapter 2

Naphthobisthiadiazole-based polymer (PNTz4T)

2-1. Introduction

In the design and synthesis of D-A polymers, selection and combination of the respective donor (D) and acceptor (A) units are the key, and thus development of these units is one of the most important issues. In fact, a wide variety of D units, most of which consist of thiophene- and/or related heteroaromatic-based substructures, have been explored and/or developed and employed in the D-A polymers.[1-3]

Naphtho[1,2-*c*:5,6-*c'*]bis[1,2,5]thiadiazole (NTz), a doubly BTz-fused heteroaromatic, first reported by Mataka and co-workers in 1991,[4] is an emerging A unit for semiconducting polymers. In fact during the last two years, several NTz-based polymers, PBDT-DTNT,[5] PNTz4T,[6] and PNDT3NTz[7] (Figure 2-1), have been reported and proven to be promising semiconducting polymers both for OFET and OPV applications.

PBDT-DTNT

PNTz4T

PNDT3NTz
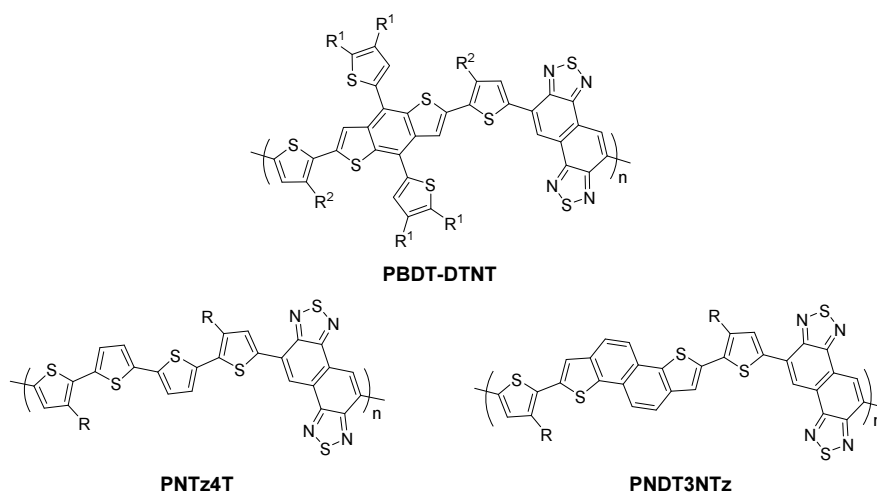
Figure 2-1. Structures of NTz-based polymers recently developed.

This chapter consists of two topics, all of which focus on PNTz4T: First, I have examined the Suzuki-Miyaura polymerization to prepare PNTz4T using 5,10-diboryalted NTz and the corresponding quaterthiophene derivatives and evaluated their optochemical properties and OFET characteristics (section 2-2).

13
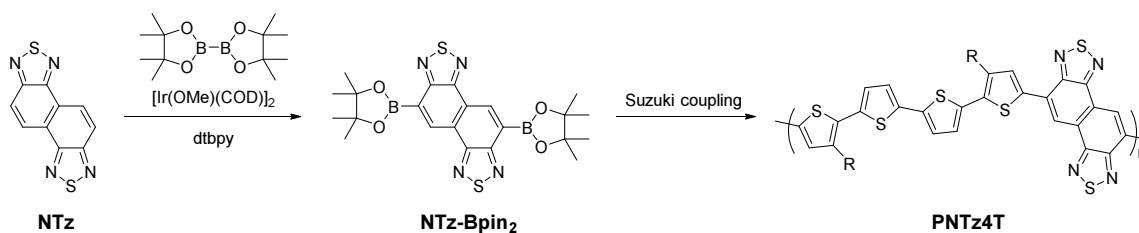
Scheme 2-1. Synthesis of PNTz4T using NTz-Bpin$_2$.

Next, I performed the further studies on the polymer solar cells (PSCs) using PNTz4T/PCBM. I demonstrated that a PCE of 10% has been achieved in a single-junction PSCs with an inverted architecture (section 2-3).

2-2. Synthesis of PNTz4T via Suzuki-Miyaura coupling

Synthesis of NTz-based polymers are generally carried out by consecutively using the Stille cross coupling reactions, where 5,10-dibromonaphtho[1,2-*c*:5,6-*c'*]bis[1,2,5]thiadiazole is first coupled with 2-(trialkylstannyl)thiophenes, followed by bromination at the thiophene α-positions, and then polymerized with other D units with trialkylstannyl functionalities via the Stille coupling reaction to produce the polymers (Scheme 2-2, Route A).

Although this approach allows us to develop a range of NTz-based polymers, the Stille coupling requiring organotin compounds as the key reagents is not amenable to industrial use and is also less environmentally friendly. In this context, the Suzuki-Miyaura coupling using organoboron compounds should be a favorable alternative. In fact, a number of conjugated polymers have been reported to be synthesized with the Suzuki-Miyaura polymerization.[8, 9] However, in contrast to the prevailing Stille polymerization reaction, the Suzuki-Miyaura polymerization has been less frequently employed for polythiophene-based semiconducting polymers. This is probably because that the boryl groups, particularly at the α-position of thiophene moiety, can easily be cleaved off during the polymerization reaction, which can reduce the yields and molecular weights of the desired polymers. To circumvent such

14

reductive deborylation, choice and combination of borylated and halogenated co-monomers in the Suzuki polymerization is crucial.

   With these backgrounds, I have examined the Suzuki-Miyaura polymerization to prepare PNTz4T using 5,10-diboryalted NTz and the corresponding quaterthiophene derivatives (Scheme 2-2, Route B). As a result, I have found that, for example, PNTz4T can be readily synthesized by the Suzuki-Miyaura polymerization.
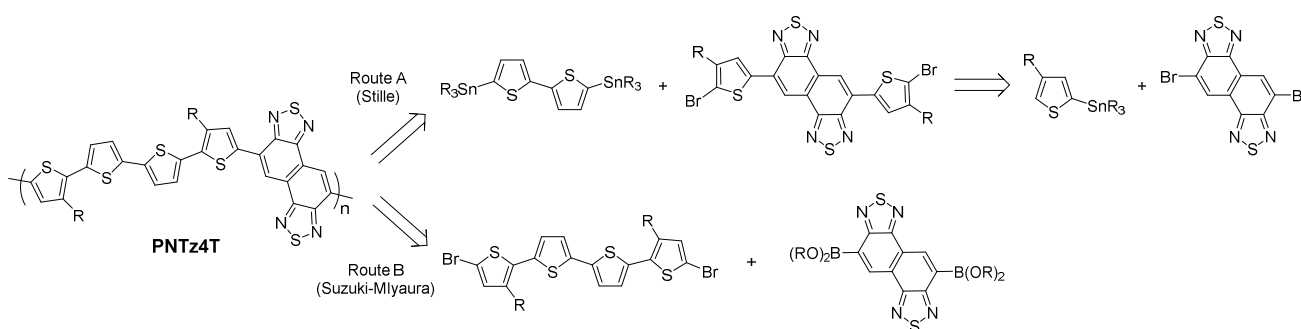

Scheme 2-2. Retrosynthetic schemes for PNTz4T as a representative of the NTz-polymers: a conversional approach using 5,10-dibromonaphtho[1,2-*c*:5,6-*c'*]bis[1,2,5]thiadiazole (top) and a new approach using 5,10-diboryalted NTz (bottom).

   To achieve the Suzuki-Miyaura polymerization for NTz-based polymers, the key intermediate is 5,10-diborylated NTz. Among several methods for borylation on aromatic cores so far developed, I choose a direct borylation reaction on parent NTz catalyzed by Ir complexes in the presence of bis(pinacolato)diboron,[10, 11] since the reaction usually takes place at the least sterically hindered position. In fact, similar heteroaromatics with four fused aromatic rings can be selectively borylated at the corresponding naphthalene parts on the fused ring systems[12, 13] Scheme 2-3 depicts the synthesis of 5,10-bis(4,4,5,5-tetramethyl-1,3,2-dioxaborolan-2-yl)naphtho[1,2-*c*:5,6-*c'*]bis[1,2,5]thiadiazole (NTz-Bpin$_2$). As I expected, the borylation reaction takes place at the least sterically hindered 5- and 10-positions on the NTz core under the typical borylation conditions (bis(pinacolato)diboron: 1.5 eq, [Ir(OMe)(COD)]$_2$: 10 mol%, 4,4'-di-tert-butyl-2,2'-bipyridine (dtbpy): 20 mol%, 80 °C for 20 h in dry cyclohexane), and

after recrystallization from chloroform/methyl isobutyl ketone to give highly pure NTz-Bpin$_2$ in 70% isolated yield (Scheme 2-3).

Scheme 2-3. Synthesis of NTz-Bpin$_2$

Quaterthiophene co-monomers were synthesized from 3-(2-decyltetradecyl)-2-bromothiophene (**1**) (Scheme 2-4). **1** was first derived into the corresponding borylated compound (**2**) via lithium-bromine exchange followed by a reaction with isopropoxyboronic acid pinacol ester. **2** was then utilized to the Suzuki-Miyaura coupling with 5,5′-dibromo-2,2′-bithiophene to give quaterthiophene with two 2-decyltetradecyl groups on the terminal thiophene rings (**3**). After bromination of **3** at the terminal thiophenes′ α-positions to give **4**, the palladium catalyzed Suzuki-Miyaura polymerization with the assist of microwave was carried out to prepare PNTz4T. The resulting polymer was purified by combining reprecipitation and consecutive Soxhlet extractions. The chloroform fraction in the Soxhlet extractions gave PNTz4T with M_n = 21.8 kDa, M_w = 40.2 kDa, and PDI = 1.84. Although this molecular weight is slightly lower than that prepared by the Stille reaction method (Scheme 2-2, Route A), that is suitable enough to be used in the preparation of thin film for OFET device.

(i) n-BuLi/THF, -78°C, then 2-isopropoxy-4,4,5,5-tetramethyl-1,3,2-dioxaborolane (Y=66%). (ii) Pd(dppf)Cl$_2$, K$_3$PO$_4$/DMF, 100°C (Y=94%). (iii) NBS/CHCl$_3$, DMF, 0°C (Y=92%). (iv) Pd(PPh$_3$)$_4$, Aliquat336, K$_2$CO$_3$/toluene, H$_2$O, μW 100°C (Y=74%)

Scheme 2-4. Synthesis of PNTz4Ts using NTz-Bpin$_2$.

I also confirm the oneness between the polymers prepared by two different methods by comparing the UV-vis absorption spectra in the dilute solution. Although the absorption peak in the long wavelength region for PNTz4T prepared by the Suzuki-Miyaura reaction appears slightly weaker than that prepared by the Stille reaction, which might be due to the difference of the molecular weight, the absorption edge is mostly the same and this clearly demonstrate that these two polymers are practically identical (Figure 2-2). In addition, the mobility, evaluated by OFETs, for PNTz4T synthesized by the Suzuki-Miyaura reaction was ~0.2 cm^2 V^{-1} s^{-1}, which is comparable to those for PNTz4T synthesized by the Stille reaction (Figure 2-3).
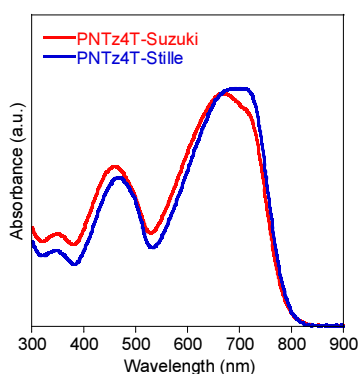

Figure 2-2. UV-vis absorption spectra of PNTz4T synthesized via the Stille and Suzuki methods in the solution.

It is important to note that aromatic halides as the corresponding co-monomers for the synthesis of NTz-based polymers using NTz-Bpin$_2$ are not just easy to be prepared but also the number is virtually infinite. I therefore conclude that NTz-Bpin$_2$ is a versatile and ready-to-use intermediate for synthesis of various NTz-based polymers.

In summary, I have successfully developed NTz-Bpin$_2$, by direct borylation reaction, as a versatile co-monomer for NTz-based semiconducting polymers. I demonstrated that NTz-Bpin$_2$ can be effectively utilized in the synthesis of PNTz4T. Considering the fact that NTz-Bpin$_2$ has two reactive boryl groups, which is ready to be polymerized with dihalogen substituted co-monomer units, it is very useful precursor that can pave the way for developing a range of NTz-based D-A polymers by combining electron donating

building blocks with halogen functionality as the handles. I hope that further material developments based on NTz will be accelerated in the near future by using NTz-Bpin$_2$.
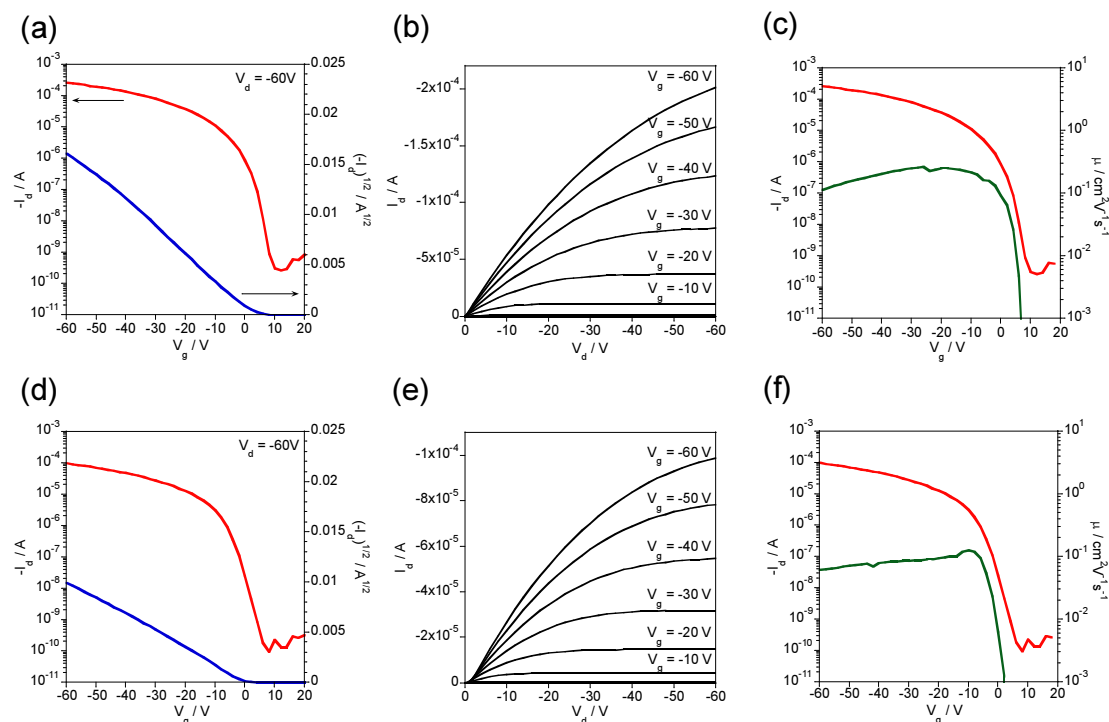
Figure 2-3. OFET characteristics of PNTz4T synthesized via the Suzuki methods (a) Transfer curves with the FDTS SAM. (b) Output curves with the FDTS SAM. (c) Transfer curves and the dependence of mobility on the V_g with FDTS SAM. (d) Transfer curves with the ODTS SAM. (b) Output curves with the ODTS SAM. (c) Transfer curves and the dependence of mobility on the V_g with ODTS SAM.

Table 2-1. OFET characteristics of PNTz4T synthesized via the Suzuki methods.

SAM	μ_h (cm^2/Vs)	V_{th} (V)	on / off
FDTS	0.13 (0.08 ~ 0.21)	−12.0 ~ 6.0	~ 10^6
ODTS	0.07 (0.04 ~ 0.08)	−9.6 ~ 7.9	~ 10^6

2-3. Implication of molecular orientation distribution on device performance

Osaka and co-workers previously reported a new D-A polymer with quaterthiophene and NTz as the D and A units, respectively (PNTz4T).[6] This polymer is promising as it shows a high PCE of 6.3% with around 100 nm active layer thickness in single-junction PSCs that use [6,6]-phenyl-C61-butyric acid methyl ester (PC$_{61}$BM) as the n-type material thanks to its long-wavelength absorption in the range of 300–800 nm and a relatively large ionization potential of 5.15 eV. Another striking feature of PNTz4T is that it forms a crystalline structure with a lamellar motif in which the polymer backbones are π-stacked with a distance of ca. 3.5 Å in the thin film. This π–π stacking distance is short compared with that of typical high-performance D–A polymers used in PSCs,[14, 15] owing to the strong intermolecular interactions most likely originating in the NTz-based backbone structure. In addition, PNTz4T forms a "face-on" orientation in the polymer/PC$_{61}$BM blend film, which is favourable for PSCs, whereas it forms an "edge-on" orientation in the polymer neat film suitable for transistors, in which high field-effect hole mobilities of up to 0.5 cm^2 V^{-1} s^{-1} was observed. The high crystallinity and the favourable backbone orientation well rationalize the high photovoltaic performance of PNTz4T.

Osaka and co-workers previously reported that the BHJ solar cells using the polymers with primary face-on orientation afforded high J_{SC} with thicker active layers without a loss of FF.[16] As above mentioned, PNTz4T forms a "face-on" orientation in the polymer/PC$_{61}$BM blend film, whereas it forms an "edge-on" orientation in the polymer neat film. Therefore, I thought that the polymer with thicker active layers can be applied to PNTz4T. I fabricated and evaluated the PSCs with active layer thickness variation from ca. 100 to 400 nm. In addition, I fabricated the inverted OPVs which have improved long-term ambient stability and also show higher PCEs in many cases as compared with conventional OPVs.[17-20] As a result, I demonstrated that PCEs of 10.1% can be achieved in a single-junction PSC with the inverted architecture and the active layer thickness of ca. 300 nm, which is much larger than that of typical PSCs. Importantly, I found that the face-on orientation is more abundant and that the distribution of the edge-on/face-on orientation through the film thickness is more favourable in the inverted cell than in the conventional cell,

which should be key factors for understanding the origin of the high performance in PNTz4T cells.

2-3-1. Solar cell fabrications and performance

I used PNTz4T samples which synthesized via the Stille coupling polymerization. Solar cells with conventional and inverted architectures were fabricated. The cells were composed of indium tin oxide (ITO)/poly(3,4-ethylenedioxythiophene):polystyrene sulfonate (PEDOT:PSS)/PNTz4T:$PC_{61}BM$ or [6,6]-phenyl-C71-butyric acid methyl ester ($PC_{71}BM$)/LiF/Al and ITO/ZnO/PNTz4T:$PC_{61}BM$ or $PC_{71}BM$/MoO$_x$/Ag, respectively. The PNTz4T to PCBM weight ratio was 1:2 in all cases. The active layer was fabricated by spin-coating the polymer/PCBM blend solution in o-dichlorobenzene (DCB). Note that no solvent additives were used in this system (for example, 1,8-diiodooctane (DIO) is often used to promote phase separation).

In a conventional cell using $PC_{61}BM$, a PCE of 6.55% with a J_{SC} of 12.1 mA cm^{-2}, an open-circuit voltage (V_{OC}) of 0.746 V, and a fill factor (FF) of 72.7% were obtained with an active layer thickness of 150 nm (Figure 2-4a, Table 2-2). This observed FF is fairly high considering that the active layer is 1.5 to 2 times thicker than that of typical PSCs (70–100 nm). I then fabricated cells with even thicker active layers. Similarly to previous studies using thicker active layers,[16, 21-24] the value of J_{SC} increased with increasing thickness. V_{OC} slightly decreased with the increasing thickness, but the change was relatively small. Although the FF showed a gradual decrease, it remained moderately high (66.7% at 300 nm). As a result, the overall PCE reached 8.70% with a J_{SC} of 17.7 mA cm^{-2} and V_{OC} of 0.738 V at 300 nm. The external quantum efficiency (EQE) was generally high, at 70% in the polymer absorption ranges of 300–500 nm and 600–800 nm (Figure 2-4b). In the conventional cell using $PC_{71}BM$ (Figure 2-4c), a large J_{SC} was obtained compared with the cell using $PC_{61}BM$, which is due to the increased absorption and thus the high EQE in the range of 500–600 nm (Figure 2-4d), as commonly observed for PSCs. The $PC_{71}BM$ cells showed a dependence of the photovoltaic parameters on the active layer thickness similarly to the $PC_{61}BM$ cell, and gave the highest PCE of 8.92% with the 290 nm thick active layer (Figure 2-4c, Table 2-3).

(a)

(b)

(c)

(d)
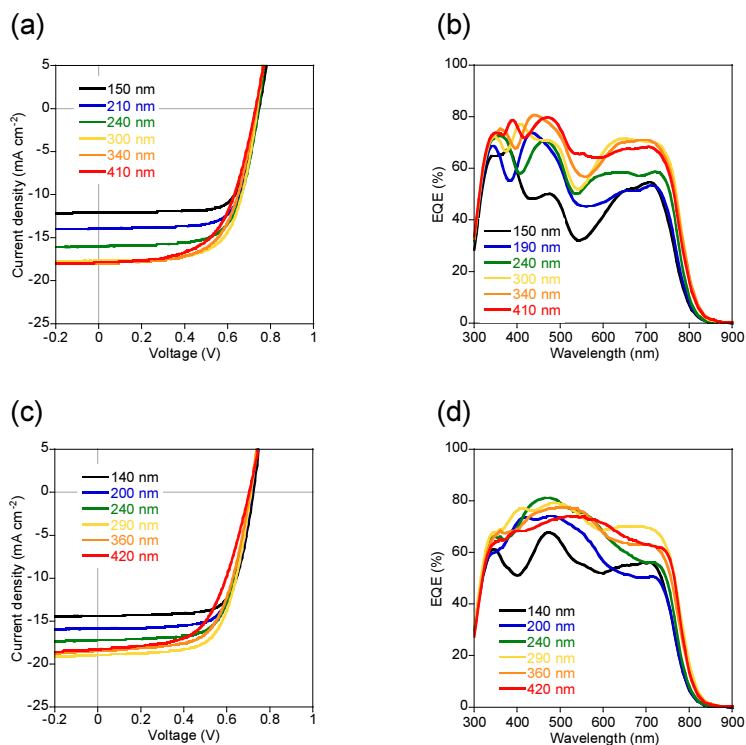
Figure 2-4. *J-V* curves (a) and EQE spectra (b) of conventional cells with PC$_{61}$BM. *J-V* curves (c) and EQE spectra (d) of conventional cells with PC$_{71}$BM.
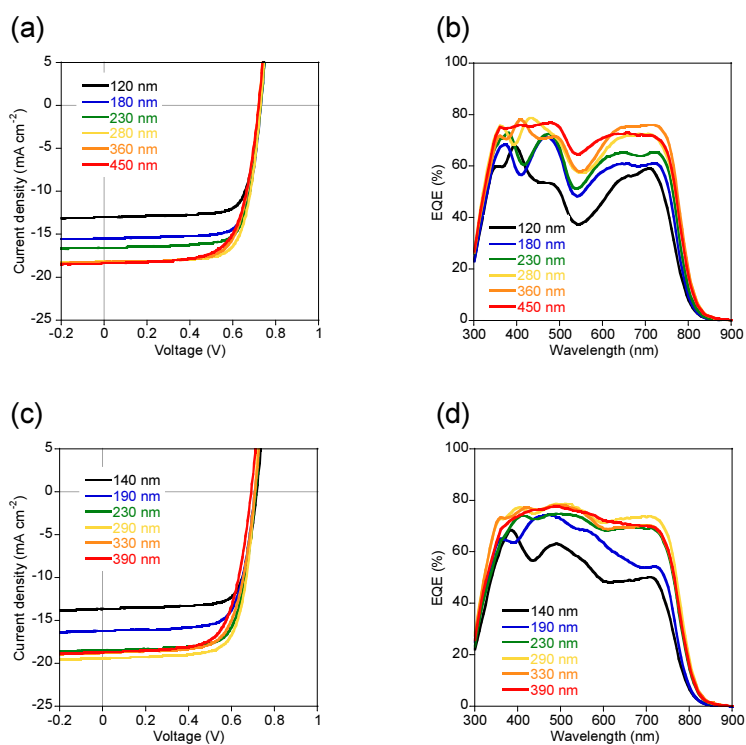
Table 2-2. Photovoltaic parameters of conventional cells with PC$_{61}$BM.

Thickness (nm)	J_{SC} (mA cm^{-2})	V_{OC} (V)	FF (%)	PCE (%)
150	12.1	0.746	72.7	6.55
210	13.9	0.739	71.5	7.36
240	16.0	0.743	67.9	8.06
300	17.7	0.738	66.7	8.70
340	17.9	0.732	63.2	8.30
410	17.9	0.729	59.8	7.78

Table 2-3. Photovoltaic parameters of conventional cells with PC$_{71}$BM.

Thickness (nm)	J_{SC} (mA cm^{-2})	V_{OC} (V)	FF (%)	PCE (%)
140	14.3	0.723	72.1	7.47
200	15.8	0.715	70.0	7.92
240	17.2	0.711	67.6	8.27
290	18.9	0.712	66.2	8.92
360	18.4	0.708	63.8	8.31
420	18.2	0.703	58.6	7.51

Interestingly, the inverted cells demonstrated high photovoltaic performances, compared to the conventional cells, in particular in terms of J_{SC} and FF, as has been observed in other polymer systems.[17-20] The inverted cells also showed the thickness dependence of photovoltaic performance (Figures 2-5a,b and Table 2-4, 2-5). Notably, the PCE reached 10.1% (J_{SC} = 19.4 mA cm^{-2}, V_{OC} = 0.708 V, FF = 73.4%), with an average of 9.77%, for the inverted PC$_{71}$BM cell with an active layer thickness of ~290 nm, which is one of the highest PCEs observed in a single-junction cell. It is interesting to note that PCEs close to 10% were also observed for the inverted PC$_{61}$BM cell with a thickness of 280 nm (PCE = 9.80% (average 9.55%), J_{SC} = 18.2 mA cm^{-2}, V_{OC} = 0.729 V, FF = 73.9%).

Figure 2-5. *J-V* curves (a) and EQE spectra (b) of inverted cells with PC$_{61}$BM. *J-V* curves (c) and EQE spectra (d) of inverted cells with PC$_{71}$BM.

Table 2-4. Photovoltaic parameters of inverted cells with $PC_{61}BM$.

Thickness (nm)	J_{SC} (mA cm^{-2})	V_{OC} (V)	FF (%)	PCE (%)
120	13.0	0.725	76.2	7.18
180	15.4	0.731	76.6	8.64
230	16.5	0.730	75.2	9.07
280	18.2	0.729	73.9	9.80
360	18.2	0.719	71.5	9.37
450	18.4	0.720	68.7	9.08

Table 2-5. Photovoltaic parameters of inverted cells with $PC_{71}BM$.

| Thickness (nm)	J_{SC} (mA cm^{-2})	V_{OC} (V)	FF (%)	PCE (%)
140	13.6	0.716	75.1	7.33
190	16.2	0.708	73.1	8.36
230	18.5	0.712	72.8	9.57
290	19.4	0.708	73.4	10.1
330	18.8	0.708	70.1	9.32
390	18.7	0.691	68.4	8.84

To investigate the reason for higher FF in the inverted cell than in the conventional cells, I conducted a qualitative study of the difference in charge recombination between the two device architectures by plotting J_{SC} and FF as a function of light intensity (Figures 2-6a,b).[25] It is clear that for both conventional and inverted $PC_{61}BM$ and $PC_{71}BM$ cells, J_{SC} increases linearly as the light intensity increase increases, wherein the number of free carriers increases. The decrease in FF with increasing light intensity was milder in the inverted cells than in the conventional cells. The difference in the decrease in FF implies that bimolecular recombination is reduced in the inverted cell compared with the conventional cell, which may be one of the reasons for the higher FF in the inverted cell of this system.
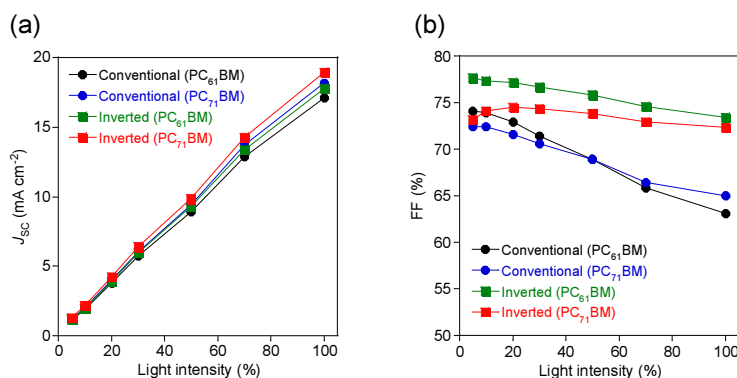
Figure 2-6. J_{SC} (a) and FF (b) as a function of light intensity.

2-3-2. Charge transport property

Charge carrier mobilities of the blend films in the direction perpendicular to the substrate plane were evaluated by using hole-only (ITO/PEDOT:PSS/active layer/MoO$_x$/Ag) and electron-only (ITO/ZnO/active layer/LiF/Al) devices (Figures 2-7a,b). The polymer neat film was also evaluated in the hole-only device (Figure 2-7a). Both hole (μ_h) and electron (μ_e) mobilities were obtained by using the space-charge limited current (SCLC) model. The value of μ_h for the polymer neat film was 7.2×10^{-4} cm^2 V^{-1} s^{-1}, while those for the blend films with PC$_{61}$BM and PC$_{71}$BM were 2.1×10^{-3} cm^2 V^{-1} s^{-1} and 3.4×10^{-3} cm^2 V^{-1} s^{-1}, respectively. The higher μ_h for the blend film than for the polymer neat film is probably due to the more favourable backbone orientation for vertical charge transport in the blends.[6] The μ_h values for the blends are fairly high for the semiconducting polymers[26] and most probably originate from the combination of the highly crystalline structure and short π–π stacking distance (3.5 Å), and the favourable face-on orientation. It should be noted that μ_e was also on the order of 10^{-3} cm^2 V^{-1} s^{-1} (2.3×10^{-3} cm^2 V^{-1} s^{-1} for the blend film with PC$_{61}$BM, and 1.1×10^{-3} cm^2 V^{-1} s^{-1} for that with PC$_{71}$BM). These results are indicative of the well-balanced hole and electron transport in the PNTz4T/PCBM blend films, explaining the high photovoltaic performance for the PNTz4T cells.
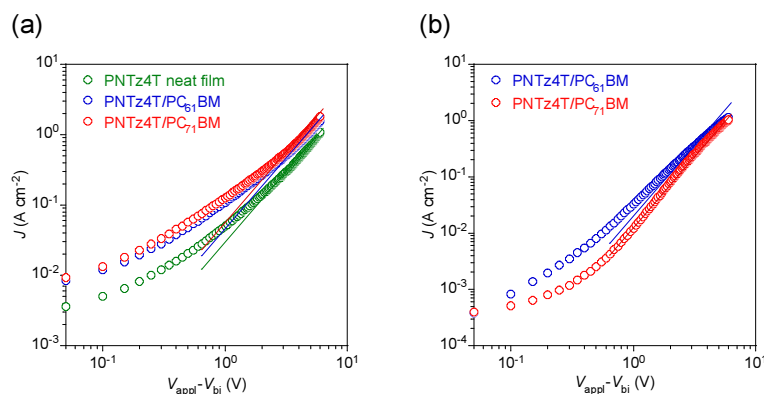
Figure 2-7. *J-V* curves of (a) the hole-only devices (ITO/PEDOT:PSS/active layer/MoOx/Ag) and (b) the electron-only devices (ITO/ZnO/active layer/ LiF/Al).

2-3-3. Grazing incidence wide-angle X-ray diffraction (GIWAXD) studies

The polymer microstructures in the blend films were studied by grazing-incidence wide-angle X-ray diffraction (GIWAXD) measurements. Figure 2-8b,e displays the two-dimensional (2D) GIWAXD images of PNTz4T/PC$_{61}$BM blend films spun on ITO/PEDOT:PSS and ITO/ZnO substrates (film thickness, ~250 nm). In both cases, a diffraction corresponding to the π–π stacking appeared only along the q_z axis (out-of-plane direction), suggesting that there is a large population of polymer crystallites with the face-on orientation.[27] Nevertheless, diffractions corresponding to the lamellar structure appeared along both the q_z and q_{xy} (in-plane direction) axes, indicating that edge-on and face-on crystallites co-exist in the film. These results indicate that the polymer easily forms a crystalline structure in the blend films by spin- coating from DCB solution onto both substrates. The fact that PNTz4T/PC$_{71}$BM blend films also showed similar textures to the PNTz4T/PC$_{61}$BM blend films (Figure 2-8c,f) suggests that there is no significant difference in polymer crystallinity and orientation between the PC$_{61}$BM and PC$_{71}$BM blend films.

To gain a deeper insight into the orientation, I performed a pole figure analysis of the blend films.[28, 29] Figure 2-9c shows the pole figures extracted from the lamellar diffraction, (100), of PNTz4T in the 2D GIWAXD patterns for the PNTz4T/PC$_{61}$BM blend films on the ITO/PEDOT:PSS and ITO/ZnO substrates (thickness, ~250 nm), as shown in Figures 2-9a and 2-9b (see insets for a close-up of the

lamellar diffraction). I defined that the areas integrated with the polar angle (χ) ranges of 0–45° and 135–180° (A_z) and 55–125° (A_{xy}) as those corresponding to the fractions of the edge-on and face-on crystallites, respectively. It is interesting to note that the ratio of A_{xy} to A_z (A_{xy}/A_z) for the blend film on the ITO/ZnO substrate was 0.79, which was higher than that for the blend film on the ITO/PEDOT:PSS substrate, namely, 0.64. This means that the population of the face-on crystallite is larger in the inverted cells than in the conventional cells. This could be attributed to the difference in wettability of the solution on the substrate surfaces. It has been reported that substrate surfaces with lower wettability induce a higher tendency of edge-on orientation to semiconducting polymers in the thin film by spin-coating the polymer solution.[30] I therefore measured the contact angle of DCB, the solvent used for the spin-coating, on the PEDOT:PSS and ZnO surfaces (both coated on the ITO glass substrate), and obtained average values of 18.5° and 6.1°, respectively (Figure 2-10). This suggests that the PEDOT:PSS surface has low wettability compared to the ZnO surface, which may explain the larger population of edge-on orientation on the PEDOT:PSS surface (larger population of face-on orientation on the ZnO surface).
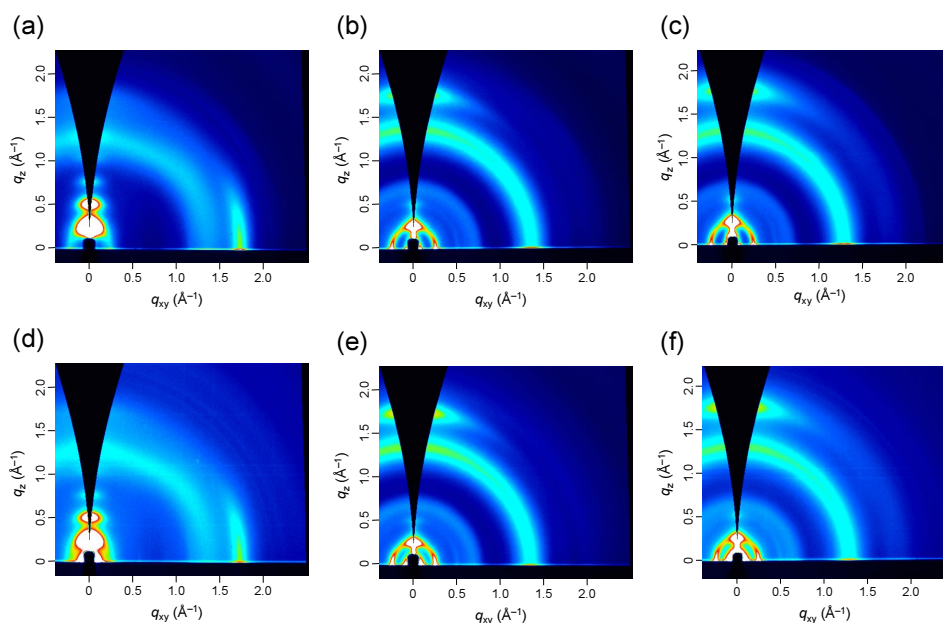
Figure 2-8. (a-c) 2D-GIWAXD images of the films on ITO/PEDOT:PSS substrate. The PNTz4T neat film (a), the PNTz4T/PC$_{61}$BM blend film (1:2 wt ratio) (b), the PNTz4T/PC$_{71}$BM blend film (1:2 wt ratio) (c). (d-f) 2D-GIWAXD images of the films on ITO/ZnO substrate. The PNTz4T neat film (d), the PNTz4T/PC$_{61}$BM blend film (1:2 wt ratio) (e), the PNTz4T/PC$_{71}$BM blend film (1:2 wt ratio) (f).
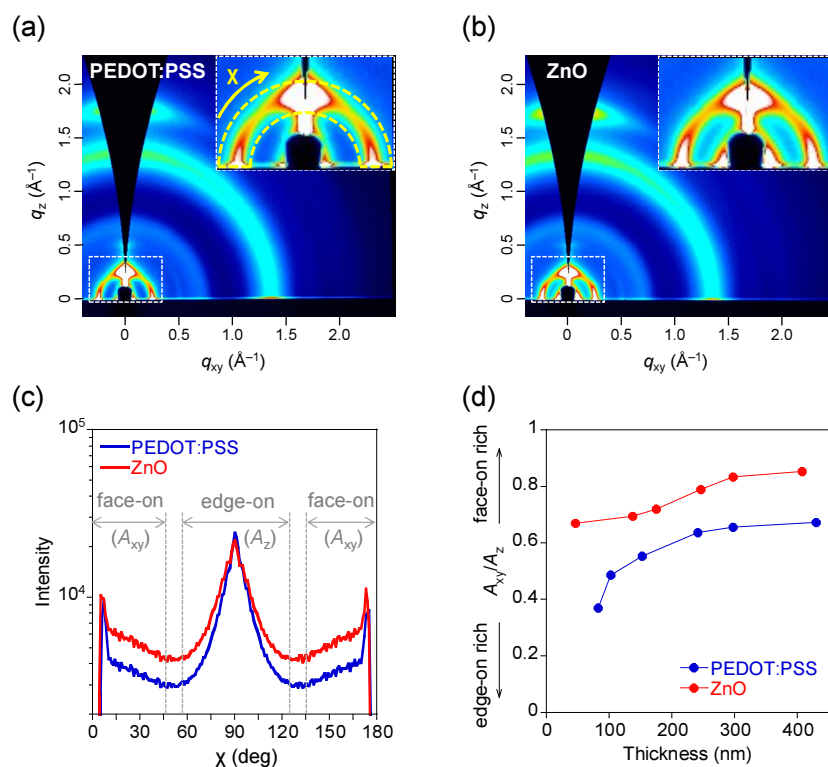
Figure 2-9. GIWAXD data for PNTz4T/PC$_{61}$BM blend films. (a) 2D GIWAXD image of the blend film on the ITO/PEDOT:PSS substrate (thickness, 241 nm). (b) 2D GIWAXD image of the blend film on the ITO/ZnO substrate (thickness, 246 nm). Insets: close-up of the lamellar, (100), diffraction region. (c) Pole figures extracted from the lamellar diffraction for the blend films on both ITO/PEDOT:PSS and ITO/ZnO substrates. Definition of the polar angle (χ) range corresponding to the edge-on (A_z) and face-on (A_{xy}) crystallites are also shown. (d) Dependence of A_{xy}/A_z on the film thickness. A_{xy}/A_z is a figure that represents the ratio of the face-on to edge-on orientation.
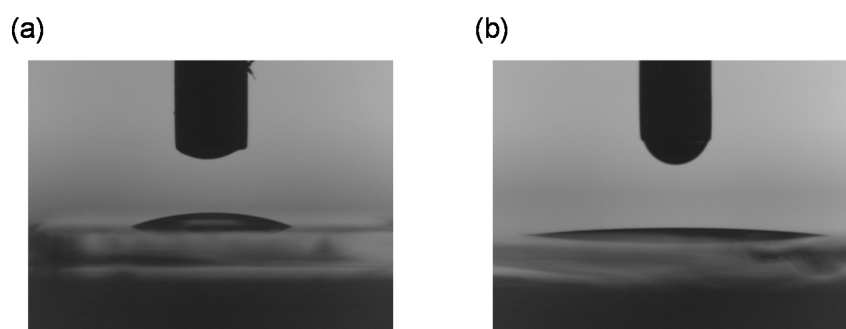

Figure 2-10. Photos of a DCB droplet. (a) ITO/PEDOT:PSS substrate. (b) ITO/ZnO substrate. The average contact angle of DCB, collected from 10 different substrates, on the ITO/PEDOT:PSS and ITO/ZnO substrates are 18.5° (±2.31) and 6.1° (±0.42), respectively.

I also carried out pole figure analysis of the PNTz4T/PC$_{61}$BM blend films on the ITO/PEDOT:PSS and ITO/ZnO substrates with different thicknesses ranging from ~50 nm to 400 nm, then plotted A_{xy}/A_z as a function of film thickness (Figure 2-9d). For all the thicknesses, A_{xy}/A_z was larger for the ITO/ZnO substrate than for the ITO/PEDOT:PSS substrate. Notably, A_{xy}/A_z gradually increased with the increasing film thickness in both cases; that is, the population of the face-on crystallites increased with the film thickness. This suggests that the face-on to edge-on ratio is not distributed evenly along the film thickness. One can assume that the orientation in the interfacial layers at the bottom (PEDOT:PSS or ZnO) and top (air), as well as the thickness of the interfacial layer, is independent of the total film thickness. Thus, this increase in the face-on crystallite population mainly occurs at the bulk, and arises from the increase in the bulk volume in thicker films. This means that the edge-on crystallites are abundant either at the film-bottom or film-air interface. In regioregular poly(3-hexylthiophene) films it has been reported previously that edge-on crystallites exist at the film-bottom layer interface and that face-on crystallites exist in the bulk and at the film-air interface.[31,32] Thus, in the case of PNTz4T, a class of polythiophene-based polymer, it is natural to consider that the edge-on crystallites are abundant at the film-bottom layer interface and that the face-on crystallites are abundant in the bulk through the film-air interface, regardless of the substrate. The PNTz4T/PC$_{71}$BM blend film provided the similar results to the PNTz4T/PC$_{61}$BM blend film.

In summary, I have demonstrated PCE values reaching 10% in singe-junction PSCs with an inverted architecture, using PNTz4T as the p-type material and PC$_{71}$BM as the n-type material. Notably, these results has been achieved by using the thick active layer measuring around 300 nm which is far thicker than the typical thickness for PSCs and is beneficial for the practical use.[21, 23] The high efficiency is most likely attributed to the highly ordered polymer structure in the active layer, in which the highly crystalline structure with the short π–π stacking distance and the favourable face-on orientation are achieved. I found that PNTz4T shows a higher tendency to form the favourable face-on orientation on the ZnO surface than on the PEDOT:PSS surface, which correspond to the inverted and conventional cells, respectively. It is

also important to mention that I observed unevenly distributed polymer orientations through the film thickness, as revealed by the in-depth GIWAXD studies. The population of the face-on crystallites is larger in the bulk through the film/top interlayer interface, i.e., the film/LiF (conventional cell) or MoO_x (inverted cell) top interfaces, and the population of the edge-on crystallites is larger at the film/bottom interlayer interface, i.e., the film/PEDOT:PSS (conventional cells) or film/ZnO (inverted cells) interfaces, as illustrated in Figure 2-11. Therefore, in the conventional cells, where the generated holes flow toward the bottom PEDOT:PSS layer through the edge-on-rich region, this distribution of the polymer orientation should be detrimental to the vertical hole transport, resulting in the inefficient hole collection. In contrast, in the inverted cells, where the holes flow toward the top MoO_x layer through the face-on-rich region, this polymer orientation distribution would facilitate the vertical hole transport, leading to the efficient hole collection. This model is in good agreement with the high J_{SC} and FF, as well as the reduced charge recombination, in the inverted cell compared with the conventional cell.
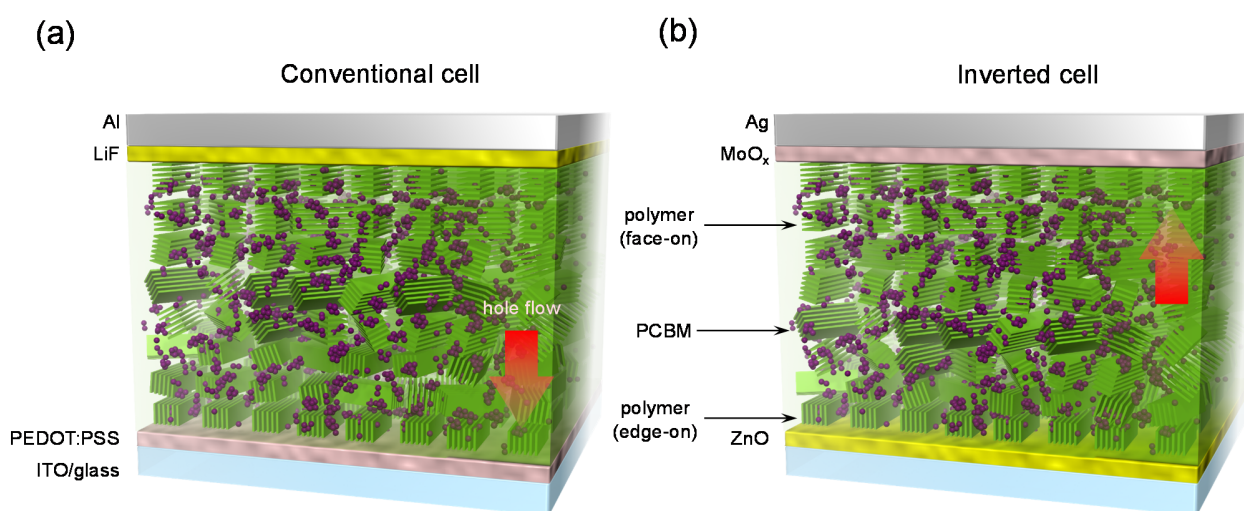
Figure 2-11. Schematic illustrations of PNTz4T/PC$_{61}$BM blend films in the solar cells. (a) Conventional cell with PEDOT:PSS as the bottom and LiF as the top interlayer. (b) Inverted cell with ZnO as the bottom and MoO_x as the top interlayer. The population of face-on crystallite is larger in the inverted cell than in the conventional cell. In both cases, the population of edge-on crystallites is large at the bottom interface and the population of face-on crystallites is large in the bulk through the top interface. Note that the amount of PCBM is markedly reduced as compared with the real cells and the distribution of the orientation is exaggerated in order to better visualize the polymer orientation.

2-4. Conclusion of chapter 2

I have successfully developed NTz-Bpin$_2$, by a direct borylation reaction, as a versatile co-monomer for NTz-based semiconducting polymers. PNTz4T, which is previously synthesized through the Stille coupling reaction, can be synthesized using NTz-Bpin$_2$ through the Suzuki-Miyaura coupling reaction. With this method, I am able to avoid the use of toxic organotin monomers, which is very important from the viewpoint of industrial use.

I also have demonstrated that high efficiencies of 10.1% can be obtained using the crystalline polymer PNTz4T in single-junction inverted cells with a thick active layer having a thickness of ~300 nm. I found that there is the distribution of the edge-on/face-on orientation thorough the film thickness, and it is important to choice device structure which is suited for the distribution.

2-5. Experimental section

Synthesis

Naphtho[1,2-*c*:5,6-*c'*]bis[1,2,5]thiadiazole (NTz) was synthesized according to the reported procedure.[4] All chemicals and solvents are of reagent grade unless otherwise indicated. THF and DMF were purified by a Glass Contour Solvent System, and cyclohexane and toluene were distilled with CaH$_2$ prior to use. Polymerization was carried out with a microwave reactor, Biotage Initiator. Nuclear magnetic resonance (NMR) spectra were obtained in deuterated chloroform (CDCl$_3$) and *o*-dichlorobenzene (*o*-DCB-*d*$_4$) with TMS as internal reference. High-resolution mass spectrometry was carried out with a LTQ Orbitrap XL (Thermo Fisher Scientific). Molecular weights were determined by gel permeation chromatography (GPC) with a TOSOH HLC-8121GPC/HT at 140 °C using *o*-DCB as a solvent and calibrated with polystyrene standards.

5,10-Bis(4,4,5,5-tetramethyl-1,3,2-dioxaborolan-2-yl)naphtho[1,2-*c*:5,6-*c′*]bis[1,2,5]thiadiazole [NTz-Bpin₂]

To a 200-mL three-neck flask were placed (1,5-cyclooctadiene)(methoxy)iridium(I) dimer (398 mg, 0.60 mmol), 4,4′-di-*tert*-butyl-2,2′-bipyridyl (490 mg, 1.20 mmol), and cyclohexane (150 mL) under an N_2 atmosphere. The mixture was then refluxed for 1 h. Bis(pinacolato)diboron (4.57 g, 18.0 mmol) was added and the mixture was refluxed for 30 min. Naphtho[1,2-c:5,6-c′]bis[1,2,5]thiadiazole (NTz) (1.47 g, 6.00 mmol) was added to the mixture, which was then refluxed for 20 h. After the mixture was cooled to room temperature, the precipitate was filtered, washed with methanol, and dried in vacuo. The crude product was purified by recrystallization from chloroform/methyl isobutyl ketone to give NTz-Bpin₂ as yellow solid (2.08 g, 70%). ^{1}H NMR (500 MHz, CDCl₃): δ 9.51 (s, 2H), 1.50 (s, 24H). ^{13}C NMR (500 MHz, CDCl₃): δ 157.0, 152.7, 136.7, 136.7, 126.7, 84.7, 25.0, 24.9. EI-MS (70 eV) *m/z* 496 (M⁺). Anal. Calcd for $C_{22}H_{26}N_4O_4S_2B_2$: C, 53.25; H, 5.28; N, 11.29%. Found: C, 53.03; H, 5.24; N, 11.18%.

2-(4,4,5,5-Tetramethyl-1,3,2-dioxaborolane-2-yl)-3-(2-decyltetradecyl)thiophene (2)

To a 100-mL three-neck flask with a dropping funnel were placed **1** (3.00 g, 6.00 mmol) and THF (24 mL) under an N_2 atmosphere. After cooled to −78 °C, 1.64 M *n*-BuLi hexane solution (4.0 mL, 6.60 mmol) was added slowly. After the solution was stirred at −78 °C for 1 h, a solution of 2-isopropoxy-4,4,5,5-tetramethyl-1,3,2-dioxaborolane (1.51 g, 8.10 mmol) in 6 mL of THF was added. The solution was gradually warmed to room temperature, and stirred for 16 h. Saturated NH₄Cl aq. was added, and the mixture was extracted with ethyl acetate. The organic layer was washed with brine and then dried over anhydrous MgSO₄. The solvent was removed by vacuum evaporation, and the residue was purified by column chromatography on silica gel with hexane-dichloromethane (4:1) to give **2** as yellow oil (2.16 g, 66%). ^{1}H NMR (500 MHz, CDCl₃): δ 7.47 (d, 1H, *J* = 4.7 Hz), 6.97 (d, 1H, *J* = 4.7 Hz), 2.80 (d, 2H, *J* = 7.2 Hz), 1.58 (m, 1H), 1.32 (s, 12H), 1.17−1.30 (m, 40H), 0.88 (t, 6H, *J* = 7.0Hz). ^{13}C NMR (500 MHz, CDCl₃): δ 153.8, 131.0, 131.0, 83.5, 40.2, 34.8, 33.4, 31.9, 30.1, 29.7, 29.7, 29.7, 29.4, 26.6, 24.8, 22.7,

14.1. EI-MS (70 eV) m/z 546 (M^+). HR-MS (APCI) m/z calcd for $C_{34}H_{63}O_2BS$ $[M]^+$ 546.46363, found 546.46484.

3, 3′″-Bis (2-decyltetradecyl)-2,2′:5′,2″:5″,2′″-quaterthiophene (3)

To a 100-mL three-neck flask with a reflux condenser were placed **2** (2.00 g, 3.66 mmol), 5,5′-dibromo-2,2′-bithiophene (539 mg, 1.66 mmol), and DMF (35 mL) and purged with N_2 for 30 min. Potassium phosphate (2.11 g, 9.96 mmol) and Pd(dppf)Cl$_2$ (61 mg, 0.08 mmol) were added, and the solution was heated under N_2 at 100 °C for 16 h. After the mixture was cooled to room temperature, saturated NH$_4$Cl aq. was added, and the mixture was extracted with ethyl acetate. The organic layer was washed with saturated NaHCO$_3$ aq. and brine, and then dried over anhydrous MgSO$_4$. The solvent was removed by vacuum evaporation, and the residue was purified by column chromatography on silica gel with hexane to give **3** as yellow oil (1.57 g, 94%). ^{1}H NMR (500 MHz, CDCl$_3$): δ 7.18 (d, 2H, J = 5.0 Hz), 7.11 (d, 2H, J = 3.6 Hz), 7.01 (d, 2H, J = 3.4 Hz), 6.90 (d, 2H, J = 5.1 Hz), 2.71 (d, 4H, J = 7.2 Hz), 1.65−1.73 (m, 2H), 1.16−1.32 (m, 80H), 0.87 (t, 12H, J = 6.7 Hz). ^{13}C NMR (500 MHz, CDCl$_3$): δ 139.2, 136.9, 135.3, 130.8, 130.6, 126.8, 123.7, 123.6, 38.9, 33.8, 33.5, 31.9, 30.0, 29.7, 29.7, 29.7, 29.7, 29.4, 26.5, 22.7, 14.1. MS (MALDI-TOF): m/z calcd for $C_{64}H_{106}S_4$ $[M]^+$ 1002.72, found 1003.38. HR-MS (APCI) m/z calcd for $C_{64}H_{106}S_4$ $[M]^+$ 1002.71719, found 1002.71747.

5,5′″-Dibromo-3,3′″-bis(2-decyltetradecyl)-2,2′:5′,2″:5″,2′″-quaterthiophene (4)

To a 100-mL three-neck flask with a dropping funnel was placed **3** (1.00 g, 1.00 mmol), and dissolved in chloroform (25 mL). After cooled to 0 °C, a solution of N-bromosuccinimide (357 mg, 2.00 mmol) in 25mL of DMF was added slowly. The solution was gradually warmed to room temperature. After the solution was stirred at room temperature for 3 h, saturated NaHCO$_3$ aq. was added, and the mixture was extracted with hexane. The organic layer was washed with brine and then dried over anhydrous MgSO$_4$. The solvent was removed by vacuum evaporation, and the residue was purified by column

chromatography on silica gel with hexane, subsequently by recrystallization from methyl isobutyl ketone to give **4** as a yellow solid (1.06 g, 92%). ^{1}H NMR (500 MHz, CDCl$_3$): δ 7.09 (d, 2H, J = 3.7 Hz), 6.95 (d, 2H, J = 3.8 Hz), 6.86 (s, 2H), 2.64 (d, 4H, J = 7.2 Hz), 1.59−1.67 (m, 2H), 1.17−1.32 (m, 80H), 0.87 (t, 12H, J = 6.8 Hz). ^{13}C NMR (500 MHz, CDCl$_3$): δ 140.0, 137.2, 134.0, 133.1, 132.1, 127.3, 123.8, 110.6, 38.9, 33.7, 33.4, 31.9, 31.9, 30.0, 29.7, 29.7, 29.7, 29.4, 26.5, 22.7, 14.1. MS (MALDI-TOF): m/z calcd for C$_{64}$H$_{105}$S$_4$Br$_2$ [M+H]$^+$ 1158.54, found 1158.73; HR-MS (APCI) m/z calcd for C$_{64}$H$_{105}$S$_4$Br$_2^+$ [M+H]$^+$ 1158.53821, found 1158.53711.

PNTz4T (via the Suzuki coupling reaction)

4 (42 mg, 0.036 μmol), NTz-Bpin$_2$ (18 mg, 0.036 μmol), Aliquat 336 (8 mg), and toluene (3.2 mL) were added to a 5 mL reaction vial. The vial was purged with argon for 30 min, and 20% K$_2$CO$_3$ aq. (250 mg, 0.362 μmol), tetrakis(triphenylphosphine)palladium(0) (0.83 mg, 0. 72 μmol) were added. The vial was sealed and heated in a microwave reactor at 100 °C for 2 h. After cooling to room temperature, the reaction mixture was poured into a mixture of methanol (100 mL) and concentrated HCl (5 mL), and vigorously stirred for 6 h at room temperature. The precipitate was filtered and subjected to Soxhlet extraction sequentially with methanol, hexane, dichloromethane, chloroform, and finally chlorobenzene. The CHCl$_3$ and chlorobenzene fractions were concentrated and poured into methanol, respectively. The precipitates were collected by filtration to afford the polymer samples (chloroform fraction: 33 mg, 74%. chlorobenzene fraction: 4 mg, 9%) as metallic dark purple solids. ^{1}H NMR (500 MHz, o-DCB-d$_4$): δ 9.11 (br, 2H), 8.39 (br, 2H), 8.26 (br, 2H), 7.26 (br, 2H), 3.03 (br, 4H), 1.56 (br, 2H), 1.27 (br, 80H), 0.86 (br, 12H). Anal. Calcd for C$_{74}$H$_{106}$N$_4$S$_6$: C, 71.44; H, 8.59; N, 4.50. Found: C, 71.54; H, 8.56; N, 4.40. GPC (o-DCB, 140 °C): M_n = 21,800, M_w = 40,200, PDI = 1.84 (CHCl$_3$ fraction), M_n = 25,200, M_w = 45,500, PDI = 1.81 (chlorobenzene fraction).

Instrumentation

UV−vis absorption spectra were measured using a Shimadzu UV-3600 spectrometer.

OFET fabrication and evaluation

OFET devices were fabricated in a bottom-gate-top-contact configuration on a heavily doped n$^+$-Si(100) wafer with 200-nm-thickness thermally grown SiO$_2$ (C_i = 17.3 nFcm^{-2}). The Si/SiO$_2$ substrates were ultrasonicated with water for 3 min thrice, and acetone and isopropanol for 5 min, respectively, and rinsed in boiled isopropanol for 10 min, and then were subjected to UV-ozone treatment for 30 min. The cleaned substrates were then treated by 1H,1H,2H,2H-perfluorodecyltriethoxysilane (FDTS) or octadecyltriethoxysilane (ODTS) as follows. For FDTS, the substrates were left in a Teflon container with several drops of FDTS and then the container was heated to 120 °C for 2h in the desiccator. The FDTS-treated substrates were ultrasonicated with acetone and isopropanol for 5 min, respectively, and rinsed in boiled isopropanol for 10 min. For ODTS, a solution of ODTS in trichloroethylene (3 mM) was spin-coated onto the substrates at a rate of 3000 rpm for 15 sec followed by hydrolysis in a closed container in the presence of ammonia hydroxide solution for 24 h. After the hydrolysis, the substrates were rinsed with water, acetone and boiling isopropanol, respectively. In a glove box under nitrogen atmosphere, polymer thin films were spin-coated from hot DCB solutions (3 gL^{-1}) at 1000 rpm for 10 sec and then 2500 rpm for 35 sec. The polymer films were annealed at 200 °C for 30 min under nitrogen. On top of the polymer thin films, gold drain and source contact electrodes (thickness: 80 nm) with the channel length and width of 40 μm and 1500 μm, respectively, were deposited in vacuum through shadow masks.

Current-voltage characteristics of the OFET devices were measured at room temperature under ambient conditions (relative humidity: 30~40%) with a Keithley 4200-SCS semiconductor parameter analyzer. Threshold voltages of the devices were estimated from the transfer plots by extrapolating the square root of the drain current to the horizontal axis. Hole field-effect mobilities were extracted from the square root of the drain current in the saturation regime (V_d = –60 V) by using the following equation,

$$I_d = (WC_i/2L)\ \mu\ (V_g - V_{th})^2$$

where, L and W are channel length and width, respectively, and C_i is capacitance of the gate insulator. The average hole mobilities and threshold voltages were obtained over more than 10 devices.

Materials for OPV

PNTz4T samples were synthesized according to the reported procedure.[6] The molecular weights (M_n) of the samples were 50–60 kDa and the polydispersity index (PDI) was ~2.5. $PC_{61}BM$ and $PC_{71}BM$ were purchased from Frontier Carbon Corporation, Solenne BV, and Luminescence Technology Corporation. $PC_{61}BMs$ and $PC_{71}BMs$ from different suppliers gave similar results. PEDOT:PSS (Clevios P VP Al 4083) was purchased from Heraeus. The patterned ITO-coated glass substrates were purchased from Atsugi Micro, Co. Ltd.

Thin film characterization

GIWAXD experiments were conducted at the SPring-8 on beamline BL46XU. The sample was irradiated with an X-ray energy of 12.39 keV (λ = 1 Å) at a fixed incident angle on the order of 0.12° through a Huber diffractometer. The GIWAXD patterns were recorded with a two-dimensional image detector (Pilatus 300K).

Solar cells fabrication and characterization

ITO substrates were pre-cleaned sequentially by sonicating in a detergent bath, de-ionized water, acetone, and isopropanol at rt, and in a boiled isopropanol bath, each for 10 min. Then, the substrates were subjected to UV/ozone treatment at rt for 20 min. For conventional cells, the pre-cleaned ITO substrates were coated with PEDOT:PSS by spin coating (5000 rpm for 30 sec, thickness: ~30 nm), and then baked at 120 °C for 15 min in air. The active layer was deposited in a glove box by spin coating hot (100 °C) DCB solution containing PNTz4T and $PC_{61}BM$ or $PC_{71}BM$ with the weight ratio of 1:2 at 600 rpm for 20

sec. The active layer thickness was controlled by changing the concentration of the solution, e.g., an 8 g/L solution (based on the polymer concentration) typically gave an active layer of 250–300 nm thickness. The thin films were transferred into a vacuum evaporator connected to the glove box, and LiF (0.8 nm) and Al (100 nm) were deposited sequentially through a shadow mask under ~10^{-5} Pa, where the active area of the cells was 0.16 cm^2. For the inverted cells, the pre-cleaned ITO substrates masked at the electrical contacts were coated with ZnO precursor by spin coating (3000 rpm for 30 sec) a precursor solution prepared by dissolving zinc acetate dehydrate (0.5 g) and ethanolamine (0.14 mL) in 5 mL of 2-methoxyethanol. They were then baked in air at 200 °C for 30 min, then rinsed with acetone and isopropanol, and dried in a glove box. The active layer was deposited as described above. MoOx (7.5 nm) and Ag (100 nm) were deposited sequentially by thermal evaporation under ~10^{-5} Pa.

J–V characteristics of the cells were measured with a Keithley 2400 source measure unit in nitrogen atmosphere under 1 Sun (AM1.5G) conditions using a solar simulator (SAN-EI Electric, XES-40S1, 1000 W m^{-2}). More than 20 cells have been analysed to provide average efficiencies for the optimized cells. The light intensity for the *J–V* measurements was calibrated with a reference PV cell (Konica Minolta AK-100 certified by the National Institute of Advanced Industrial Science and Technology, Japan). EQE spectra were measured with a Spectral Response Measuring System (Soma Optics, Ltd., S-9241). The thickness of the active layer was measured with an AlphaStep® D-100 surface profiler (KLA Tencor).

Hole-only and electron-only devices fabrication and measurement[33]

For hole-only devices, the pre-cleaned ITO substrates were coated with PEDOT:PSS by spin-coating (5000 rpm for 30 sec, thickness: ~30 nm). Then, the PNTz4T film or the PNTz4T/PC$_{61}$BM or PC$_{71}$BM (1:2 weight ratio) blend film was spin coated from a hot (100 °C) DCB solution (8 g/L based on the polymer concentration) at 600 rpm for 20 sec. The thin films were transferred into a vacuum evaporator connected to the glove box, and MoO$_x$ (7.5 nm) and Ag (100 nm) were deposited sequentially through a shadow mask. For electron-only devices, the pre-cleaned ITO substrates were coated with ZnO, and then

with the PNTz4T/PC$_{61}$BM or PC$_{71}$BM (1:2 weight ratio) blend film as described above. LiF (2 nm) and Al (100 nm) were deposited sequentially. *J–V* characteristics were measured in the range of 0−7 V using a Keithley 2400 source measure unit under nitrogen in the dark, and the mobility was calculated by fitting the *J–V* curves to a space charge limited current model described by

$$J = (8/9)\, \varepsilon_r\, \varepsilon_0\, \mu\, (V^2/L^3)$$

where ε_r is the dielectric constant of the polymer, ε_0 is the permittivity of free space, μ is the mobility, $V = V_{appl} - V_{bi}$, where V_{appl} is the applied voltage to the device and V_{bi} is the built-in voltage due to the difference in work function of the two electrodes, which is determined to be 0.1 for the hole-only device and 0.1 for the electron-only device, and L is the polymer thickness. The dielectric constant ε_r is assumed to be 3, which is a typical value for semiconducting polymers.

2-6. References

1) Facchetti, A. *Chem. Mater.* **2011**, *23*, 733–758.

2) Beaujuge, P. M.; Fréchet, J. M. J. *J. Am. Chem. Soc.* **2011**, *133*, 20009–20029.

3) Boudreault, P.-L. T.; Najari, A; Leclerc, M. *Chem. Mater.* **2011**, *23*, 456–469.

4) Mataka, S.; Takahashi, K.; Ikezaki, Y.; Hatta, T.; Tori-I, A.; Tashiro, M. *Bull. Chem. Soc. Jpn.* **1991**, *64*, 68–73.

5) Wang, M.; Hu, X.; Liu, P.; Li, W.; Gong, X.; Huang, F.; Cao, Y. *J. Am. Chem. Soc.* **2011**, *133*, 9638–9641.

6) Osaka, I.; Shimawaki, M.; Mori, H.; Doi, I.; Miyazaki, E.; Koganezawa, T.; Takimiya, K. *J. Am. Chem. Soc.* **2012**, *134*, 3498–3507.

7) Osaka, I.; Abe, T.; Shimawaki, M.; Koganezawa, T.; Takimiya, K. *ACS Macro Lett.* **2012**, 437–440.

8) Leclerc, M.; Morin, J.-F. eds., *Design and Synthesis of Conjugated Polymers*, Wiley-VCH, Weinheim, Germany, 2010.

9) Chujo, Y. ed., *Conjugated Polymer Synthesis*, Wiley-VCH, Weinheim, Germany, 2010.

10) Ishiyama T.; Takagi, J.; Ishida, K.; Miyaura, N.; Anastasi, N. R.; Hartwig, J. F. *J. Am. Chem. Soc.* **2002**, *124*, 390–391.

11) Ishiyama, T.; Nobuta, Y.; Hartwig, J. F.; Miyaura, N. *Chem. Commun.* **2003**, 2924–2925.

12) Shinamura, S.; Sugimoto, R.; Yanai, N.; Takemura, N.; Kashiki, T.; Osaka, I.; Miyazaki, E.; Takimiya, K. *Org. Lett.* **2012**, *14*, 4718–4721.

13) Nakano, M.; Shinamura, S.; Sugimoto, R.; Osaka, I.; Miyazaki, E.; Takimiya, K. *Org. Lett.* **2012**, *14*, 5448–5451.

14) Szarko, J. M.; Guo, J.; Liang, Y.; Lee, B.; Rolczynski, B. S.; Strzalka, J.; Xu, T.; Loser, S.; Marks, T. J.; Yu, L.; Chen, L. X. *Adv. Mater.* **2010**, *22*, 5468–5472.

15) Guo, X.; Zhou, N.; Lou, S. J.; Hennek, J. W.; Ortiz, R. P.; Butler, M. R.; Boudreault, P.-L. T.; Strzalka, J.; Morin, P.-O.; Leclerc, M.; Navarrete, J. T. L.; Ratner, M. A.; Chen, L. X.; Chang, R. P. H.; Facchetti, A.; Marks, T. J. *J. Am. Chem. Soc.* **2012**, *134*, 18427–18439.

16) Osaka, I.; Saito, M.; Koganezawa, T.; Takimiya, K. *Adv. Mater.* **2014**, *26*, 331–338.

17) He, Z.; Zhong, C.; Su, S.; Xu, M.; Wu, H.; Cao, Y. *Nat. Photon.* **2012**, *6*, 591–595.

18) Etxebarria, I.; Guerrero, A.; Albero, J.; G.-Belmonte, G.; Palomares, E.; Pacios, R. *Organic Electronics* **2014**, *15*, 2756–2762.

19) Xu, Z.; Chen, L.-M.; Yang, G.; Huang, C.-H.; Hou, J.; Wu, Y.; Li, G.; Hsu, C.-S.; Yang, Y. *Adv. Funct. Mater.* **2009**, *19*, 1227–1234.

20) Guo, X.; Zhou, N.; Lou, S. J.; Smith. J.; Tice, D. B.; Hennek, J. W.; Ortiz, R. P.; Navarrete, J. T. L.; Li, S.; Strzalka, J.; Chen, L. X.; Chang, R. P. H.; Facchetti, A.; Marks, T. J. *Nat. Photon.* **2013**, *7*, 825–833.

21) Peet, J.; Wen, L.; Byme, P.; Rodman, S.; Forberich, K.; Shao, Y.; Drolet, N.; Gaudiana, R.; Dennler, G.; Waller, D. *Appl. Phys. Lett.* **2011**, *98*, 043301.

22) Price, S. C.; Stuart, A. C.; Yang, L.; Zhou, H.; You, W. *J. Am. Chem. Soc.* **2011**, *133*, 4625–4631.

23) Li, W.; Hendriks, K. H.; Roelofs, W. S. C.; Kim, Y.; Wienk, M. M.; Janssen, R. A. J. *Adv. Mater.* **2013**, *25*, 3182–3186.

24) Osaka, I.; Kakara, T.; Takemura, N.; Koganezawa, T.; Takimiya, K. *J. Am. Chem. Soc.* **2013**, *135*, 8834–8837.

25) Stuart, A. C.; Tumbleston, J. R.; Zhou, H.; Li, W.; Liu, S.; Ade, H.; You, W. *J. Am. Chem. Soc.* **2013**, *135*, 1806–1815.

26) Liang, Y.; Feng, D.; Wu, Y.; Tsai, S.-T.; Li, G.; Ray, C.; Yu, L. *J. Am. Chem. Soc.* **2009**, *131*, 7792–7799.

27) Sirringhaus, H.; Brown, P. J.; Friend, R. H.; Nielsen, M. M.; Bechgaard, K.; Langeveld-Voss, B. M. W.; Spiering, A. J. H.; Janssen, R. A. J.; Meijer, E. W.; Herwig, P.; de Leeuw, D. M. *Nature* **1999**, *401*, 685–688.

28) Baker, J. L.; Jimison, L. H.; Mannsfeld, S.; Volkman, S.; Yin, S.; Subramanian, V.; Salleo, A.; Alivisatos, A. P.; Toney, M. F. *Langmuir* **2010**, *26*, 9146–9151.

29) Rivnay, J.; Mannsfeld, S. C. B.; Miller, C. E.; Salleo, A.; Toney, M. F. *Chem. Rev.* **2012**, *112*, 5488–5519.

30) Umeda, T.; Kumaki, D.; Tokito, S. *J. Appl. Phys.* **2009**, *105*, 024516.

31) Kline, R. J.; McGehee, M. D.; Toney, M. F. *Nat. Mater.* **2006**, 5, 222–228.

32) Duong, D. T.; Toney, M. F.; Salleo, A. *Phys. Rev. B* **2012**, *86*, 205205.

33) Shrotriya, V.; Yao, Y.; Li, G.; Yang, Y. *Appl. Phys. Lett.* **2006**, 89, 063505.

Chapter 3

Fluorinated PNTz4T (PNTz4TF2 and PNTz4TF4)

3-1. Introduction

A good example of the high performance polymer system is naphtho[1,2-*c*:5,6-*c'*]bis[1,2,5]thiadiazole (NTz)-based polymers, where NTz act as the A unit.[1-4] Of particular interest among the NTz-based polymers is a quaterthiophene–NTz polymer (PNTz4T), which I have previously developed (Figure 3-1).[5, 6] PNTz4T possesses a narrow optical band gap (E_g) of 1.56 eV and highest occupied molecular orbital (HOMO) energy level (E_H) of –5.14 eV and forms crystalline structure and face-on orientation in blend films with [6,6]-phenyl-C_{61}-butyric acid methyl ester ($PC_{61}BM$) or [6,6]-phenyl-C_{71}-butyric acid methyl ester ($PC_{71}BM$). As a consequence, PNTz4T demonstrated PCEs as high as 10.1%, in particular with an inverted cell architecture, in which the distribution of the backbone orientation and the flow of the charge carriers within the cell are well matched. Although the PNTz4T cell exhibited high J_{SCS} of more than 19 mA cm^{-2}, V_{OC} was limited to 0.71–0.74 V due to the moderately deep E_H.[7] These results motivated us to further study on the development of new PNTz4T-related polymers with a deeper E_H and a similarly narrow E_g.

Recently, it was reported that the fluorine atom is a powerful functional group for semiconducting polymers.[8-18] With its strong electron-withdrawing nature, the introduction of fluorine into the polymer backbone can deepen E_H with a minimal change of E_g, resulting in the enhancement of V_{OC} and thereby PCE. It is also believed that fluorine offers some non-covalent attractive interactions such as C-F$\cdots$H and F$\cdots$S, which may contribute to enhance the coplanarity of the polymer backbone and thereby the crystallinity, in turn the performance of PSCs.[18]

In this chapter, I synthesized two new NTz-based polymers by introducing two and four fluorine atoms on the bithiophene moiety of PNTz4T, that are PNTz4TF2 and PNTz4TF4, respectively. I investigated the effect of the fluorine substitution on the electronic structure, ordering structure, and photovoltaic properties.
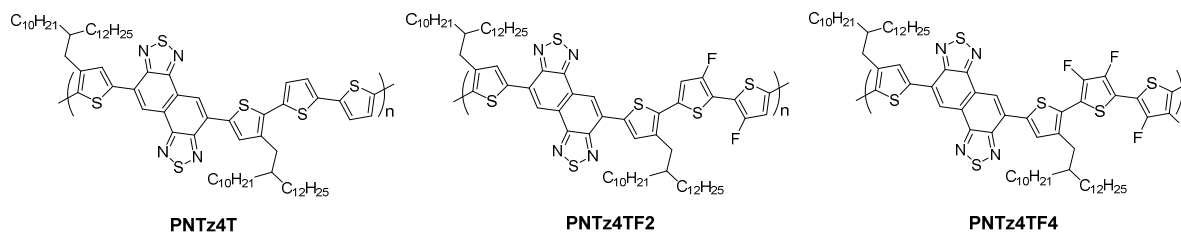
Figure 3-1. Chemical structures of the polymers based on NTz studied in this chapter.

3-2. Results and discussion

3-2-1. Synthesis and properties

The key to accessing the designed polymers is the synthesis of fluorinated bithiophene compounds (Scheme 3-1). 5,5′-bis(trimethylstannyl)-3,3′-difluoro-2,2′-bithiophene (**4**), the monomer for PNTz4TF2, was synthesized with the similar method reported during our study.[11] As for the synthesis of 5,5′-bis(tributylstannyl)-3,3′,4,4′-tetrafluoro-2,2′-bithiophene (**11**), first the α-positions of 3,4-dibromothiophene (**5**) was protected with the triisopropylsilyl (TIPS) group, quantitatively giving **6**, via the lithiation using diisopropylamide (LDA) followed by the treatment with chlorotriisopropylsilane. Then, **6** was difluorinated to give **7** with repeating five times the lithiation with *n*-BuLi and the following treatment with *N*-Fluorobenzenesulfonimide (NFSI)[19] in one-pot with a reasonably high yield of 88%. **7** was monoiodinated (**8**) with iodine monochloride (ICl), which was then dimerized (**9**) via lithiation with *n*-BuLi followed by the oxidative coupling with copper(II) chloride (CuCl₂). **9** was desilylated with tetrabutylammonium fluoride (TBAF), giving **10**, which was then stannylated via lithiation with LDA and treatment with tributyltin chloride to afford **11**. Note that although stannylation of **11** was also successful with trimethyltin chloride, the trimethyltin moiety was found to easily cleave off from the resulting compound in the ambient conditions.

41

**Scheme 3-1.** Synthesis of the fluorinated bithiophene monomers and polymers.
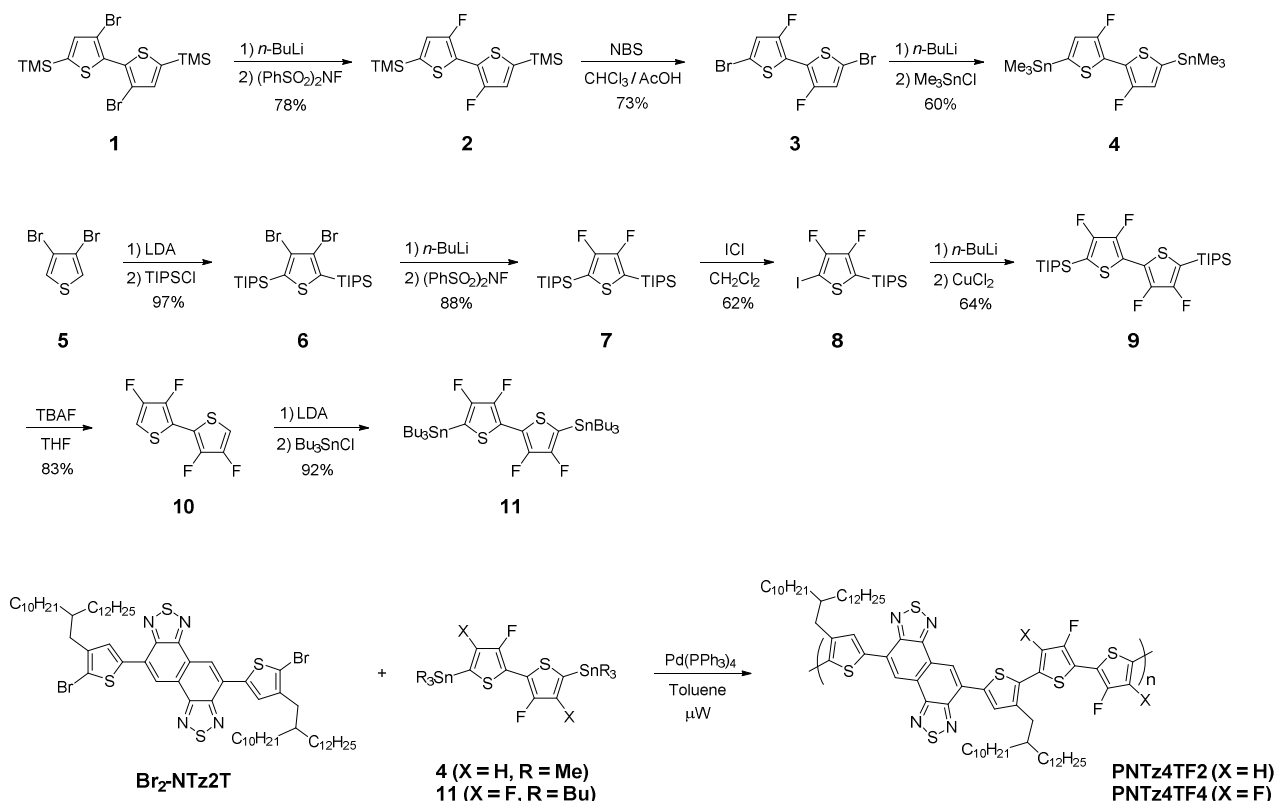
The fluorinated monomers (**4** and **11**) were polymerized with 5,10-bis(5-bromo-4-(2-decyltetradecyl)thiophen-2-yl)naphtho[1,2-c:5,6-c′]bis[1,2,5]thiadiazole (**Br2-NTz2T**) via the Stille coupling reaction associated with microwave heating to give PNTz4TF2 and PNTz4TF4, respectively. The number average molecular weight (M_n) and weight average molecular weight (M_w) were evaluated by high-temperature gel-permeation chromatography (GPC) using o-dichlorobenzene (DCB) as the eluent at 140 °C. M_n and M_w were 66.5 kDa and 1520 kDa with the polydispersity index (PDI) of 22.9 for PNTz4TF2, and 15.8 kDa and 34.1 kDa with PDI of 2.16 for PNTz4TF4, respectively (Table 3-1). PNTz4T was also synthesized with **Br2-NTz2T** and plane bithiophene monomer (5,5′-bis(trimethylstannyl)-2,2′-bithiophene) (M_n = 52.9 kDa, M_w = 113.5 kDa, and PDI = 2.1).[5] The solubility of polymers decreased as the fluorine atom increased. Because of the very low solubility, only a portion of the PNTz4TF4 solution in DCB with the typical concentration for the GPC measurement (0.67 g L^{-1};

5.1×10^{-4} mol/L) was able to pass through a filter, which is technically required for the measurement. This is most likely a cause for the low M_n of PNTz4TF4. The large PDI of 22.9 for PNTz4TF2 comes from a bimodally distributed GPC chromatogram (Figure 3-2), probably owing to the strong aggregation tendency of the polymer that is sometimes seen in D–A polymers.[20, 21] The lower solubility of PNTz4TF2 and PNTz4TF4 is likely due to the enhanced coplanarity and thus the rigidity of the polymer backbone compared to PNTz4T as seen in the geometry-optimized structures of the model compound using the DFT method at the B3LYP/6-31g(d) level as will be discussed later.

Table 3-1. Polymerization results.

Polymer	M_n (kDa)[a]	M_w (kDa)[a]	PDI[a]	$DP_n{}^c$	T_m (°C)[d] heating/cooling	T_{d5} (°C)[e]
PNTz4T	52.9	114	2.16	42.5	321/302	439
PNTz4TF2	66.5	1520	22.9	52.0	–	432
PNTz4TF4	15.8[b]	34.1[b]	2.16	12.0	–	411

[a]Determined by GPC using polystyrene standard and DCB as the eluent at 140 °C. [b]Results with a fraction of the polymer solution after passing through a PTFE filter. [c]Based on the repeating unit. [d]Melting point determined by DSC measurements at a scan rate of 10 °C/min. [e]Temperature of 5% weight loss.
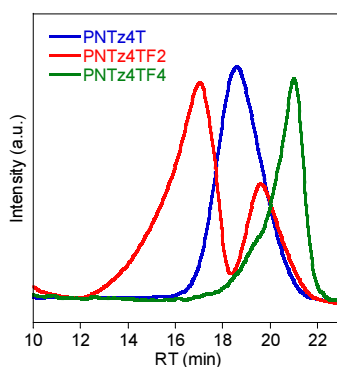
Figure 3-2. GPC charts of PNTz4TFx.

Thermal properties of the polymers were evaluated by the differential scanning calorimetry (DSC) (Figure 3-3a) and thermogravimetry (TG) (Figure 3-3b). While the DSC curve of PNTz4T showed a melting point (T_m) at 321 °C, in the heating process (302 °C in the cooling process), that of PNTz4TF2

and PNTz4TF4 showed no transition peaks below 350 °C. The DSC results suggest that rigidity of the backbone is higher by introduction of fluorine substituents. The temperatures of 5% weight loss (T_{d5}) were 439 °C, 432, and 411 for PNTz4T, PNTz4TF2, and PNTz4TF4, respectively. All polymers have good thermal stability.
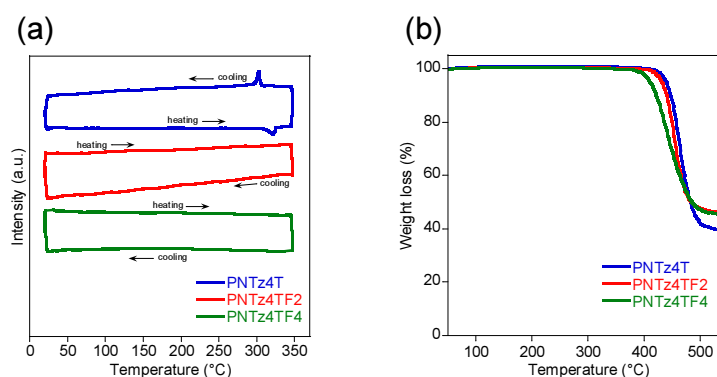

**Figure 3-3.** DSC curves (a) and TGA curves (b) of the polymers.

3-2-2. Physicochemical properties of the polymers

E_H of the polymers was evaluated by the photoelectron spectroscopy in air (PESA) using the thin films (Figure 3-4b). E_H was determined from the onset of the spectra (Table 3-2). E_Hs of PNTz4TF2 and PNTz4TF4 were –5.32 eV and –5.46 eV, respectively, which was deeper than that of PNTz4T (–5.15 eV) by 0.17 eV and 0.31 eV. The lowest unoccupied molecular orbital (LUMO) energy level (E_L) was evaluated by the low-energy inverse photoelectron spectroscopy (LEIPS)[22, 23] using the polymer thin films (Figure 3-4a). E_Ls of PNTz4TF2 and PNTz4TF4 were –3.18 eV and –3.30 eV, respectively, which was also deeper than that of PNTz4T (–3.12 eV) by 0.06 eV and 0.18 eV. These results agree well with E_Hs and E_Ls evaluated with the cyclic voltammetry (CV) (Figure 3-4c), where they were calculated using the redox onset potentials (Table 3-2). Note that although E_Ls were slightly deeper when evaluated by CV, the trend was mostly the same. It should be mentioned that the electronic effect of the fluorine atom was larger on E_H than on E_L in this system. This trend is consistent with the computation of the model compounds, the dimer of the repeat unit with the methyl groups on thiophenes neighboring NTz, by the

DFT method at the B3LYP/6-31g(d) level (Figure 3-5). This can be explained by the geometry of the HOMOs and LUMOs. As depicted in Figure 3-5, whereas the HOMOs are localized on the quaterthiophene moieties, the LUMOs are localized on the NTz moieties. As the fluorine atoms are substituted on the quaterthiophene moieties, it is natural that the downward shift of the E_H is greater than that of the E_L.
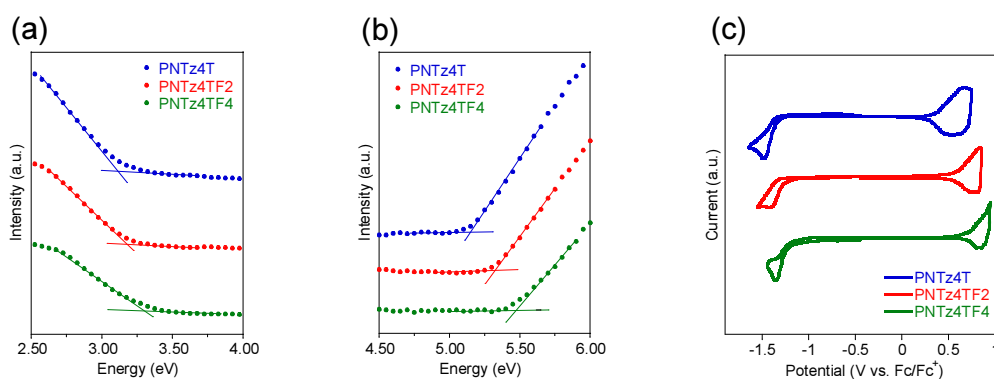

Figure 3-4. LEIPS spectra (a), PESA spectra (b) and cyclic voltammograms (c) of polymer thin films.
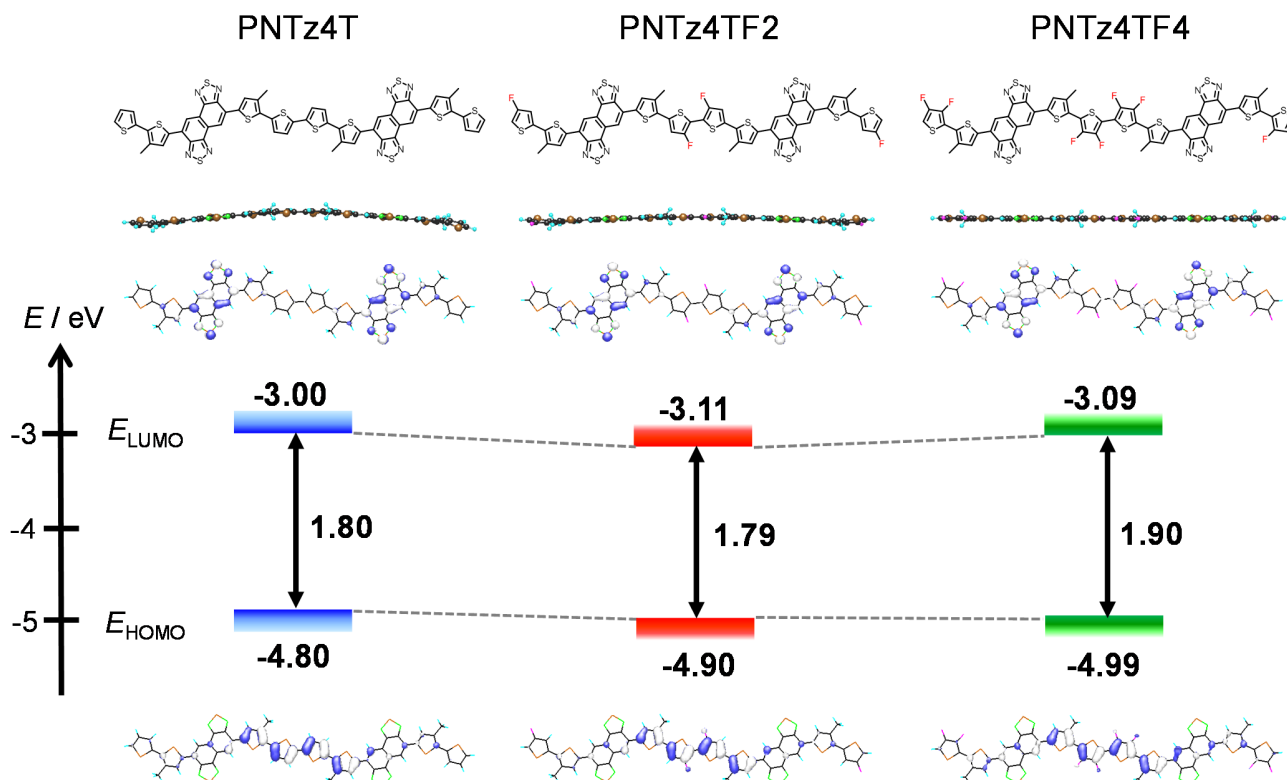
Figure 3-5. The energy levels and geometry of HOMO and LUMO for the polymer repeat unit. Calculations were carried out by the DFT method at the B3LYP/6-31G(d) level on the polymers with a chain length = 2. Alkyl substituents are replaced here by methyl groups to simplify the calculation.

UV-vis absorption spectra of the polymers were measured in chlorobenzene (CB) solution (Figure 3-6a) and in thin film (Figure 3-6b). In both PNTz4TF2 and PNTz4TF4, the spectra in the solution and the film were mostly similar in the absorption range and the shape as is the case in PNTz4T, suggesting that they aggregate, in part, in the solution. This is most likely ascribed to the strong intermolecular interaction. In the thin film, PNTz4TF2 and PNTz4TF4 gave λ_{max} at 697 nm and 688 nm, which was bathochromically shifted by 24 nm and 33 nm compared with PNTz4T (λ_{max} = 721 nm), respectively. E_g of PNTz4TF2 and PNTz4TF4 were calculated to be 1.60 eV and 1.62 eV from the absorption edge (λ_{edge} = 774 nm and 765 nm), which were slightly wider than that of PNTz4T (E_g =1.56 eV, λ_{edge} =793 nm). This is consistent with their E_H and E_L; shift of the E_H is greater than that of the E_L with the introduction of fluorine.
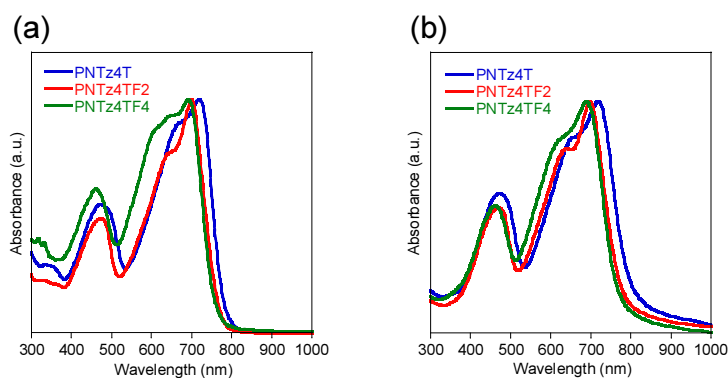
Figure 3-6. UV-vis absorption spectra of the polymers in the chlorobenzene solution (a) and in the thin film (b).

Table 3-2. Physicochemical properties of the polymers.

Polymer	E_H (eV)[a]		E_L (eV)[d]		λ_{max} (nm)[g]		λ_{edge} (nm)[h]	E_g (eV)[i]
	PESA[b]	CV[c]	LEIPS[e]	CV[f]	solution	film		
PNTz4T	−5.15	−5.14	−3.12	−3.46	718	721	793	1.56
PNTz4TF2	−5.32	−5.38	−3.18	−3.53	699	697	774	1.60
PNTz4TF4	−5.46	−5.49	−3.30	−3.56	691	688	765	1.62

a) HOMO energy level. b) E_H evaluated by photoelectron spectroscopy in air (PESA). c) E_H evaluated by cyclic voltammetry (CV). d) LUMO energy level. e) E_L evaluated by low-energy inverse photoelectron spectroscopy (LEIPS). f) E_L evaluated by CV. g) absorption maximum. h) absorption edge. i) optical band gap calculated from λ_{edge} (E_g = 1240/λ_{edge}).

3-2-3. OFET Properties

Transistor characteristics of polymers were evaluated using top-contact, bottom-gate devices fabricated by using polymer thin films spin-coated from o-dichlorobenzene (DCB) (for PNTz4T and PNTz4TF2) or monochlorobenzene (CB)/trichlorobenzene (TCB) mix (1:1) (for PNTz4TF4) solutions onto 1H, 1H, 2H, 2H-perfluorodecyltriethoxysilane (FDTS)[24, 25]-modified Si/SiO$_2$ substrates, which were subsequently annealed at 200 °C for 30 min. In PNTz4TF2 and PNTz4TF4, the devices were again annealed at 150 °C (for PNTz4TF2) or 200 °C (for PNTz4TF4) for 30 min after the deposition of the Au electrodes due to the improved contacts.[26, 27] Figure 3-7 depicts typical transfer and output curves of the polymer-based devices with the FDTS modified substrate. The mobilities (μ_h) evaluated at the saturation regime for PNTz4TF2 was as high as 0.38 cm^2/Vs with the average of 0.29 cm^2/Vs, which was comparable to that of PNTz4T (Table 3-3). On the other hand, μ_h of PNTz4TF4 was slightly lower than those of the others (maximum 0.17 cm^2/Vs, average 0.15 cm^2/Vs). Current on and off ratio were fairly high ($10^7 \sim 10^8$) for all the polymers.
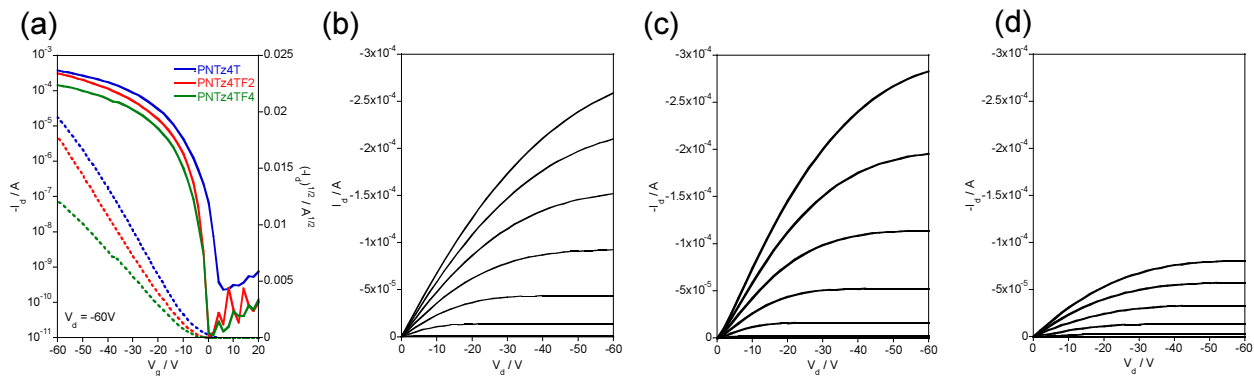

Figure 3-7. Current–voltage characteristics of OFET devices fabricated with polymers on the FDTS-treated Si/SiO$_2$ substrate. Transfer curves of OFET devices using polymers (a), output curves of the devices unsing PNTz4T (b), PNTz4TF2 (c), PNTz4TF4 (d).

Table 3-3. OFET characteristics of the polymers.

| Polymer	μ_h (cm^2/Vs)	V_{th} (V)	on / off
PNTz4T	0.23 (0.18~0.56)	−11.2 ~ 4.7	$\sim 10^8$
PNTz4TF2	0.29 (0.16~0.38)	−9.9 ~ 0.7	$\sim 10^8$
PNTz4TF4	0.15 (0.10~0.17)	−13.3 ~ −5.8	$\sim 10^7$

3-2-4. Thin film structure and morphology

The ordering structures in the thin film were investigated by X-ray diffraction studies. Two-dimensional grazing incidence X-ray diffraction (2D-GIXD) images of PNTz4T, PNTz4TF2 and PNTz4TF4 films on the FDTS-modified SiO_2 substrate, which reflect the ordering structure in the transistors, are shown in Figure 3-8. The diffractions assignable to the lamellar ($q_z \approx 0.28$ Å^{-1}) and the $\pi-\pi$ stacking structures ($q_{xy} \approx 1.8$ Å^{-1}) appear on the q_z and q_{xy} axes, respectively, indicating the predominant edge-on orientation on the substrate surface. The $\pi-\pi$ stacking distance (d_π) for PNTz4TF2 and PNTz4TF4 was calculated to be 3.5 Å, which was comparable to that of PNTz4T. PNTz4TF4 thin films show a somewhat arcing of the diffractions, which reflects misorientation of edge-on lamellae. This difference in orientation in PNTz4TF4 are well-correlated with the transistor properties.
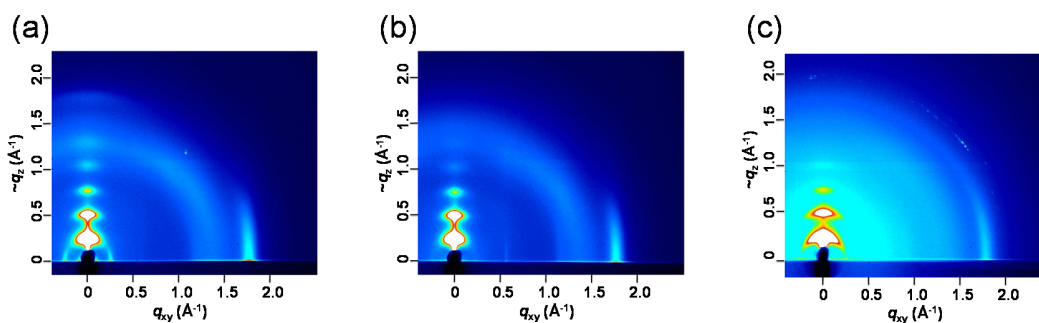
Figure 3-8. 2D GIXD images of polymer thin films fabricated on the FDTS-treated Si/SiO$_2$ substrate. (a) PNTz4T, (b) PNTz4TF2, (c) PNTz4TF4

Morphologies of polymer thin films were investigated by using the atomic force microscopy (AFM). Figure 3-9 displays the topographic AFM images. The obtained root-mean-square roughness (RMS) values for the PNTz4T, PNTz4TF2 and PNTz4TF4 films were 1.00, 2.46 and 4.27 nm, the surface was relatively roughed as the fluorine atom increased. This could possibly originate in the low solubility.

(a)   (b)   (c)
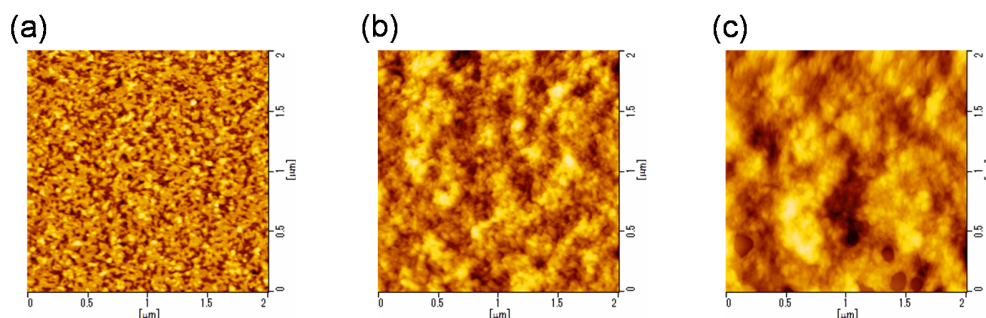
Figure 3-9. AFM height images of the thin films on the actual device treated with FDTS for PNTz4T (a), PNTz4TF2 (b), and PNTz4TF4 (c).

3-2-5. Photovoltaic Properties

Photovoltaic properties of polymers were investigated in an inverted architecture, indium–tin-oxide (ITO)/ZnO/polymer:PC$_{71}$BM/MoO$_x$/Ag, where the active layer was spin-coated from the blend solution in DCB. The optimal polymer to PC$_{71}$BM weight ratio (p/n ratio) was 1:2 for all the polymers. Figures 3-10a and 10b depict the current density (J)–voltage (V) curves and the external quantum efficiency (EQE) spectra of the cells, respectively, and Table 3-4 summarizes the photovoltaic parameters. Note that no processing additives were used at the time of spin coating and no postdeposition treatments such as thermal annealing or solvent vapor treatment were employed. However, due the lower solubility of fluorinated polymers, the ITO/ZnO substrate was heated at 160 °C prior to the spin-coating.

As expected from the deeper E_H, cells based on PNTz4TF2 and PNTz4TF4 exhibited high V_{OC}s of ~0.82 V and ~0.93 V, respectively, compared to PNTz4T cells. Consequently, the photon energy loss (E_{loss}), defined as $E_g – eV_{OC}$, was slightly reduced to 0.78 eV and 0.69 eV for PNTz4TF2 and PNTz4TF4 cells, respectively, from PNTz4T cells (0.85 eV). Interestingly, PNTz4TF2 cells exhibited J_{SC}s similar to the PNTz4T cells despite the narrower spectral response as seen in the EQE spectra. This is due to the high EQEs of PNTz4TF2 cells at the polymer λ_{max} region (~82%), compared to those of the PNTz4T cells (~75%). Notably, although the fill factor (FF) was slightly lower than the PNTz4T cells, PNTz4TF2 cellls overall exhibited quite high PCEs of up to 10.5% (J_{SC} = 19.3 mA/cm², V_{OC} = 0.82 V, FF = 67 %), which is one of the highest efficiencies in single junction solar cells reported so far. In the meantime, while the

V_{OC} of the PNTz4TF4 cells was the highest among the polymers studied here, the J_{SC} was significantly low (~10.5 mA/cm^2), which agrees well with the low EQE of ~51%, resulting in the overall PCEs of 6.5%.

Figure 3-10c–e depict the dependence of J_{SC}, FF, and PCE on the active layer thickness, respectively. J_{SC} of the PNTz4TF2 cells increased as the thickness increased, reflecting the increased volume of the light-absorbing layer, and was maximized at 230 nm. This behavior was similar to that of the PNTz4T cell, though the maximum point for the PNTz4TF2 cells was thinner than for the PNTz4T cells (290 nm). On the other hand, the J_{SC} of the PNTz4TF4 cells was maximized at much smaller thickness, and significantly dropped beyond 200 nm. In all the polymer cells, FF decreased as the thickness increased, which is quite natural considering the extended carrier pathway through the electrodes. In addition, the drop of FF became more significant with the fluorine substitution increased. Overall, the optimal active layer thickness, providing the highest PCEs, was 290 nm, 230 nm and 120 nm for PNTz4T, PNTz4TF2 and PNTz4TF4 cells, respectively.
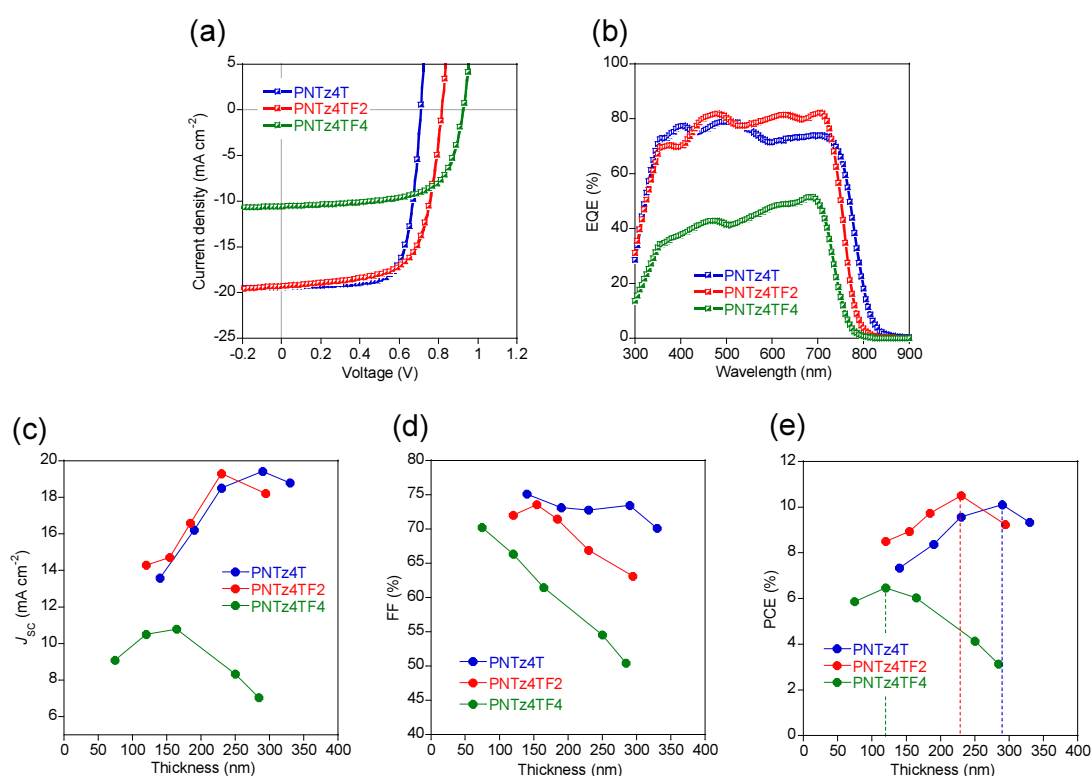
Figure 3-10. *J-V* curves of polymer/PC$_{71}$BM cells with a p/n ratio of 1:2 (a) and EQE spectra of polymer/PC$_{71}$BM cells (b). Thickness dependences of J_{SC} (a), *FF* (b), and PCE (c) of polymer/PC$_{71}$BM (1:2, wt ratio) solar cells.

Table 3-4. Photovoltaic parameters of polymer/PC$_{71}$BM (1:2, wt ratio) solar cells.

polymer	thickness (nm)^a	J_{SC} (mA cm^{-2})^b	J_{SC}^{EQE} (mA cm^{-2})^c	V_{OC} (V)	FF	PCE$_{max}$ [PCE$_{ave}$] (%)^d
PNTz4T	290	19.4	19.4	0.71	0.73	10.1 [9.8]
PNTz4TF2	230	19.3	19.2	0.82	0.67	10.5 [10.1]
PNTz4TF4	120	10.5	10.5	0.93	0.66	6.5 [5.9]

^{a} Thickness of the active layer. ^{b} Short circuit current density observed from the J–V measurement. ^{c} Short circuit current density calculated from the EQE spectra. ^{d} PCE$_{max}$: maximum power conversion efficiency, PCE$_{ave}$: average power conversion efficiency with standard deviation from more than 20 devices.

### 3-2-6. Charge transport properties of the blend films

Charge transport property of the polymer/PCBM films in the direction vertical to the substrate plane was evaluated with hole-only devices (ITO/PEDOT:PSS/polymer:PC$_{71}$BM/MoO$_x$/Ag), where the p/n ratio was 1:2 (Figure 3-11a). The hole mobility was calculated by using the space-charge-limited current (SCLC) model. Whereas hole mobilities of the system of PNTz4T, PNTz4TF2 were 3.4×10^{-3} cm^2 V^{-1} s^{-1} and 1.5×10^{-3} cm^2 V^{-1} s^{-1}, that of the PNTz4TF4 system was 1.8×10^{-4} cm^2 V^{-1} s^{-1}, which is 1 order of magnitude lower (Table 3-5). Hole mobilities of the systems of PNTz4T and PNTz4TF2 are comparable to or greater than those reported for typical high-efficiency polymer systems.[28, 29] To confirm the balance of the charge carrier transport between hole and electron,[30] I also fabricated electron-only devices using the polymer/PC$_{71}$BM blend films (ITO/ZnO/polymer:PC$_{71}$BM/LiF/Al) also with the p/n ratio of 1:2. The electron mobilities of all the polymer systems were of the order of 10^{-3} cm^2 V^{-1} s^{-1}: 1.1×10^{-3}, 2.1×10^{-3} cm^2 V^{-1} s^{-1} and 1.5×10^{-3} cm^2 V^{-1} s^{-1} for the systems of PNTz4T, PNTz4TF2 and PNTz4TF4, respectively (Figure 3-11b). Thus, while the hole and electron transports for systems of PNTz4T and PNTz4F2 are well-balanced, those for the PNTz4TF4 systems is imbalanced. This imbalance should be one of the reasons for the low FF and difficulty of the use of thick active layer, in turn for the limited PCEs.
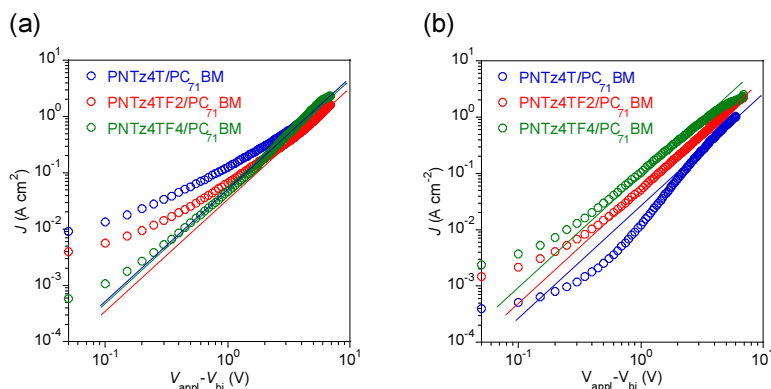
Figure 3-11. *J–V* curves of the hole-only device (ITO/PEDOT:PSS/active layer/MoO$_x$/Ag) (a), *J–V* curves of the electron-only device (ITO/ZnO/active layer/LiF/Al) (b). Measurement at optimal thickness with best device data.

3-2-7. Ordering structure of the polymers in the blend films.

The molecular packing and nanostructural order of the polymers in the active layer were investigated by the two-dimensional grazing incidence X-ray diffraction (2D GIXD) studies using the polymer:PC$_{71}$BM (p/n ratio = 1:2) blend film.[31] Similarly to the PNTz4T film, the PNTz4TF2 film exhibited diffractions at *ca.* 0.25 Å^{-1}, on both the q_z and q_{xy} axis (Figure 3-12). Assuming that the unit cell of the polymer packing was orthorhombic, these diffractions correspond to the lamellar structure, (100), of the crystallite with an edge-on and a face-on orientation, respectively.[32] The PNTz4TF2 film also gave a diffraction on the q_z axis, which corresponds to the π–π stacking structure, (010), of the face-on crystallite, as is the case in the PNTz4T film. The π–π stacking distance (d_π) for PNTz4T and PNTz4TF2 was calculated to be 3.53 Å and 3.49 Å, respectively. In the meantime, in PNTz4TF4, both the lamellar and π–π stacking diffractions were observed as ring, indicating that the crystallites were rather randomly orientated. Nevertheless, d_π of PNTz4TF4 was 3.46 Å, which was comparable to that of PNTz4T and PNTz4TF2.
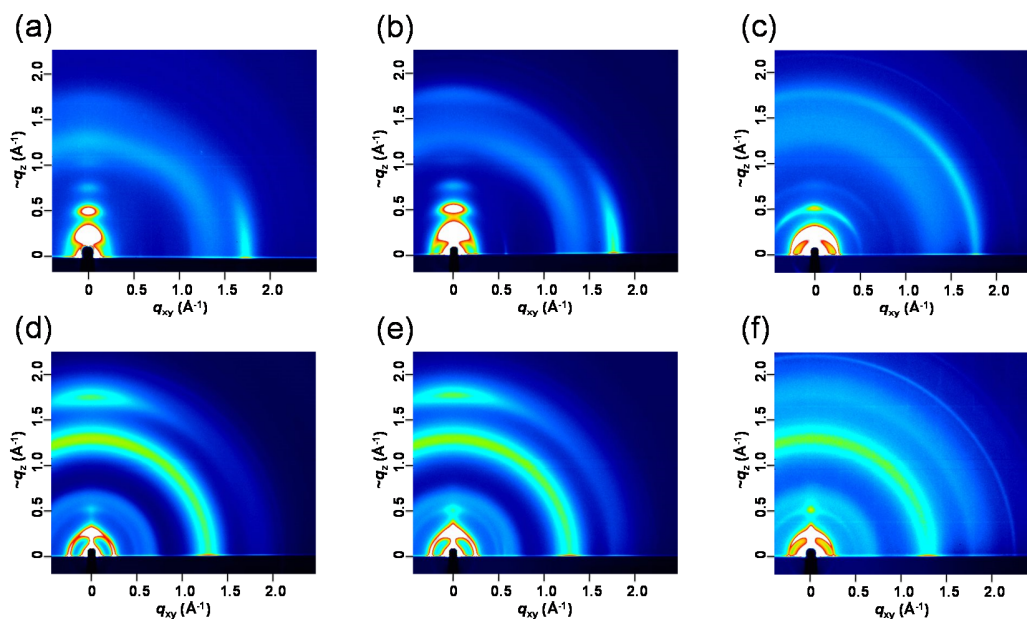
Figure 3-12. (a–c) 2D GIXD images of the neat films on ZnO/ITO substrate for PNTz4T (a), PNTz4TF2 (b), and PNTz4TF4 (c). (d–f) 2D GIXD images of the blend films on ZnO/ITO substrate for PNTz4T (d), PNTz4TF2 (e), and PNTz4TF4 (f).
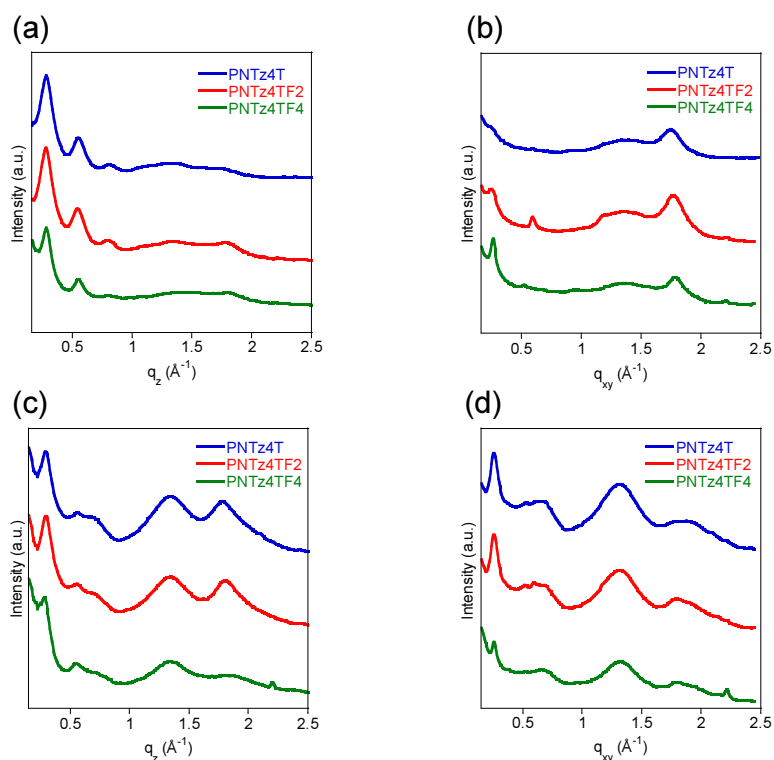
Figure 3-13. The cross-sectional profiles of the neat films on ZnO/ITO substrate along the q_z and q_{xy} axes, respectively (a, b). The cross-sectional profiles of the blend films on ZnO/ITO substrate along the q_z and q_{xy} axes, respectively (c, d).

The orientation was further studied quantitatively using the pole figure analysis of the blend films.[7, 31] Figure 3-14 shows the pole figures extracted from the lamellar diffraction, (100), of the polymers. I defined the areas integrated with polar angle χ ranges of 0–45° and 135–180° (A_{xy}) and 55–125° (A_z) as those corresponding to the fractions of face-on and edge-on crystallites, respectively, and the ratio of A_{xy} to A_z (A_{xy}/A_z) was calculated as a figure for the face-on to edge-on ratio. I note that A_{xy}/A_z may not show the actual face-on to edge-on ratio since the orientation of the backbone long axis is random in these films, which may not provide the comparable data between the q_z and q_{xy} directions. A_{xy}/A_z for PNTz4TF2 was 0.62, which was lower than that for PNTz4T, namely 0.81. This means that the population of the face-on crystallite is smaller in PNTz4TF2 than in PNTz4T. Although the orientation of PNTz4TF4 is basically random, I also calculated A_{xy}/A_z, which was 0.36. Thus, the face-on fraction was reduced by an increase of fluorine on the bithiophene moiety in this system.
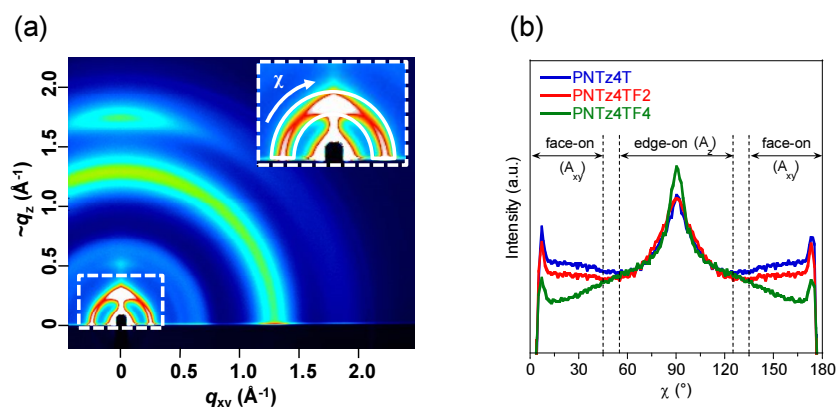
Figure 3-14. Typical 2D GIXD image of the blend film on the ITO/ZnO substrate. Insets: close-up of the lamellar, (100), diffraction region (a). Pole figures extracted from the lamellar diffraction for the blend films. Definition of the polar angle (χ) range corresponding to the edge-on (A_z) and face-on (A_{xy}) crystallites are shown (b).

Crystallinity of the polymers was evaluated by calculating the coherence length (L_C) of the π–π stacking structures in the face-on crystallite by using the Scherrer equation with the full-width-at-half-maximum (FWHM) of the diffraction peak (Table 3-5).[33, 34] While the L_C for PNTz4TF2 (2.9 nm) was similar to

that for PNTz4T (2.7 nm), that for PNTz4TF4 (1.5 nm) was approximately half of those for PNTz4T and PNTz4TF2, despite the fact that PNTz4TF4 is expected to have the most coplanar backbone among the three polymers according to the computation. This could possibly originate in the low solubility of PNTz4TF4. It is speculated that due to the low solubility, PNTz4TF4 nucleates quickly from the solution, which prevents the polymer chains to self-organize into well-ordered structure, in turn resulting in the lower crystallinity and random orientation. In PNTz4T and PNTz4TF2 with higher solubility than PNTz4TF4 can have sufficient time for self-organization before nucleation, affording higher crystallinity. These differences in orientation and crystallinity in the series of polymer are well-correlated with the photovoltaic properties.

Table 3-5. Charge carrier mobilities and parameters for the ordering structures.

| Polymer | Mobility (cm^2 V^{-1} s^{-1})[a] | | A_{xy}/A_z[b] | lamellar | π–π stacking | | |
	hole	electron		d_l (Å)[c] [q_{xy} (Å^{-1})]	d_π (Å)[d] [q_z (Å^{-1})]	FWHM (Å^{-1})[e]	L_C (nm)[f]
PNTz4T	3.4×10^{-3}	1.1×10^{-3}	0.81	24.7 [0.254]	3.53 [1.78]	0.23	2.7
PNTz4TF2	1.5×10^{-3}	2.1×10^{-3}	0.62	24.7 [0.254]	3.49 [1.80]	0.22	2.9
PNTz4TF4	1.8×10^{-4}	1.5×10^{-3}	0.36	24.7 [0.254]	3.46 [1.82]	0.41	1.5

[a] Hole and electron mobilities evaluated with the hole-only devices (ITO/PEDOT:PSS/active layer/MoOx/Ag) and electron-only devices (ITO/ZnO/active layer/LiF/Al), respectively, in which the active layer are the polymer/PC$_{71}$BM blend films. [b] Area ratio corresponding to the edge-on (A_z) and face-on (A_{xy}) crystallites, respectively. [c] d spacing correspond to the lamellar structure (100) along the q_{xy} axis (in-plane direction). [d] d spacing correspond to the π–π stacking (010) along the q_z axis (out-of-plane direction). [e] full width at half maximum. [f] crystallite coherence length ($Lc = 2\pi/$FWHM).

The surface morphology of the polymer/PC$_{71}$BM blend films was investigated by using the atomic force microscopy (AFM). Figure 3-15 displays the topographic AFM images. Whereas the PNTz4TF2 film exhibited a morphology with finely separated domains similar to the PNTz4T film, the PNTz4TF4 film exhibited a morphology with larger domains. The obtained root-mean-square roughness (RMS) values for the PNTz4T and PNTz4TF2 films were 0.97, 1.01, indicative of fairy smooth surfaces. On the

other hand, the RMS value for the PNTz4TF4 film was 3.06 nm, suggesting that the surface was relatively rough, which is consistent with the morphology. The nicely phase separated structure and the smooth surface of the PNTz4TF2 film and large domains with the rough surface of the PNTz4TF4 film compared to PNTz4T agree well with the trend in the photovoltaic performance.
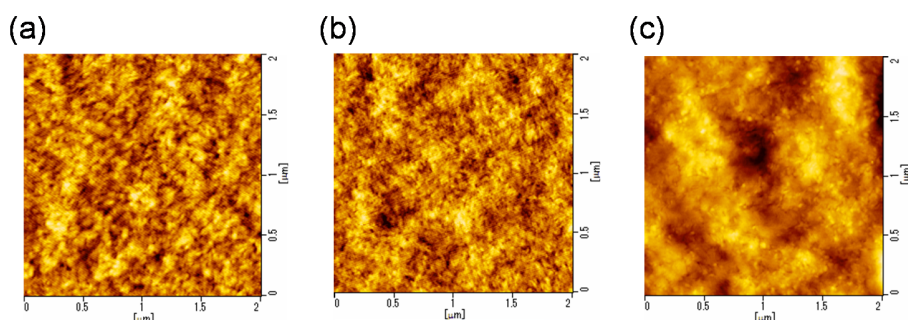
Figure 3-15. AFM height images of the blend films on the actual device for PNTz4T (a), PNTz4TF2 (b), and PNTz4TF4 (c).

3-3. Conclusion of chapter3

I synthesized two types of fluorinated NTz-based polymers with different numbers of fluorine on bithiophene unit, having two and four fluorine, namely, PNTz4TF2 and PNTz4TF4, respectively. Compared to non-fluorinated polymer, PNTz4T, fluorinated polymers have deeper HOMO levels without large change of optical bandgap and exhibit stronger vibrionic solder in UV-spectra. PNTz4TF2 based-cell exhibits higher PCE of 10.5% than PNTz4T (10.1%), which is among the highest for PSCs with a single BHJ structure. On the other hand, PNTz4TF4 exhibits lower PCE of 6.5%. PNTz4TF4 has the relative low solubility and poor film quality in comparison with PNTz4T, PNTz4TF2. This may contribute unfavorable factor for the mobility, orientation and crystallinity.

Our results indicate that the physicochemical properties and device performance of PSCs can be easily tuned by introduction of fluorine atom on polymer backbone. It is also suggested that the improvement of solubility of polymers is key to enable to achieving high performance polymer solar cells.

3-4. Experimental section

Synthesis

3,4-Dibromothiophene (**5**) was purchased from Tokyo Chemical Industry Co., Ltd. 3,3′-Dibromo-5,5′-bis(trimethylsilyl)-2,2′-bithiophene (**1**),[35] 5,10-Bis(5-bromo-4-(2-decyltetradecyl)thiophen-2-yl)-naphtho[1,2-c:5,6-c′]bis[1,2,5]thiadiazole (Br$_2$-NTz2T)[5] were synthesized according to the reported procedure. All chemicals and solvents are of reagent grade unless otherwise indicated. THF and toluene were purified by a Glass Contour Solvent System (Nikko Hansen & Co., Ltd.) prior to use. Polymerization was carried out with a microwave reactor (Biotage Initiator). Nuclear magnetic resonance (NMR) spectra were obtained in deuterated chloroform (CDCl$_3$) and o-dichlorobenzene (o-DCB-d$_4$) (for polymers) with TMS and C$_6$F$_6$ (for ^{19}F NMR) as internal reference by using a JNM-ECS400 (JEOL RESONANCE). EI-MS spectra were obtained with a GCMS-QP-2010SE spectrometer (SHIMADZU) using an electron impact ionization procedure (70 eV). The molecular ion peaks of the fluorine-, chlorine-, bromine-, iodine, sulfur-, or tin-containing compounds showed a typical isotropic pattern, and all the mass peaks are reported based on ^{19}F, ^{35}Cl, ^{79}Br, ^{127}I, ^{32}S, or ^{120}Sn, respectively. Molecular weights were determined by gel permeation chromatography (GPC) by calibrating with polystyrene standards using a TOSOH HLC-8121GPC/HT at 140 °C with DCB as a solvent.

3,3′-Difluoro-5,5′-bis(trimethylsilyl)-2,2′-bithiophene (2)

To a solution of **1** (5.00 g, 10.7 mmol) in THF (50 mL) was added 1.64 M n-BuLi in hexane (6.9 mL, 11.3 mmol) slowly at –78 °C under nitrogen, and the mixture was stirred at -78 °C for 15 min. N-Fluorobenzenesulfonimide (NFSI, 3.57 g, 11.3 mmol) was added in one portion, and the resulting mixture was stirred at –78 °C for 30 min. Further lithiation and fluorination were repeated four times with n-BuLi (3.5 mL, 5.74 mmol), NFSI (1.81 g, 5.74 mmol), n-BuLi (1.7 mL, 2.79 mmol), NFSI (0.88 g, 2.79 mmol), n-BuLi (0.9 mL, 1.48 mmol), NFSI (0.45 g, 1.43 mmol), n-BuLi (0.9 mL, 1.48 mmol), and NFSI (0.68 g, 2.16 mmol). The reaction mixture was allowed to warm to room temperature and stirred for 2 h. Then,

1N HCl was added to quench the reaction and the mixture was extracted with ether. The organic layer was washed with water, and then dried over anhydrous $MgSO_4$. After removal of the solvent, the residue was suspended in hexane and filtered. The filtrate was concentrated by vacuum evaporation, and the residue was purified by column chromatography on silica gel with hexane to give **2** as a pale yellow oil (2.88 g, 78%). ^{1}H NMR (400 MHz, $CDCl_3$): δ 6.95 (s, 2H), 0.32 (s, 18H). ^{13}C NMR (100 MHz, $CDCl_3$): δ 155.1 (d, $J = 266$ Hz), 138.0–138.2 (m), 123.1 (d, $J = 23.3$ Hz), 116.6 (dd, $J = 17.5, 6.9$ Hz), –0.55. ^{19}F NMR (376 MHz, $CDCl_3$): δ –131.0 (s, 2F). EI-MS (70 eV) m/z 346 (M$^+$).

5,5′-Dibromo-3,3′-difluoro-2,2′-bithiophene (3)

To a solution of **2** (1.00 g, 2.89 mmol) in chloroform (12.5 mL) and acetic acid (12.5 mL) was added N-Bromosuccinimide (NBS, 1.03 g, 5.78 mmol) at room temperature. The mixture was stirred for 22 h at 50 °C. After cooling at room temperature, the mixture was poured into a saturated aqueous solution of $NaHSO_3$. The mixture was extracted with ether. The organic layer was washed with $NaHCO_3$ aq. and water, and then dried over anhydrous $MgSO_4$. The solvent was removed by vacuum evaporation, the residue was purified by column chromatography on silica gel with hexane, and subsequently by preparative GPC (JAIGEL 1H–2H, $CHCl_3$ as the eluent) to give **3** as a white solid (0.76 g, 73%). ^{1}H NMR (400 MHz, $CDCl_3$): δ 6.86 (s, 2H). ^{13}C NMR (100 MHz, $CDCl_3$): δ 151.9 (d, $J = 267$ Hz), 120.1 (d, $J = 26.8$ Hz), 112.3 (dd, $J = 16.2, 5.7$ Hz), 111.3–111.6 (m). ^{19}F NMR (376 MHz, $CDCl_3$): δ –126.5 (s, 2F). EI-MS (70 eV) m/z 360 (M$^+$).

3,3′-Difluoro-5,5′-bis(trimethylstannyl)-2,2′-bithiophene (4)

To a solution of **3** (0.36 g, 1.00 mmol) in THF (15 mL) was added 1.64 M n-BuLi in hexane (1.4 mL, 2.30 mmol) slowly at –78 °C under nitrogen, and the mixture was stirred at the same temperature for 30 min. The resulting solution was allowed to warm to room temperature. It was kept at this temperature for 30 min and subsequently cooled to –78 °C. Trimethylstannyl chloride (0.50 g, 2.51 mmol) was added in

one portion. The reaction mixture was allowed to warm to room temperature and stirred for 2 h. Water was added to quench the reaction. The resulting mixture was extracted with ether. The organic layer was washed with water, and then dried over anhydrous $MgSO_4$. The solvent was removed by vacuum evaporation, and the residue was purified by recrystallization twice from acetonitrile to give **4** as a white solid (0.32 g, 60%). ^{1}H NMR (400 MHz, $CDCl_3$): δ 6.89 (s, 2H), 0.39 (s, 18H). ^{13}C NMR (100 MHz, $CDCl_3$): δ 155.4 (d, J = 267 Hz), 135.9–136.2 (m), 124.3 (d, J = 22.9 Hz), 117.1 (dd, J = 17.9, 6.6 Hz), – 8.29. ^{19}F NMR (376 MHz, $CDCl_3$): δ –132.6 (s, 2F). EI-MS (70 eV) m/z 530 [M(^{120}Sn, ^{120}Sn)]$^+$, 528 [M(^{118}Sn, ^{120}Sn)]$^+$.

3,4-Dibromo-2,5-bis(triisopropylsilyl)thiophene (6).

To a solution of diisopropylamine (32.5 mL, 231.2 mmol) in THF (250 mL) was added 1.61 M n-BuLi in hexane (142 mL, 228.6 mmol) slowly at –78 °C under nitrogen, and the mixture was stirred at -78 °C for 15 min. The resulting solution was allowed to warm to 0 °C. It was kept at this temperature for 1 h and subsequently cooled to –78 °C. 3,4-Dibromothiophene (**5**) was then added dropwise slowly, and the resulting solution was stirred at –78 °C for 1 h. Triisopropylsilyl chloride (54 mL, 245.9 mmol) was added dropwise. The reaction mixture was then allowed to warm to room temperature and stirred overnight. Water was added to quench the reaction. The resulting mixture was extracted with hexane. The organic layer was washed with water, and then dried over anhydrous $MgSO_4$. The solvent was removed by vacuum evaporation, and the residue was purified by column chromatography on silica gel with hexane, followed by recrystallization from isopropanol/water to give **6** as a white solid (55.7 g, 97%). ^{1}H NMR (400 MHz, $CDCl_3$): δ 1.61 (sept, J = 7.5 Hz, 6H), 1.13 (d, J = 7.5 Hz, 36H). ^{13}C NMR (100 MHz, $CDCl_3$): δ 137.6, 122.5, 18.8, 12.2. EI-MS (70 eV) m/z 554 (M$^+$). Anal. Calcd for $C_{22}H_{42}Br_2SSi_2$: C, 47.64; H, 7.63. Found: C, 47.92; H, 7.68.

3,4-Difluoro-2,5-bis(triisopropylsilyl)thiophene (7).

To a solution of **6** (19.9 g, 36.5 mmol) in THF (200 mL) was added 1.55 M *n*-BuLi in hexane (26.0 mL, 40.3 mmol) slowly at –78 °C under nitrogen, and the mixture was stirred at -78 °C for 15 min. *N*-Fluorobenzenesulfonimide (NFSI, 13.3 g, 42.2 mmol) was added in one portion, and the resulting mixture was stirred at –78 °C for 30 min. Further lithiation and fluorination were repeated four times with *n*-BuLi (13.0 mL, 20.2 mmol), NFSI (6.6 g, 20.9 mmol), *n*-BuLi (6.5 mL, 10.1 mmol), NFSI (3.3 g, 10.5 mmol), *n*-BuLi (3.3 mL, 5.1 mmol), NFSI (1.7 g, 5.4 mmol), *n*-BuLi (3.3 mL, 5.1 mmol), and NFSI (1.7 g, 5.4 mmol). The reaction mixture was allowed to warm to room temperature and stirred for 2 h. Then, 1N HCl was added to quench the reaction and the mixture was extracted with hexane. The organic layer was washed with water, and then dried over anhydrous MgSO$_4$. After removal of the solvent, the residue was suspended in hexane and filtered. The filtrate was concentrated by vacuum evaporation, and the residue was purified by column chromatography on silica gel with hexane to give **7** as a white solid (13.9 g, 88%). ^{1}H NMR (400 MHz, CDCl$_3$): δ 1.38 (sept, *J* = 7.5 Hz, 6H), 1.10 (d, *J* = 7.5 Hz, 36H). ^{13}C NMR (100 MHz, CDCl$_3$): δ 151.0 (dd, *J* = 261, 25.1 Hz), 116.9 (m), 18.5, 11.5. ^{19}F NMR (376 MHz, CDCl$_3$): δ –130.5 (s, 2F). EI-MS (70 eV) *m/z* 432 (M$^+$). HRMS (EI) m/z calcd for C$_{22}$H$_{42}$F$_2$SSi$_2$ [M]$^+$: 432.2514. Found: 432.2496.

3,4-Difluoro-5-iodo-2-(triisopropylsilyl)thiophene (8).

To a solution of **7** (2.35 g, 5.43 mmol) in dichloromethane (40 mL) was added 1.0 M ICl in dichloromethane (8.2 mL, 8.20 mmol) slowly at room temperature. The mixture was stirred for 18 h at the same temperature and then poured into a saturated aqueous solution of NaHSO$_3$. The mixture was extracted with dichloromethane. The organic layer was washed with NaHCO$_3$ aq. and water, and then dried over anhydrous MgSO$_4$. The solvent was removed by vacuum evaporation, and the residue was purified by column chromatography on silica gel with hexane to give **8** as colorless oil (2.69 g, 62%). ^{1}H NMR (400 MHz, CDCl$_3$): δ 1.35 (sept, *J* = 7.4 Hz, 3H), 1.10 (d, *J* = 7.4 Hz, 18H). ^{13}C NMR (100 MHz,

CDCl$_3$): δ 149.3 (dd, J = 264, 24.9 Hz), 149.1 (dd, J = 261, 19.0 Hz), 117.6 (d, J = 27.7 Hz), 57.9 (dd, J = 23.0, 2.5 Hz), 18.4, 11.5. ^{19}F NMR (376 MHz, CDCl$_3$): δ –125.6 (d, J = 15.2 Hz, 1F), –131.3 (d, J = 15.2 Hz, 1F). EI-MS (70 eV) m/z 402 (M$^+$). HRMS (EI) m/z calcd for C$_{13}$H$_{21}$F$_2$ISSi [M]$^+$: 402.0146. Found: 402.0158.

3,3′,4,4′-Tetrafluoro-5,5′-bis(triisopropylsilyl)-2,2′-bithiophene (9)

To a solution of **8** (1.33 g, 3.31 mmol) in ether (25 mL) was added 1.61 M n-BuLi in hexane (2.2 mL, 3.54 mmol) slowly at –78 °C under nitrogen, and the mixture was stirred at the same temperature for 1 h. Anhydrous CuCl$_2$ (0.67 g, 4.96 mmol) was added in one portion, and it was kept at this temperature for 1 h and subsequently allowed to warm to room temperature and stirred overnight. Then, 1N HCl was added to quench the reaction and the mixture was extracted with hexane. The organic layer was washed with NaHCO$_3$ aq. and water, and then dried over anhydrous MgSO$_4$. The solvent was removed by vacuum evaporation, and the residue was purified by column chromatography on silica gel with hexane, followed by recrystallization from methanol to give **9** as a white solid (0.58 g, 64%). ^{1}H NMR (400 MHz, CDCl$_3$): δ 1.40 (sept, J = 7.5 Hz, 6H), 1.12 (d, J = 7.5 Hz, 36H). ^{13}C NMR (100 MHz, CDCl$_3$): δ 150.0 (dd, J = 257, 17.6 Hz), 142.3 (dd, J = 270, 26.0 Hz), 116.1 (d, J = 5.8 Hz), 110.0 (dd, J = 27.2, 3.9 Hz), 18.4, 11.6. ^{19}F NMR (376 MHz, CDCl$_3$): δ –128.3 (d, J = 13.4 Hz, 2F), –137.1 (d, J = 13.4 Hz, 2F). EI-MS (70 eV) m/z 550 (M$^+$). HRMS (EI) m/z calcd for C$_{26}$H$_{42}$F$_4$S$_2$Si$_2$ [M]$^+$: 550.2203. Found: 550.2197.

3,3′,4,4′-Tetrafluoro-2,2′-bithiophene (10)

To a solution of **8** (2.00 g, 3.63 mmol) in THF (20 mL) was added 1.0 M tetrabutylammonium fluoride in THF (TBAF, 21.8 mL, 21.8 mmol) at 0 °C. The mixture was allowed to warm to room temperature and stirred for 12 h. Water was added to quench the reaction. The resulting mixture was extracted with hexane. The organic layer was washed with water, and then dried over anhydrous MgSO$_4$. The solvent was removed by vacuum evaporation, and the residue was purified by column chromatography on silica gel

with hexane, and subsequently by preparative GPC (JAIGEL 1H–2H, CHCl$_3$ as the eluent) to give **10** as a white solid (0.71 g, 83%). ^{1}H NMR (400 MHz, CDCl$_3$): δ 6.74–6.78 (m, 2H). ^{13}C NMR (100 MHz, CDCl$_3$): δ 145.3 (dd, J = 262, 19.2 Hz), 142.0 (dd, J = 267, 20.8 Hz), 110.8 (d, J = 6.0 Hz), 102.5 (dt-like, J = 15.5, 4.3 Hz). ^{19}F NMR (376 MHz, CDCl$_3$): δ –138.1 (d, J = 12.3 Hz, 2F), –139.5 (d, J = 12.3 Hz, 2F). EI-MS (70 eV) m/z 238 (M$^+$). HRMS (EI) m/z calcd for C$_8$H$_2$F$_4$S$_2$ [M]$^+$: 237.9534. Found: 237.9539.

3,3′,4,4′-Tetrafluoro-5,5′-bis(tributylstannyl)-2,2′-bithiophene (11)

To a solution of **10** (0.30 g, 1.26 mmol) in THF (15 mL) was added 1.13 M LDA in hexane/THF (1.35 mL, 1.53 mmol) slowly at –78 °C under nitrogen, and the mixture was stirred at the same temperature for 40 min. Tributylstannyl chloride (0.42 ml, 1.55 mmol) was added in one portion, and the resulting mixture was stirred at the same temperature for 40 min. Further lithiation and stannylation were repeated two times with LDA (1.35 mL, 1.53 mmol), tributylstannyl chloride (0.42, 1.55 mmol), LDA (1.35 mL, 1.53 mmol) and tributylstannyl chloride (0.42, 1.55 mmol). The reaction mixture was allowed to warm to room temperature and stirred for 2 h. Water was added to quench the reaction. The resulting mixture was extracted with hexane. The organic layer was washed with water, and then dried over anhydrous MgSO$_4$. The solvent was removed by vacuum evaporation, and the residue was purified by preparative GPC (JAIGEL 1H–2H, CHCl$_3$ as the eluent) to give **11** as yellow oil (0.94 g, 89%). ^{1}H NMR (400 MHz, CDCl$_3$): δ 1.45–1.68 (m, 12H), 1.29–1.40 (m, 12H), 1.08–1.37 (m, 12H), 0.91 (t, J = 7.3 Hz, 18H). ^{13}C NMR (100 MHz, CDCl$_3$): δ 150.5 (dd, J = 250, 17.0 Hz), 142.4 (dd, J = 271, 27.4 Hz), 117.1 (d, J = 7.6 Hz), 111.6 (d, J = 39.2 Hz), 28.8, 27.1, 13.6, 10.9. ^{19}F NMR (376 MHz, CDCl$_3$): δ –131.0 (d, J = 15.0 Hz, 2F), –139.4 (d, J = 15.0 Hz, 2F). EI-MS (70 eV) m/z 818 [M(^{120}Sn, ^{120}Sn)]$^+$, 816 [M(^{118}Sn, ^{120}Sn)]$^+$, 814 [M(^{118}Sn, ^{118}Sn and ^{116}Sn, ^{120}Sn)]$^+$, 759 [M–Bu]$^+$. HRMS (EI) m/z calcd for C$_{32}$H$_{54}$F$_4$S$_2$^{120}Sn$_2$ [M]$^+$: 818.1647. Found: 818.1660.

PNTz4TF2

Br$_2$-NTz2T (62.0 mg, 0.05 mmol), **4** (26.4 mg, 0.05 mmol), tetrakis(triphenylphosphine)palladium(0) (1.2 mg, 1 μmol) and toluene (2 mL) were added in a 2 mL reaction vessel. The vessel was purged with argon and subsequently sealed. The vessel was put into a microwave reactor and heated at 160 °C for 1.5 h. After cooling to room temperature, the reaction mixture was poured into a mixture of methanol (100 mL) and concentrated hydrochloric acid (5 mL), and then vigorously stirred for 6 h at room temperature. The precipitate was filtered and subjected to sequential Soxhlet extraction with methanol, hexane, chloroform to remove low molecular weight fraction. The residue was extracted with CB, which was reprecipitated in methanol. The precipitate was filtered and dried in vacuo, yielding PNTz4TF2 (58 mg, 91%) as metallic purple solid. GPC (DCB, 140 °C): M_n = 66.5 kDa, M_w = 1520.5 kDa, PDI = 22.9. ^{1}H NMR (400 MHz, DCB-d_4, 150 °C): δ 9.12 (br s, 2H), 8.33 (br s, 2H), 7.12 (m, 2H), 3.00 (m, 4H), 2.05 (m, 2H), 1.18–1.61 (m, 80H), 0.84 (m, 12H). Anal. Calcd for C$_{74}$H$_{104}$F$_2$N$_4$S$_6$: C, 69.44; H, 8.19; N, 4.38. Found: C, 69.34; H, 8.20; N, 4.31.

PNTz4TF4

Br$_2$-NTz2T (62.0 mg, 0.05 mmol), **11** (40.8 mg, 0.05 mmol), tetrakis(triphenylphosphine)palladium(0) (1.2 mg, 1 μmol) and toluene (2 mL) were added in a 2 mL reaction vessel. The vessel was purged with argon and subsequently sealed. The vessel was put into a microwave reactor and heated at 140 °C for 48 min. After cooling to room temperature, the reaction mixture was poured into a mixture of methanol (100 mL) and concentrated hydrochloric acid (5 mL), and then vigorously stirred for 6 h at room temperature. The precipitate was filtered and subjected to sequential Soxhlet extraction with methanol, hexane, chloroform and 1,1,2-trichloroethane to remove low molecular weight fraction. The residue was extracted with CB, which was reprecipitated in methanol. The precipitate was filtered and dried in vacuo, yielding PNTz4TF4 (41 mg, 62%) as metallic purple solid. GPC (DCB, 140 °C): M_n = 15.8 kDa, M_w = 34.1 kDa, PDI = 2.16. ^{1}H NMR (400 MHz, DCB-d_4, 150 °C): 9.14 (s, 2H), 8.36 (s, 2H), 2.95 (m, 4H), 2.02 (m, 2H),

1.18–1.58 (m, 80H), 0.84 (m, 12H). Anal. Calcd for $C_{74}H_{102}F_4N_4S_6$: C, 67.54; H, 7.81; N, 4.26. Found: C, 67.34; H, 7.97; N, 4.16.

Materials. $PC_{61}BM$ and $PC_{71}BM$ were purchased from Frontier Carbon. The patterned ITO-coated glass substrates were purchased from Atsugi Micro.

Instrumentation

Cyclic voltammograms were recorded on an ALS Electrochemical Analyzer Model 612D with the three electrode system consisting of a platinum disc working electrode (φ = 3 mm), a platinum wire counter electrode, and an Ag/AgCl reference electrode in a acetonitrile solution containing tetrabutylammonium hexafluorophosphate (0.1 M) at a scan rate of 100 mVs^{-1}. Polymer thin films were cast from DCB solutions on the ITO, which was then connected to the working electrode. All the potentials were calibrated with the half-wave potential of the ferrocene/ferrocenium redox couple measured under identical condition. UV-vis absorption spectra were recorded on a Shimadzu UV-3600 spectrometer. Photoelectron spectra were recorded on a Model AC-2 photoelectron spectrometer (Riken Keiki Co., Ltd.) in air. Ionization potentials were determined from the onset potentials of the photoelectron spectra. Differential scanning calorimetry (DSC) analysis was carried out with an EXSTAR DSC7020 (SII Nanotechnology, Inc.) at a cooling and heating rate of 10 °C min^{-1}. 2D GIXD experiments were conducted at SPring-8 on beamline BL46XU. The samples were irradiated with an X-ray energy of 12.39 keV (λ = 1 Å) at a fixed incident angle of 0.12° through a Huber diffractometer, and the GIXD patterns were recorded on a 2D image detector (Pilatus 300K). The polymer thin films for GIXD were prepared under the same condition used for the solar cell fabrication. Dynamic force-mode atomic force microscopic images were obtained with Nanocute scanning probe microscope system (SII Nanotechnology, Inc.) by using a canti-lever, SI-DF20 (Seiko Instruments Inc.).

OFET fabrication and evaluation.

OFET devices were fabricated in a bottom-gate-top-contact configuration on a heavily doped n$^+$-Si(100) wafer with 200-nm-thickness thermally grown SiO$_2$ (C_i = 17.3 nFcm^{-2}). The Si/SiO$_2$ substrates were ultrasonicated with water for 3 min thrice, and acetone and isopropanol for 5 min, respectively, and rinsed in boiled isopropanol for 10 min, and then were subjected to UV-ozone treatment for 30 min. The cleaned substrates were then treated by 1H,1H,2H,2H-perfluorodecyltriethoxysilane (FDTS) as follows. The substrates were left in a Teflon container with several drops of FDTS and then the container was heated to 120 °C for 2h in the desiccator. The FDTS-treated substrates were ultrasonicated with acetone and isopropanol for 5 min, respectively, and rinsed in boiled isopropanol for 10 min. In a glove box under nitrogen atmosphere, polymer thin films were spin-coated from hot DCB (for PNTz4T and PNTz4TF2) or CB/TCB=1/1 (for PNTz4TF4) solutions (3 gL^{-1}) at 3000 rpm for 40 sec. The polymer films were annealed at 200 ºC for 30 min under nitrogen. On top of the polymer thin films, gold drain and source contact electrodes (thickness: 80 nm) with the channel length and width of 40 μm and 1500 μm, respectively, were deposited in vacuum through shadow masks. In PNTz4TF2 and PNTz4TF4, the devices were again annealed at 150 °C (for PNTz4TF2) or 200 °C (for PNTz4TF4) for 30 min after the deposition of the Au electrodes.

Current-voltage characteristics of the OFET devices were measured at room temperature under ambient conditions (relative humidity: 30~40%) with a Keithley 4200-SCS semiconductor parameter analyzer. Threshold voltages of the devices were estimated from the transfer plots by extrapolating the square root of the drain current to the horizontal axis. Hole field-effect mobilities were extracted from the square root of the drain current in the saturation regime (V_d = –60 V) by using the following equation,

$$I_d = (WC_i/2L) \, \mu \, (V_g\text{-}V_{th})^2$$

where, L and W are channel length and width, respectively, and C_i is capacitance of the gate insulator. The average hole mobilities and threshold voltages were obtained over more than 10 devices.

Solar cell fabrication and evaluation

ITO substrates were pre-cleaned sequentially by sonicating in a detergent bath, deionized water, acetone, and isopropanol at room temperature, and in a boiled isopropanol bath, each for 10 min. Then, the substrates were subjected to UV/ozone treatment at room temperature for 20 min. The pre-cleaned ITO substrates masked at the electrical contacts were coated with ZnO precursor by spin coating (5000 rpm for 30 s) a precursor solution prepared by dissolving zinc acetate dehydrate (549 mg) and ethanolamine (152 mg) in 5 mL of 2-methoxyethanol. They were then baked in air at 170 ºC for 30 min, rinsed with acetone, isopropanol and boiled isopropanol bath and dried in a glove box. The photoactive layers were deposited in a glove box (KOREA KIYON, KK-011AS-EXTRA) by spin coating DCB solution for PNTz4TF2 and CB/TCB=1/1 mixture solution for PNTz4TF4: the containing 4-5 g/L of the polymer sample with respective amount of $PC_{71}BM$ was kept at 160 °C for 30 min, and the hot solution was directly spin-coated on the substrate, which was pre-heated at 160°C, at 600 rpm for 20 sec. The thin films were transferred into a vacuum evaporator (ALS Technology, E-100J) connected to the glove box. MoO_x (7.5 nm) and Ag (100 nm) were deposited sequentially by thermal evaporation under ~10^{-5} Pa, where the active area of the cells was 0.16 cm^2. J–V characteristics of the cells were measured with a Keithley 2400 source measure unit in nitrogen atmosphere under 1 Sun (AM1.5G) conditions using a solar simulator (SAN-EI Electric, XES-40S1). The light intensity for the J–V measurements was calibrated with a reference PV cell (Konica Minolta AK-100 certified by the National Institute of Advanced Industrial Science and Technology, Japan). EQE spectra were measured with a Spectral Response Measuring System (Soma Optics, Ltd., S-9241). The thickness of the active layer was measured with an AlphaStep® D-100 surface profiler (KLA Tencor).

Hole-only and electron-only device fabrication and measurement

For hole-only devices, the pre-cleaned ITO substrates were coated with PEDOT:PSS by spin-coating (5,000 r.p.m. for 30 s, thickness of ~30 nm). The polymer neat film or the polymer/$PC_{71}BM$ (1:2 weight

ratio) blend film was then spin-coated from DCB solution for PNTz4TF2 and CB/TCB=1/1 mixture solution for PNTz4TF4: the containing 4–5 g/L of the polymer sample with respective amount of PC$_{71}$BM was kept at 160 °C for 30 min, and the hot solution was directly spin-coated on the substrate, which was pre-heated at 160°C, at 600 rpm for 20 sec. The thin films were transferred into a vacuum evaporator connected to the glove box, and MoO$_x$ (7.5 nm) and Ag (100 nm) were deposited sequentially through a shadow mask. For electron-only devices, the pre-cleaned ITO substrates were coated with ZnO and then with the polymer/ PC$_{71}$BM (1:2 weight ratio) blend film as described above. LiF (2 nm) and Al (100 nm) were deposited sequentially. The J–V characteristics were measured in the range of 0−7 V using a Keithley 2400 source measure unit under nitrogen in the dark, and the mobility was calculated by fitting the J–V curves to a space charge limited current model described by

$$J = (8/9)\, \varepsilon_r\, \varepsilon_0\, \mu\, (V^2/L^3)$$

where ε_r is the dielectric constant of the polymer, ε_0 is the permittivity of free space, μ is the mobility, $V = V_{appl} - V_{bi}$, where V_{appl} is the applied voltage to the device and V_{bi} is the built-in voltage due to the difference in workfunction of the two electrodes (determined to be 0.1 for the hole-only device and 0.1 for the electron-only device), and L is the polymer thickness. The dielectric constant ε_r is assumed to be 3, which is a typical value for semiconducting polymers.

3-5. References

1) Mataka, S.; Takahashi, K.; Ikezaki, Y.; Hatta, T.; Tori-i, A; Tashiro, M. *Bull. Chem. Soc. Jpn.* **1991,** *64*, 68–73.

2) Wang, M.; Hu, X.; Liu, P.; Li, W.; Gong, X.; Huang, F.; Cao, Y. *J. Am. Chem. Soc.* **2011**, *133*, 9638–9641.

3) Osaka, I.; Kakara, T.; Takemura, N.; Koganezawa, T.; Takimiya, K. *J. Am. Chem. Soc.* **2013**, *135*, 8834–8837.

4) Saito, M.; Osaka, I.; Suzuki, Y.; Takimiya, K.; Okabe, T.; Ikeda, S.; Asano, T. *Sci. Rep.* **2015**, 5,

14202.

5) Osaka, I.; Shimawaki, M.; Mori, H.; Doi, I.; Miyazaki, E.; Koganezawa, T.; Takimiya, K. *J. Am. Chem. Soc.* **2012**, *134*, 3498–3507.

6) Kawashima, K.; Miyazaki, E.; Shimawaki, M.; Inoue, Y.; Mori, H.; Takemura, N.; Osaka, I.; Takimiya, K. *Polym. Chem.* **2013**, *4*, 5224–5227.

7) Vohra, V.; Kawashima, K.; Kakara, T.; Koganezawa, T.; Osaka, I.; Takimiya, K.; Murata, H. *Nat. Photon.* **2015**, *9*, 403–408.

8) Zhou, H.; Yang, L.; Stuart, A. C.; Prince, S. C.; Liu, S.; You, W. *Angew. Chem. Int. Ed.* **2011**, *50*, 2995–2998.

9) Albrecht, S.; Janietz, S.; Schindler, W.; Frisch, J.; Kurpiers, J.; Kniepert, J.; Inal, S.; Pingel, P.; Fostiropoulos, K.; Koch, N.; Neher, D. *J. Am. Chem. Soc.* **2012**, *134*, 14932–14944.

10) Stuart, A. C.; Tumbleston, J. R.; Zhou, H.; Li, W.; Liu, S.; Ade, H.; You, W. *J. Am. Chem. Soc.* **2013**, *135*, 1806−1815.

11) Jo, J. W.; Jung, J. W.; Wang, H.-W.; Kim, P.; Russell, T. P.; Jo, W. H. *Chem. Mater.* **2014**, *26*, 4214−4220.

12) Zhang, M.; Guo, X.; Zhang, S.; Hou, J. *Adv. Mater.* **2014**, 26, 1118–1123.

13) Albrecht, S.; Tumbleston, J. R.; Janietz, S.; Dumsch, I.; Allard, S.; Scherf, U.; Ade, H.; Neher, D. *J. Phys. Chem. Lett.* **2014**, *5*, 1131–1138.

14) Jo, J. W.; Bae, S.; Liu, F.; Russell, T. P.; Jo, W. H. *Adv. Funct. Mater.* **2015**, *25*, 120–125.

15) Gao, Y.; Zhang, X.; Tian, H.; Zhang, J.; Yan, D.; Geng, Y.; Wang, F. *Adv. Mater.* **2015**, *27*, 6753–6759.

16) Meyer, F. *Prog. Polym. Sci.* **2015**, *47*, 70–91.

17) Liu, Y.; Zhao, J.; Li, Z.; Mu, C.; Ma, W.; Hu, H., Jiang, K.; Lin, H.; Ade, H., Yan, H. *Nat. Commun.* **2014**, *5*, 5293.

18) Jo, J. W.; Jung, J. W.; Jung, E. H.; Ahn, H.; Shin, T. J.; Jo, W. H. *Energy Environ. Sci.* **2015**, *8*,

2427–2434.

19) Sakamoto, Y.; Komatsu, S.; Suzuki, T. *J. Am. Chem. Soc.* **2001**, *123*, 4643–4644.

20) Matthews, J. R.; Niu, W.; Tandia, A.; Wallace, A. L.; Hu, J.; Lee, W.-Y.; Giri, G.; Mannsfeld, S. C. B.; Xie, Y.; Cai, S.; Fong, H. H.; Bao, Z.; He, M. *Chem. Mater.* **2013**, *25*, 782–789.

21) Kawabata, K.; Osaka, I.; Nakano, M.; Takemura, N.; Koganezawa, T.; Takimiya, K. *Adv. Electron. Mater.* **2015,** *DOI: 10.1002/aelm.201500039.*

22) Yoshida, H. *Chem. Phys. Lett.* **2012**, *539–540*, 180–185.

23) Yoshida, H. *Anal. Bioanal. Chem.* **2014**, *406*, 2231–2237.

24) Kobayashi, S.; Nishikawa, T.; Takenobu, T.; Mori, S.; Shimoda, T.; Mitani, T.; Shimotani, H.; Yoshimoto, N.; Ogawa, S.; Iwasa, Y. *Nat. Mater.* **2004**, *3*, 317−322.

25) Nakayama, K.; Uno, M.; Nishikawa, T.; Nakazawa, Y.; Takeya, *J. Org. Electron.* **2010**, 11, 1620−1623.

26) Kawashima, K.; Osaka, I.; Takimiya, K. *Chem. Mater.* **2015**, *27*, 6558−6570.

27) Uemura, T.; Rolin, C.; Ke, T.-H.; Fesenko, P.; Genoe, J.; Heremans, P.; Takaya, *J. Adv. Mater.* **2016**, *28*, 151−155.

28) He, Z.; Zhong, C.; Huang, X.; Wong, W.-Y.; Wu, H.; Chen, L.; Su, S.; Cao, Y. *Adv. Mater.* **2011**, *23*, 4636–4643.

29) Guo, X.; Zhou, N.; Lou, S. J.; Smith, J.; Tice, D. B.; Hennek, J. W.; Ortiz, R. P.; Navarrete, J. T. L.; Li, S.; Strzalka, J.; Chen, L. X.; Chang, R. P. H.; Facchetti, A.; Marks, T. J. *Nat. Photon.* **2013**, *7*, 825–833.

30) Melzer, C.; Koop, E.; Mihailetchi, V. D.; Blom, P. W. M. *Adv. Funct. Mater.* **2004**, *14*, 865–870.

31) Rivnay, J.; Mannsfeld, S. C. B.; Miller, C. E.; Salleo, A.; Toney, M. F. *Chem. Rev.* **2012**, *112*, 5488–5519.

32) Osaka, I.; Takimiya, K. *Polymer* **2015**, *59*, A1–A15.

33) DeLongchamp, D. M.; Kline, R. J.; Jung, Y.; Lin, E. K.; Fischer, D. A.; Gundlach, D. J.; Cotts, S.

K.; Moad, A. J.; Richter, L. J.; Toney, M. F.; Heeney, M.; McCulloch, I. *Macromolecules* **2008**, *41*, 5709–5715.

34) Rogers, J. T.; Schmidt, K.; Toney, M. F.; Kramer, E. J.; Bazan, G. C. *Adv. Mater.* **2011**, *23*, 2284–2288.

35) Guo, X.; Puniredd, R.; Baumgarten, M.; Pisula, W.; Müllen, K. *J. Am. Chem. Soc.* **2012**, *134*, 8404–8407.

Chapter 4
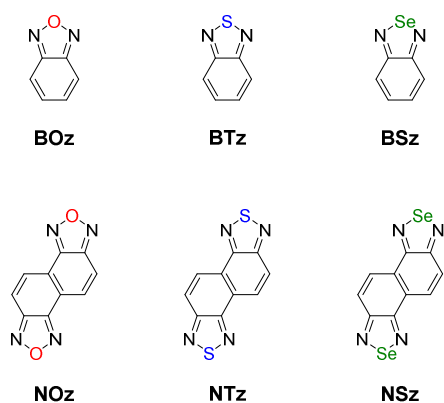
Naphthobischalcogenadiazole-based polymers (PNXz4T)

4-1. Introduction

2,1,3-Benzothiadiazole (BTz) is one of the most widely used heteroaromatic rings for semiconducting polymers (Figure 4-1).[1] Due to the high electron deficiency, BTz acts as an acceptor unit for so-called donor–acceptor (D–A) polymers, and largely deepens the energy levels of the polymers. The oxygen and selenium analogues of BTz, *i.e.*, 2,1,3-benzoxadiazole (BOz)[2] and 2,1,3-benzoselenadiazole (BSz)[3] (Figure 4-1), have also been used as an acceptor unit for D–A polymers. It has been reported that although the crystallinity of the resulting polymers were similar, the replacement of BTz by BOz or BSz altered the electronic structure. Whereas the replacement of BTz by BOz further deepened the energy levels of the polymers, replacement by BSz shallowed the energy levels.

Naphtho[1,2-*c*:5,6-*c'*]bis[1,2,5]thiadiazole (NTz, Figure 4-1) is a tetracyclic heteroaromatic where two BTz rings are fused. With its high planarity and high electron deficiency,[4] NTz is a fascinating acceptor unit for D–A polymers.[5-10] Independently from other groups, I have been focusing on NTz-based polymers.[5, 7, 8, 11] I revealed that the NTz-based polymers form high crystalline structures and exhibit high hole mobilities of around 0.5 cm^2 V^{-1} s^{-1} in OFETs.[5] NTz polymers also showed quite high power conversion efficiencies when used as the p-type material for the bulk heterojunction solar cells.[5, 7, 8, 12] These results indicated that NTz is promising building unit for D–A polymers. Replacement of the sulfur atom of NTz by the oxygen and selenium atoms, resulting in naphtho[1,2-*c*:5,6-*c'*]bis[1,2,5]oxadiazole (NOz) and naphtho[1,2-*c*:5,6-*c'*]bis[1,2,5]selenadiazole (NSz) (Figure 4-1), is expected to alter the electronic structure of the corresponding polymers. As seen from the computation of model compounds, where benzochalcogenadiazoles (BXz) and naphthobischalcogenadiazoles (NXz) are sandwiched with methylthiophenes, the effect of the chalcogen atom seems to be even larger than in the case of BXz (Figure 4-2). In particular NOz is expected to bring the corresponding polymers quite deep LUMO energy levels as well as deep HOMO energy levels, which is important in terms of providing n-channel (or ambipolar)

71

behavior in OFETs and high open-circuit voltage (V_{OC}) in OPVs. In fact, during the course of our study, Zhang and co-workers reported on an NOz-based D−A semiconducting polymer incorporating a ladder-type heptacyclic arene as the donor unit, which can deepen both the HOMO and LUMO energy levels compared with NTz and exhibits power conversion efficiencies of ~8.4% with high V_{OC} of ~0.9 V in OPV devices.[13]

Herein, I synthesize NOz and NSz, and the new polymers based on these building units. The chemical structure of the polymers used here is composed of quaterthiophene as the donor units and NXz as the acceptor units (PNOz4T, PNTz4T and PNSz4T, Figure 4-3). The use of the simple quaterthiophene unit allows us to better understand the nature of the NXz units. I describe the synthesis, characterization, and transistor and solar cell properties of PNOz4T and PNSz4T, in comparison with the NTz analogues. I first discuss the differences of optical and electrochemical properties and the molecular structures between the monomer units of PNXz4T (NXz2T-DT), or between the corresponding model compounds (NXz2T), respectively (Figure 4-2). I then focus on the physicochemical properties, charge carrier transport properties of the polymers evaluated by OFET devices, and ordering structures of the polymers in the thin film (section 4-2). Next, I discuss the OPV performances of the polymers (section 4-3).

Figure 4-1. Chemical structures of benzochalcogenadiazoles (BXz) and naphthobischalcogenadiazoles (NXz). BOz = 2,1,3-benzothiadiazole, BTz = 2,1,3-benzoxadiazole, BSz = 2,1,3-benzoselenadiazole, NOz = naphtho[1,2-*c*:5,6-*c'*]bis[1,2,5]oxadiazole, NTz = naphtho[1,2-*c*:5,6-*c'*]bis[1,2,5]thiadiazole, NSz = naphtho[1,2-*c*:5,6-*c'*]bis[1,2,5]selenadiazole.
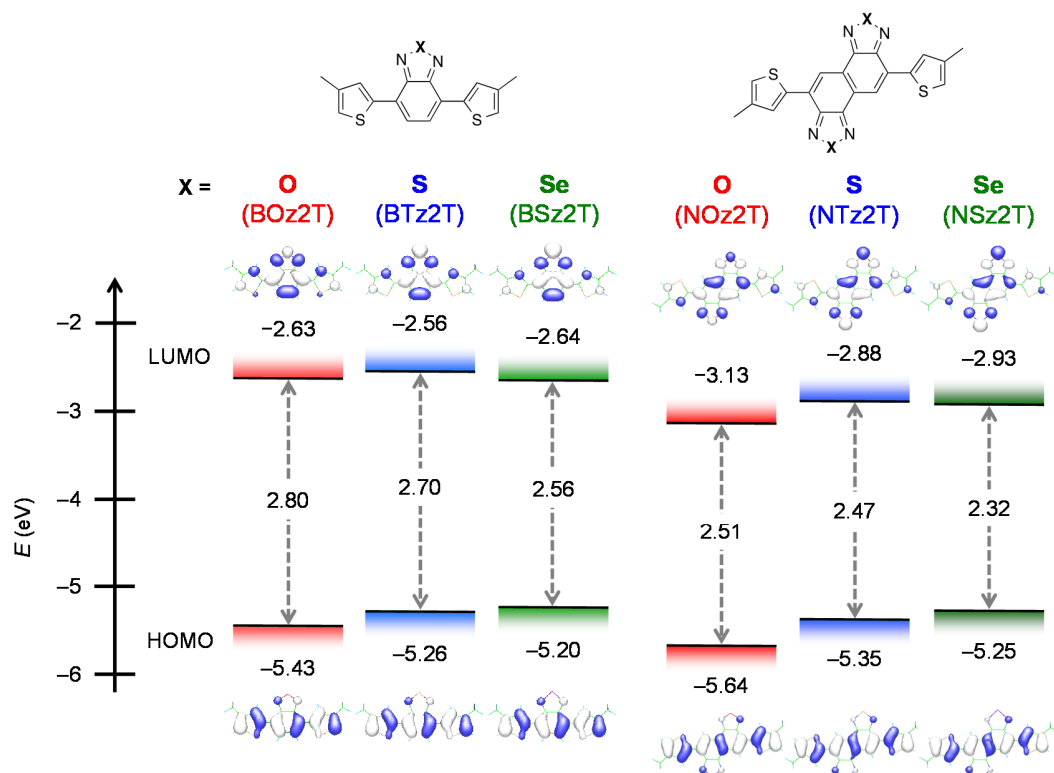
Figure 4-2. Calculated HOMOs and LUMOs of the model compounds for BXz (BOz2T, BTz2T, and BSz2T) and NXz (NOz2T, NTz2T, and NSz2T) using the DFT method at the B3LYP/6-31G(d) level.
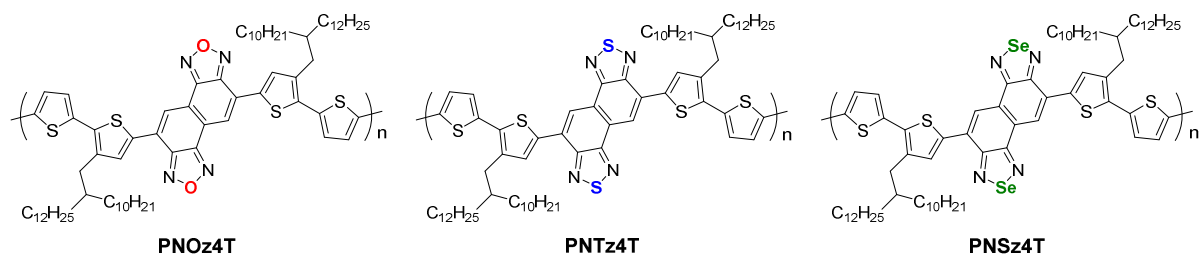
Figure 4-3. Chemical structures of the polymers based on NOz, NTz, and NSz studied in this work.

4-2. Effect of chalcogen atom on the properties of naphthobischalcogenadiazole-based π-conjugated polymers

4-2-1. Synthesis and Properties

Synthesis of NOz and NSz is shown in Scheme 4-1. NOz was synthesized as follows. An oxidation of 1,5-dinitro-2,6-diaminonaphtalene (**1**) by sodium hypochlorite and potassium hydroxide gave three

isomers of NOz *N*-oxides (**2a-c**), which were then reduced by hydroxylamine in the presence of potassium hydroxide, giving NOz in a 53% yield with two steps. For NSz, a reduction of **1** by Raney nickel gave 1,2,5,6-tetraaminonaphthalene[14] in a 70% yield, which was cyclized by using seleninyl chloride to afford NSz in a 68% yield.

Scheme 4-1. Synthesis of NOz and NSz. (TBAB = tetrabutylammonium bromide).
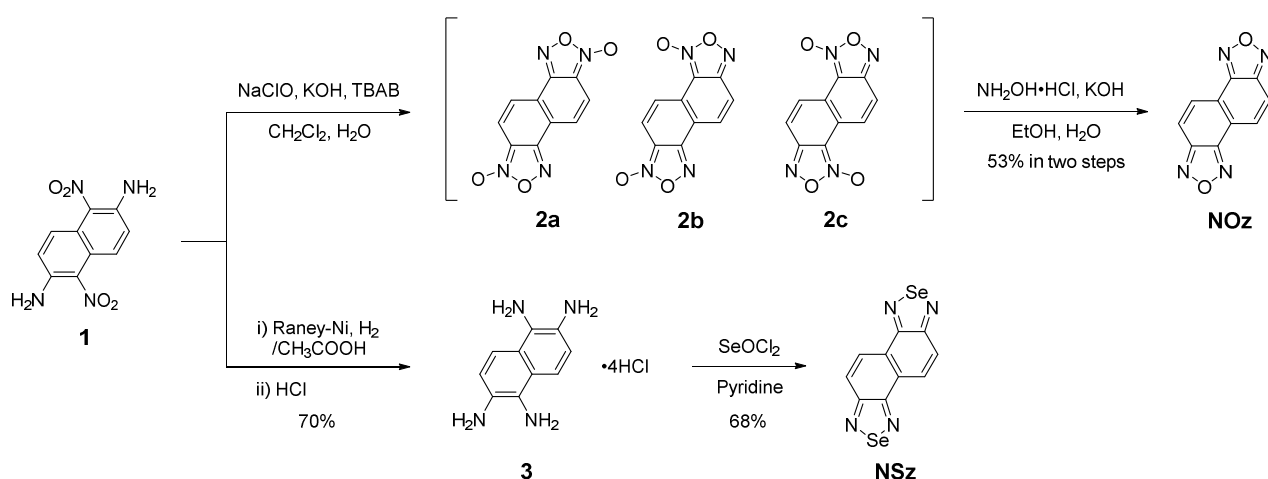
Synthesis of monomers and polymers is shown in Scheme 4-2. Both NOz and NSz were dibrominated at the 5,10 position to give **4** and **5**, respectively. These were cross-coupled with 4-(2-decyltetradecyl)-2-(trimethylstannyl)thiophene (**6**) via the Stille coupling reaction to afford NOz2T-DT (DT = 2-decyltetradecyl) and NSz2T-DT, which were then dibrominated with *N*-bromosuccinimide (NBS) to yield the corresponding monomers (**7** and **8**). The monomers were copolymerized with 5,5′-bis(trimethylstannyl)-2,2′-bithiophene (**9**) via the Stille coupling reaction associated with microwave to give PNOz4T and PNSz4T, respectively. While PNOz4T was synthesized at 140 °C, PNSz4T was synthesized at 180 °C. The lower polymerization temperature for PNOz4T is to avoid "over-polymerization". In fact, when PNOz4T was synthesized at 180 °C, more than 80 wt% of the resulted polymer sample was insoluble. Both PNOz4T and PNSz4T synthesized at 140 °C and 180 °C, respectively, were soluble in hot chlorobenzene (CB) and *o*-dichlorobenzene (DCB). Although it is difficult to quantify the solubility, both polymers had less solubility than PNTz4T.

Scheme 4-2. Synthesis of the monomers and polymers.
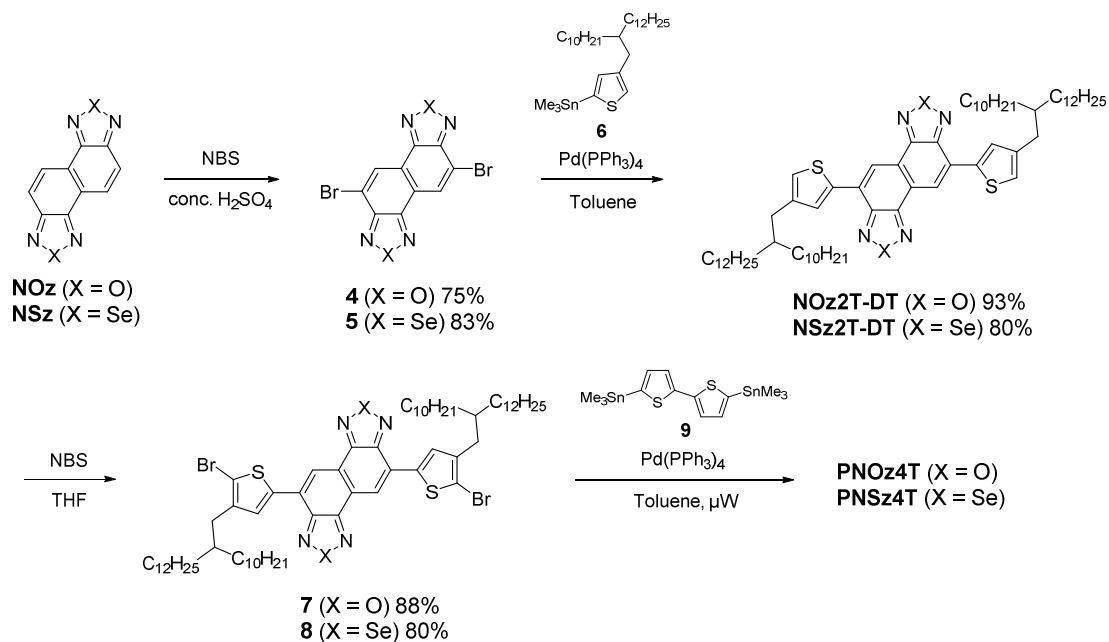
The number average molecular weight (M_n) and weight average molecular weight (M_w) were evaluated by high-temperature gel-permeation chromatography (GPC) using DCB (140 °C) as the eluent. M_n and M_w were 49.7 kDa and 240.8 kDa with the polydispersity index (PDI) of 4.8, and 28.7 kDa and 60.6 kDa with PDI of 2.1 for PNOz4T and PNSz4T, respectively (Table 4-1). As the comparison, PNTz4T was also synthesized by the reported procedure, where the polymerization was carried out at 180 °C (M_n = 52.9 kDa, M_w = 113.5 kDa, PDI = 2.1). It is noted that the chromatogram of PNOz4T exhibited bimodal distributions, resulting in a high PDI of 4.8. I assume that this is due to the strong aggregation, as sometimes seen in D–A semiconducting polymers.[15, 16] This implies that PNOz4T has stronger aggregation tendency than PNTz4T and PNSz4T.

Thermal properties of the polymers were evaluated by the differential scanning calorimetry (DSC) (Figure 4-4) and thermogravimetry (TG) (Figure 4-5). While the DSC curve of PNTz4T and PNSz4T showed a melting point (T_m) at 321 °C and 221 °C, respectively, in the heating process (302 °C and 120 °C in the cooling process), that of PNOz4T showed no transition peaks below 350 °C. The DSC results

suggest that rigidity or the backbone is in order of PNOz4T > PNTz4T > PNSz4T. The temperatures of 5% weight loss (T_{d5}) were 368 °C, 439, and 368 for PNOz4T, PNTz4T, and PNSz4T, respectively.

Table 4-1. Polymerization results and polymer properties.

Polymer	M_n (kDa)[a]	M_w (kDa)[a]	PDI[a]	DP_n[b]	T_m (°C)[c] heating/cooling	T_{d5} (°C)[d]
PNOz4T	49.7	240.8	4.8	41.0	–	368
PNTz4T	52.9	113.5	2.1	42.5	321/302	439
PNSz4T	28.7	60.6	2.1	21.5	221/120	368

[a]Determined by GPC using polystyrene standard and DCB as the eluent at 140 °C. [b]Based on the repeating unit. [c]Melting point determined by DSC measurements at a scan rate of 10 °C/min. [d]Temperature of 5% weight loss.
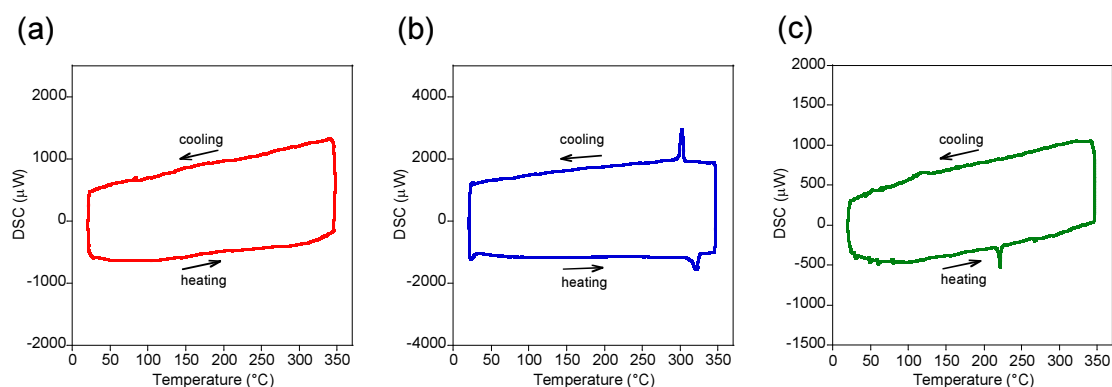
Figure 4-4. DSC curves of the polymers. (a) PNOz4T, (b) PNTz4T, (c) PNSz4T.
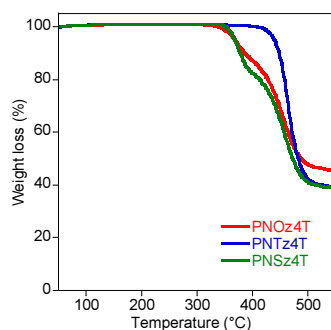
Figure 4-5. TGA curves of the polymers.

4-2-2. Properties and structures of the monomers.

I evaluated the electrochemical and optical properties of the NXz-based compounds, *i.e.*, NOz2T-DT, NTz2T-DT and NSz2T-DT, by using cyclic voltammetry, UV-vis absorption and photoluminescence (PL) spectroscopies. Figure 4-6a shows the cyclic voltammograms of the monomers and the corresponding parameters are summarized in Table 4-2. Whereas the oxidation onset of NOz2T-DT (1.40 V) was higher than that of NTz2T-DT (1.18 V), that of NSz2T-DT (1.09 V) was lower. These onset potentials for NOz2T-DT, NTz2T-DT, and NSz2T-DT correspond to the HOMO energy levels (E_H^{CV}) of –5.76 eV, –5.54 eV, and –5.45 eV, respectively (Table 4-2, Figure 4-8). The reduction onset was higher for both NOz2T-DT (–0.78 V) and NSz2T-DT (–0.98 V) than for NTz2T-DT (–1.08 V). Accordingly, the LUMO energy levels (E_L^{CV}) were –3.58 eV, –3.28 eV, and –3.38 eV for NOz2T-DT, NTz2T-DT, and NSz2T-DT, respectively (Table 4-2, Figure 4-8). These E_H^{CV}s and E_L^{CV}s were in good agreement with the computation by the DFT method at the B3LYP/6-31g(d) level (Table 4-2), in which NOz2T, NTz2T, and NSz2T with the methyl group were used instead of the DT group to simplify the calculation. The computation also revealed that whereas HOMOs are delocalized over the molecule, LUMOs are relatively localized on the NXz unit in all cases (Figure 4-2).
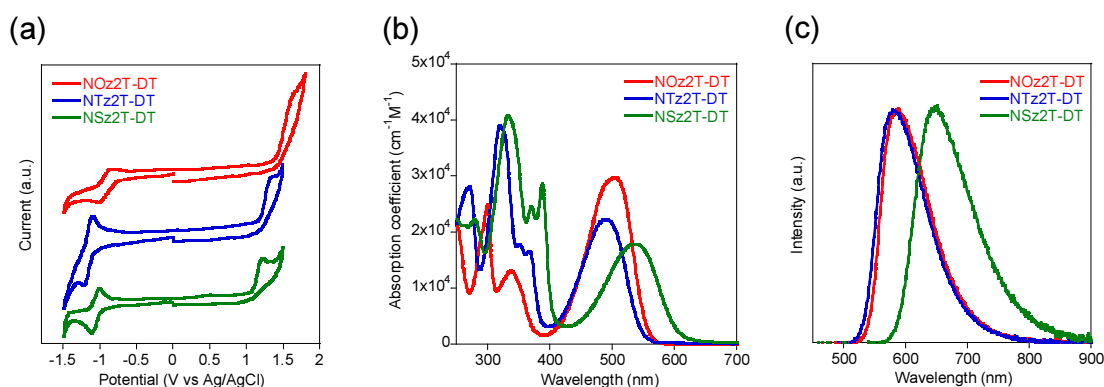
Figure 4-6. Cyclic voltammograms (a), UV–vis. absorption spectra (b), and photoluminescence spectra (c) of NOz2T-DT, NTz2T-DT, and NSz2T-DT in the solution. The cyclic voltammetry were carried out in dichloromethane, and the absorption and photoluminescence spectroscopies were carried out in chloroform.

It is noted that the order of E_H^{CV} of the present system follows the general trend observed in many chalcogenophene-fused aromatic systems, such as benzodichalcogenophenes, naphthodichalcogeno-phenes, and anthradichalcogenophenes, where it rises in the order of oxygen, sulfur, and selenium.[17, 18] On the other hand, E_L^{CV} does not follow the trend observed in the above chalcogenophene-fused aromatic systems, where it falls in the same order. In contrast, E_L^{CV} of NOz2T-DT was lower than that of NTz2T-DT, although E_L^{CV} of NSz2T-DT was accordingly lower than that of NTz2T-DT, as shown above. This could be explained by taking into account the difference in aromaticity of chalcogenadiazoles and electron negativity of chalcogens.[19] Judging from the reported nucleus-independent chemical shifts (NICS) of 1,2,5-oxadiazole (–11.11 ppm, NICS(0)), 1,2,5-thiadiazole (–13.63 ppm), and 1,2,5-selenadiazole (–12.48 ppm),[20] aromaticity of the oxadiazole ring is markedly smaller than those of the thia- and selena-diazole rings,[21] which implies that the local atomic effect of oxygen is pronounced. In other words, the higher electronegativity of oxygen (3.44) than sulfur (2.58) and selenium (2.55) should be a dominant factor for determining the energy level of the frontier orbitals, in particular, LUMO.

Table 4-2. Electrochemical properties and molecular orbital energy levels of the monomers and polymers.

Compounds	E_{ox} (V)[a]	E_{red} (V)[a]	E_H^{CV} (eV)[b]	E_L^{CV} (eV)[b]	E_H^{PESA} (eV)[c]	E_L^{opt} (eV)[d]	E_H^{DFT} (eV)[e]	E_L^{DFT} (eV)[e]
NOz2T-DT	1.40	–0.78	–5.76	–3.58	–	–	–5.64	–3.13
NTz2T-DT	1.18	–1.08	–5.54	–3.28	–	–	–5.35	–2.88
NSz2T-DT	1.09	–0.98	–5.45	–3.38	–	–	–5.25	–2.93
PNOz4T	1.13	–0.70	–5.48	–3.65	–5.50	–3.98	–	–
PNTz4T	0.79	–0.89	–5.14	–3.46	–5.15	–3.59	–	–
PNSz4T	0.87	–0.80	–5.22	–3.55	–5.25	–3.69	–	–

a) Onset oxidation (E_{ox}) and reduction (E_{red}) potentials observed in cyclic voltammograms. The monomers and polymers were measured in solution and film, respectively. b) HOMO (E_H^{CV}) and LUMO (E_L^{CV}) energy levels evaluated using E_{ox} and E_{red}, respectively. c) HOMO energy level (E_H^{PESA}) evaluated by photoelectron spectroscopy in air. d) LUMO energy level (E_L^{opt}) calculated by the addition of the optical band gap (E_g) to E_H^{PESA}. e) HOMO (E_H^{DFT}) and LUMO (E_L^{DFT}) energy levels calculated by the DFT method at the B3LYP/6-31g(d) level. Note that the DT group of the side chain was replaced with the methyl group.

UV-vis absorption and PL spectra of the compounds are displayed in Figures 4-6b and 4-6c, respectively, and the properties are summarized in Table 4-3. NOz2T-DT and NTz2T-DT showed similar spectra for both absorption and PL with the absorption maxima (λ_{max}) at around 500 nm and for emission maxima (PL_{max}) at around 580 nm. In contrast, NSz2T-DT showed a bathochromic shift for both the absorption and PL spectra by roughly 50 nm compared with NOz2T-DT and NTz2T-DT. The difference is mostly consistent with the computation. To better understand the fact that NOz2T-DT and NTz2T-DT provide similar absorption spectra and NSz2T-DT provides slightly bathochromically shifted absorption spectrum, TD-DFT calculations were carried out to simulate the electronic transition using NOz2T, NTz2T, and NSz2T (Figure 4-7). For all the compounds, the absorption bands mainly contributed by the HOMO–LUMO transition and appear in the visible region with λ_{max} of 547, 575, and 626 nm for NOz2T, NTz2T, and NSz2T, respectively. These values are somewhat larger than the experimental values. This is probably due to the overestimation of the coplanarity of the compounds in the calculations. The actual molecules have various molecular motions including rotation around the aromatic rings in solution at rt, which may reduce the orbital overlap between the adjacent rings. It is also noted that the difference between experimental and theoretical λ_{max}s become larger with the heavier chalcogen atoms, implying that the ring-size expansion with the heavier chalocogen atom can reduce the coplanarity, as will be discussed below, giving rise to the reduction of the π-electron delocalization in the actual molecules.

A higher PL quantum yield was observed for the oxygen analogue, NOz2T-DT, as similar to the other π-systems.[17, 18] Whereas in the chloroform solution, the quantum yields of NOz2T-DT and NTz2T-DT were similar with 95% and 97%, respectively, in powder, that of NOz2T-DT was 30% which is about three times higher than that of NTz2T-DT (12%). The quantum yield of selenium analogue, NSz2T-DT, was much lower in both solution (52%) and powder ($\approx$ 0%), most likely due to the heavy atom effect.

Table 4-3. Optical properties of the monomer and polymers.

Compounds	λ_{max} (nm)[a]		λ_{edge} (nm)[b]		E_g (eV)[c]		PL_{max} (nm)[d]		Φ_{PL} (%)[e]	
	solution	film	solution	film	solution	film	solution	solid	solution	solid
NOz2T-DT	504	–	557	–	2.23	–	585	648	95	30
NTz2T-DT	490	–	547	–	2.27	–	579	643	97	12
NSz2T-DT	538	–	606	–	2.05	–	648	–	52	<1
PNOz4T	749, 685	749, 680	798	815	1.55	1.52	–	–	–	–
PNTz4T	717, 660sh	721, 658	784	793	1.58	1.56	–	–	–	–
PNSz4T	686	706	796	792	1.56	1.56	–	–	–	–

a) absorption maximum, b) absorption onset, c) optical band gap calculated by using λ_{edge}, d) emission maximum, e) photoluminescence quantum yield.
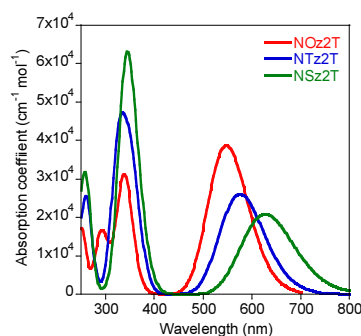
Figure 4-7. TD-DFT-estimated absorption spectra of NOz2T, NTz2T, and NSz2T.
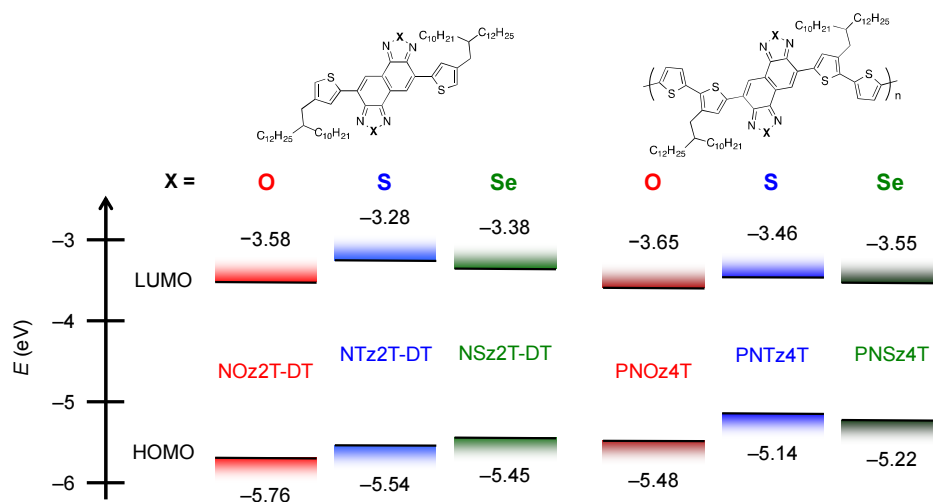
Figure 4-8. HOMO and LUMO energy levels of the monomers and polymers evaluated by cyclic voltammetry.

I also investigated in depth the molecular structure of NOz2T, NTz2T,[7] and NSz2T by means of single crystal X-ray analysis. Note that these molecules have the methyl groups instead of the DT groups on the flanking thiophene rings. As depicted in Figure 4-9, the molecules were almost coplanar in all cases. It is also noted that the sulfur atom of the thiophene ring points to the benzene substructure of NXz, resulting in the *anti* arrangement of the thiophene rings. Inspection of bond lengths in the compounds indicates that they have basically similar bond length alternation, representing the formal naphtho[1,2-*c*:5,6-*c*′]bis[1,2,5]chalcogenadiazole structure. Subtle but potentially important differences in the molecular structure are the N–X distance in the chalcogenadiazole substructure. As the chalcogen atom becomes heavier from oxygen to sulfur and selenium, the N–X distance increases from 1.38 Å (NOz2T) to 1.61 Å (NTz2T) and 1.79 Å (NSz2T). This increase apparently pushes out the nitrogen atom out of the chalcogenadiazole substructure toward the adjacent thiophene ring, which is evident by the fact that θ becomes smaller from 129.3° to 125.2°, as it goes from NOz2T to NSz2T. This suggests that the steric repulsion between the NXz core and the thiophene rings becomes larger as the chalcogen atom becomes heavier, although all the molecules remain coplanar in the single crystal: it is often the case and well-known that the molecular structure is largely affected by the packing motif in the single crystal, which can overcome the local steric repulsion. In parallel, α is smaller in NTz2T and NSz2T than in NOz2T. This implies that the thiophene ring slightly bends toward the benzene substructure, which suggests that NTz and NSz can cause more steric repulsion than NOz. In addition, the computation by the density functional theory (DFT) method predicted that the energy barrier of the rotation around the NOz core and flanking thiophene rings is largest among the NXz2T (Figure 4-10), indicating that NOz2T is energetically favorable to take the coplanar structure than others. With these structural features in the single crystal and computation, overall steric repulsion likely increases in the order of NOz2T < NTz2T < NSz2T. Thus, it is speculated that with the addition of the effect of the bulky side chains NXz2T-DT can lose the coplanarity as the chalcogen atom becomes heavier in the solution, which can rationalize the trend in the difference between the experimental and theoretical λ_{max}s as discussed above.
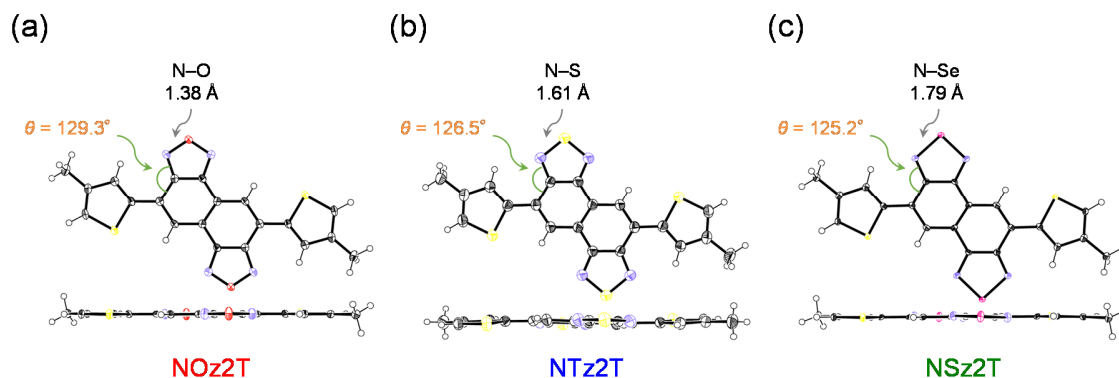
Figure 4-9. Molecular structures of NOz2T, NTz2T, and NSz2T determined by the single crystal X-ray structural analysis.
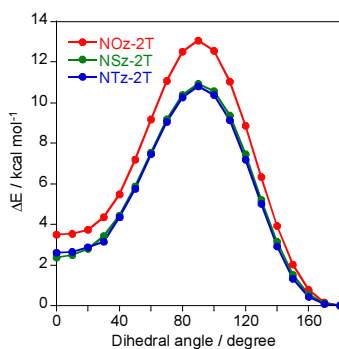
Figure 4-10. Energy variations of NXz2T with the rotation angle between the NXz core and the thiophene ring determined by the DFT method at the B3LYP/6-31d (g) level.

4-2-3. Physicochemical Properties of the polymers

E_H^{CV}s and E_L^{CV}s of the polymers were evaluated using the thin films. Figure 4-11a depicts the cyclic voltammograms of the polymer thin films, in which all polymers showed clear oxidation and reduction signals. The onset oxidation and reduction potentials and E_H^{CV} and E_L^{CV} calculated from these potentials are summarized in Table 4-2. E_H^{CV}s of PNOz4T and PNSz4T was –5.48 eV and –5.22 eV, respectively, both of which were deeper than that of PNTz4T (–5.14 eV) by 0.34 eV and 0.08 eV (Table 4-2, Figure 4-8). E_L^{CV}s of PNOz4T and PNSz4T were –3.65 eV and –3.55 eV, respectively, which were deeper by 0.19 eV and 0.09 eV than that of PNTz4T (–3.46 eV) (Table 4-2, Figure 4-8). It is noted that whereas the trend of E_L^{CV} in the polymers was similar to that in NXz2T-DTs, the trend of E_H^{CV} in the polymers was different

from that in NXz2T-DT. Whereas E_H^{CV} of NSz2T-DT was shallower than that of NTz2T-DT, E_H^{CV} of PNSz4T was deeper than that of PNTz4T. A plausible explanation is that the large steric repulsion between NXz and the adjacent thiophene rings in the NSz2T-DT moiety compared with the NTz2T-DT moiety, as discussed above, can lead to further large defect of the backbone in the polymer system and thereby the packing structure of PNSz4T compared with PNTz4T. This may result in the reduction of the effective π-conjugation and wider bandgap, which in turn gives rise to the deeper E_H^{CV} in PNSz4T than in PNTz4T. This explanation is consistent with the fact that λ_{max} of PNSz4T was slightly hypsochromically shifted compared to that of PNTz4T as shown below. Photoelectron spectroscopy in air (PESA) was also carried out using the polymer thin films to evaluate the HOMO energy levels (E_H^{PESA}) of the polymers (Figure 4-11b). E_H^{PESA} of PNOz4T, PNTz4T, and PNSz4T were –5.50 eV, –5.15 eV, and –5.25 eV, respectively, which were mostly similar to E_H^{CV}. LUMO energy levels (E_L^{opt}) were calculated by the addition of optical band gap (E_g) to E_H^{PESA}, which were –3.98 eV, –3.59 eV, and –3.69 eV for PNOz4T, PNTz4T, and PNSz4T, respectively. The difference between E_L^{CV} and E_L^{opt} can be ascribed to the exciton binding energy.[22]

    UV-vis absorption spectra of the polymers in thin film and in CB solution are shown in Figures 4-11c and 4-12, respectively. In the thin film, PNOz4T gave λ_{max} at 749 nm, which was bathochromically shifted by ca. 30 nm compared with PNTz4T (λ_{max} = 721 nm). E_g of PNOz4T was calculated to be 1.52 eV from the absorption edge (λ_{edge} = 815 nm), which was slightly narrower than that of PNTz4T (E_g = 1.56 eV, λ_{edge} = 793 nm). λ_{max} of PNSz4T (706 nm) was hypsochromically shifted by 15 nm compared with that of PNTz4T, although λ_{edge} (793 nm) and E_g (1.56 eV) was similar due to the blunt absorption signal. It is noted that while the bathochromic shift of PNOz4T against PNTz4T is consistent with that observed in NXz2T, the hypsochromic shift of PNSz4T against PNTz4T does not follow the trend in NXz2T-DT. I speculate that the larger steric repulsion in the NSz2T-DT moiety than in the NTz2T-DT moiety may give rise to a further large defect of the backbone structure in PNSz4T than in PNTz4T, which in turn gives rise to the reduction of the effective π-conjugation. In the solution, all the polymers exhibited mostly

identical spectrum to that in the film, implying the partial aggregation. The absorption coefficient of the absorption band at 500–800 nm was lower for the polymers with heavier chalcogen atoms. This is consistent with the trend observed in NXz2T-DT and the computation. The polymer solutions were heated up to 110 °C. In PNTz4T, the spectrum became structure-less upon heating, and λ_{max} showed large hypsochromic shift to 597 nm, suggesting the disaggregation as well as the destruction of coplanarity due to the molecular motion (Figure 4-12b). In PNOz4T, on the contrary, λ_{max} did not show a hypsochromic shift (Figure 4-12a). This is most likely due to the higher rigidity and thus the stronger intermolecular interaction of the PNOz4T backbone than PNTz4T, likely originating in the less steric repulsion in the NOz2T-DT moiety than the NTz2T-DT moiety, as described above. Furthermore, the large atom size in the heavier chalcogen can reduce the π–π interaction between the polymer backbones, which also contributes to the difference in the aggregation behavior seen in the solution absorption spectra. The spectrum of PNSz4T also became structure-less upon heating and hypsochromically shifted, but the shift of λ_{max} (λ_{max} = 633 nm at 110 °C) was smaller than that in PNTz4T (Figure 4-12c). The smaller hypsochromic shift is because λ_{max} of PNSz4T is already located at the slightly shorter wavelength region at rt than that of PNTz4T.
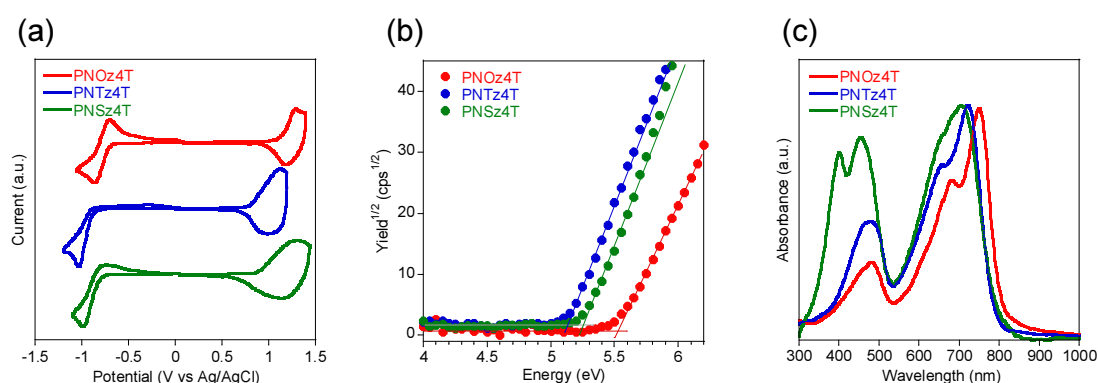
Figure 4-11. Cyclic voltammograms (a), Photoelectron spectra (b) and UV-vis. absorption spectra (c) of the polymers in thin films
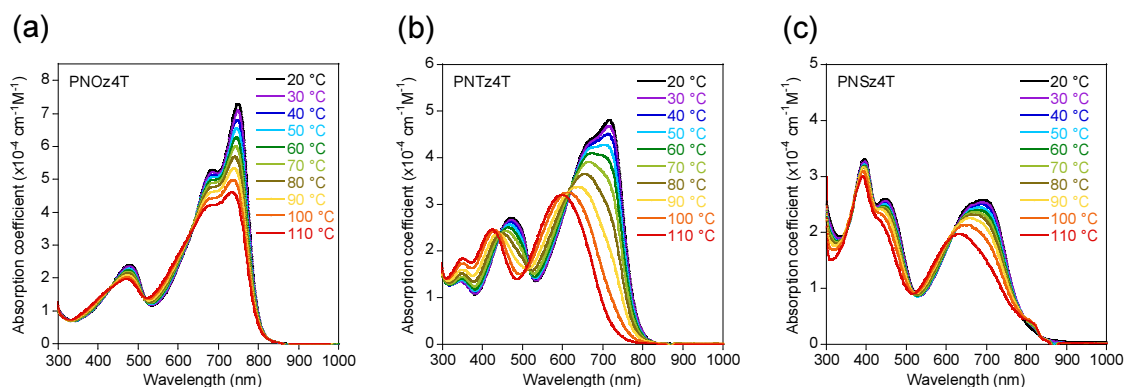
Figure 4-12. UV-vis. absorption spectra of the polymers in chlorobenzene. (a) PNOz4T, (b) PNTz4T, and (c) PNSz4T.

### 4-2-4. Thin film structure and morphology of the polymers

The grazing incidence wide-angle X-ray diffraction (GIXD) studies were carried out using the polymer thin films.[23] Figure 4-13a,b,c shows the two-dimensional (2D) GIXD patterns of the polymer thin films on the ODTS-treated Si/SiO$_2$ substrate. The 2D GIXD patterns of the polymers on the FDTS-treated substrate were almost the same as that on the ODTS-treated substrate (Figure 4-13d,e,f). In PNOz4T, diffractions assignable to the lamellar ($q_z \approx 0.28$ Å^{-1}) and the $\pi-\pi$ stacking structures ($q_{xy} \approx 1.8$ Å^{-1}) mainly appeared on the q_z and q_{xy} axes, respectively, indicating the predominant edge-on orientation on the substrate surface as similar to PNTz4T, though some fraction of face-on orientation also exist as the lamellar and $\pi-\pi$ stacking diffraction also but weakly appeared on the q_{xy} and q_z axes, respectively. The $\pi-\pi$ stacking distance (d_π) of PNOz4T was determined to be 3.5 Å, which was comparable to that of PNTz4T. Crystallinity of PNOz4T and PNTz4T was almost the same as the crystallite coherence length, calculated by the Scherrer equation using the full-width-at-half-maximum of the lamellar peak in the q_z axis and the $\pi-\pi$ stacking peak in the q_{xy} axis, showed similar values (Table 4-4).[24, 25] On the contrary, only a weak diffraction in the small-angle region was observed for PNSz4T, indicative of an amorphous nature. The significantly reduced crystallinity of PNSz4T is attributable to the larger steric repulsion in the NSz2T-DT moiety than in the oxygen and sulfur analogues, which may cause larger twist in the polymer backbone, as well as the larger atomic size of selenium, which could diminish the $\pi-\pi$ interaction

of the polymer backbones. This structural difference in the series of PNXz4T can be well-correlated with the electrochemical and optical properties.

Morphologies of the polymer thin films were investigated by using the atomic force microscopy (AFM). Figure 4-15 displays the topographic AFM images and the cross-sectional profiles of the polymer thin films on the ODTS-treated Si/SiO$_2$ substrate. Seemingly the PNOz4T film consists of larger domains compared with the PNTz4T and PNSz4T films, which would facilitate the charge carrier transport. This could explain the slightly higher mobility of PNOz4T than PNTz4T.
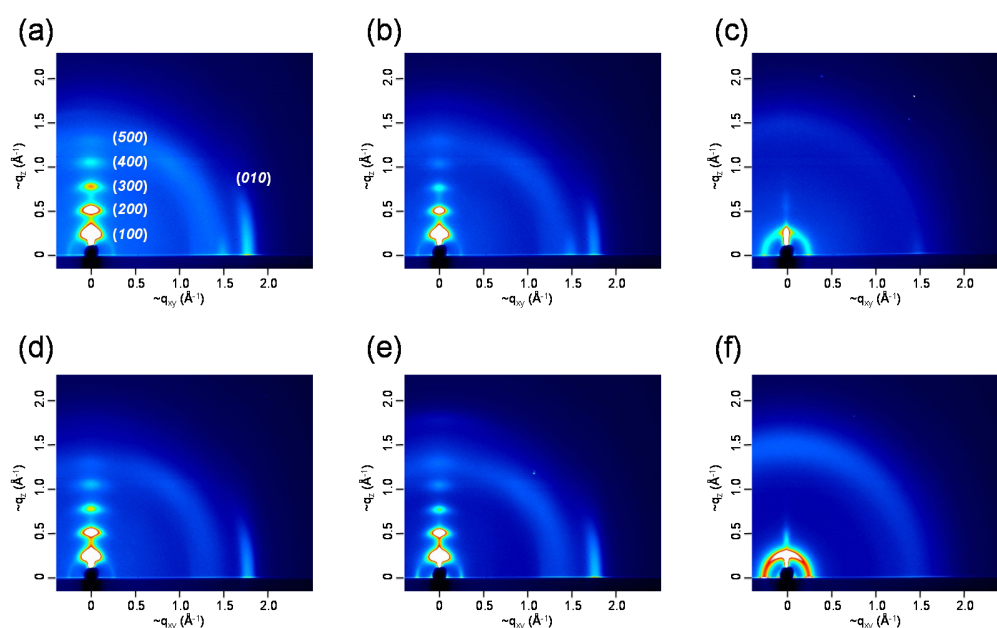
Figure 4-13. 2D GIXD images of the thin films on the ODTS (a-c) or FDTS (d-f)-treated Si/SiO$_2$ substrate for PNOz4T (a,d), PNTz4T (b,e), and PNSz4T (c,f)
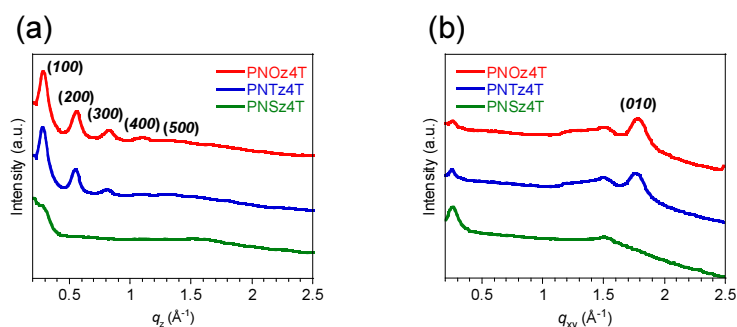

Figure 4-14. The cross-sectional profiles along the q_z (a) and q_{xy} (b) axes of the thin films on the ODTS-treated Si/SiO$_2$ substrate, respectively.

Table 4-4. Estimated crystallite coherence length of the polymers in the thin film.

Polymer	SAM	lamella ($\sim q_z$)		π–π (q_{xy})	
		FWHM (Å^{-1})[a]	L_C (nm)[b]	FWHM (Å^{-1})[a]	L_C (nm)[b]
PNOz4T	FDTS	0.041	15.3	0.13	4.8
	ODTS	0.043	14.6	0.13	4.8
PNTz4T	FDTS	0.036	17.4	0.13	4.8
	ODTS	0.041	15.3	0.14	4.5

(a) FWHM: full width at half maximum, (b) L_C: crystallite coherence length ($L_C = 2\pi/\text{FWHM}$)
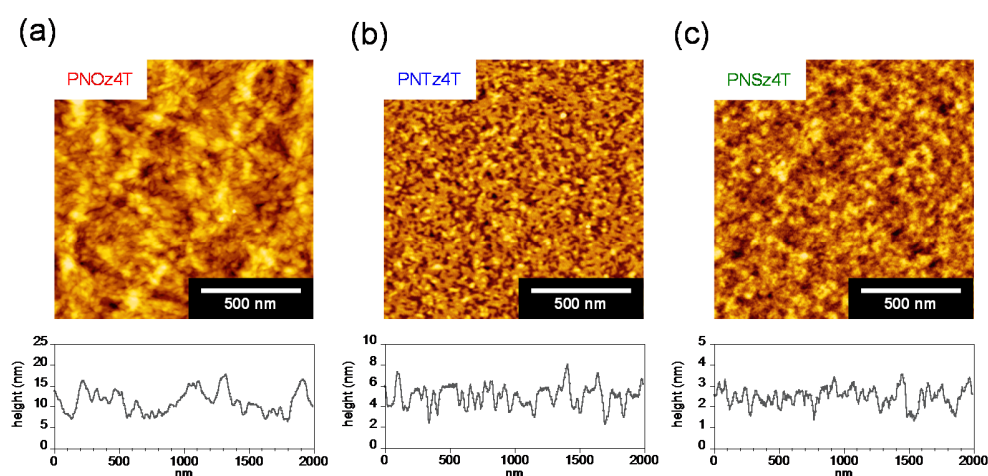
Figure 4-15. AFM height images (top) and cross section profiles (bottom) of the thin films on the actual device treated with ODTS for PNOz4T (a), PNTz4T (b), and PNSz4T (c).

4-2-5. Charge carrier transport property of the polymers

OFET devices were fabricated to investigate the charge carrier transport property of the polymers. The device used here has a bottom-gate-top-contact (BGTC) architecture using Si/SiO$_2$ as the substrate. The substrate surface was treated with surfactants such as 1*H*,1*H*,2*H*,2*H*-perfluorodecyltriethoxysilane (FDTS) or octadecyltriethoxysilane (ODTS), forming a self-assembled monolayer (SAM). Spin-coated polymer films were thermally annealed at 200 °C for 30 min, which refers to pre-annealing. After the deposition of the Au electrodes, the devices were again annealed at 200 °C, which refers to post-annealing. Figure 4-16 shows transfer (a,c,e,g,i,k) and output (b,d,f,h,j,l) curves of the polymer devices measured in air. The OFET characteristics are summarized in Table 4-5. All the polymers showed p-channel

characteristics in the FDTS-treated devices. The hole mobility (μ_h) of PNOz4T was as high as 1.0 cm^2/Vs with the average of 0.55 cm^2 V^{-1} s^{-1}, which were about twice as high as those of PNTz4T (maximum 0.56 cm^2 V^{-1} s^{-1}, average 0.23 cm^2 V^{-1} s^{-1}). In contrast, μ_h of PNSz4T was one order of magnitude lower than those of the others (maximum 0.040 cm^2 V^{-1} s^{-1}, average 0.026 cm^2 V^{-1} s^{-1}). Current on and off ratios (I_{on}/I_{off}) were fairly high (10^6–10^7). The difference of μ_h is quite in good agreement with the 2D GIXD results, where PNOz4T and PNTz4T form crystalline structures and PNSz4T forms an amorphous-like structure.

It is also important to note the effect of molecular weight on the device performance, in particular for PNOz4T and PNTz4T with higher mobilities among the series. I have tested the PNOz4T devices using two other batches with higher and lower molecular weights (higher one: M_n = 57.2 kDa, M_w = 416.8 kDa, and PDI = 7.3, lower one: M_n = 34.8 kDa, M_w = 152.1 kDa, and PDI = 4.4) (Figure 4-18, Table 4-6). While the higher molecular weight batch exhibited μ_h of ~0.84 cm^2 V^{-1} s^{-1} (average 0.52 cm^2 V^{-1} s^{-1}), the lower molecular weight batch exhibited ~0.56 cm^2 V^{-1} s^{-1} (average 0.34 cm^2 V^{-1} s^{-1}) (Figure 4-19, Table 4-7). Therefore, it could be mentioned that the molecular weight of the initial batch of PNOz4T (M_n = 49.7 kDa, M_w = 240.8 kDa, see Table 4-1) is sufficiently high (in the optimal M_n and M_w ranges) to maximize the transistor performance. In addition, M_w or PDI may not affect the device performance as long as M_n is in the optimal range (> ca. 50 kDa). In the case of PNTz4T, the molecular weight shown in Table 4-1 is also sufficiently high (Figure 4-18, Table 4-6). As the polymer became insoluble when the molecular weight was increased (synthesized by more harsh conditions), the PNSz4T sample shown here should be the highest level with sufficient solubility. With these additional results, although the molecular weights of the polymers are quite different, the performance of the polymers summarized in Figure 4-16 and Table 4-5 can be reasonably evaluated and compared.

In the ODTS-treated devices, it is interesting to note that whereas PNTz4T and PNSz4T showed p-channel characteristics with of 0.22 cm^2 V^{-1} s^{-1} and 0.059 cm^2 V^{-1} s^{-1}, respectively, PNOz4T showed ambipolar characteristics with well-balanced μ_h and electron mobilities (μ_e) of up to 0.45 cm^2 V^{-1} s^{-1} and

0.28 cm^2 V^{-1} s^{-1}, respectively. The observed ambipolar behavior of PNOz4T is ascribed to its deeper LUMO energy level. The difference in the charge carrier polarity between FDTS and ODTS-treated devices is probably due to the difference in the dipole between a perfluoroalkylsilane (FDTS) and an alkylsilane (ODTS).[26] A similar phenomenon was also seen in the thienothiophenedione-based polymers.[16]
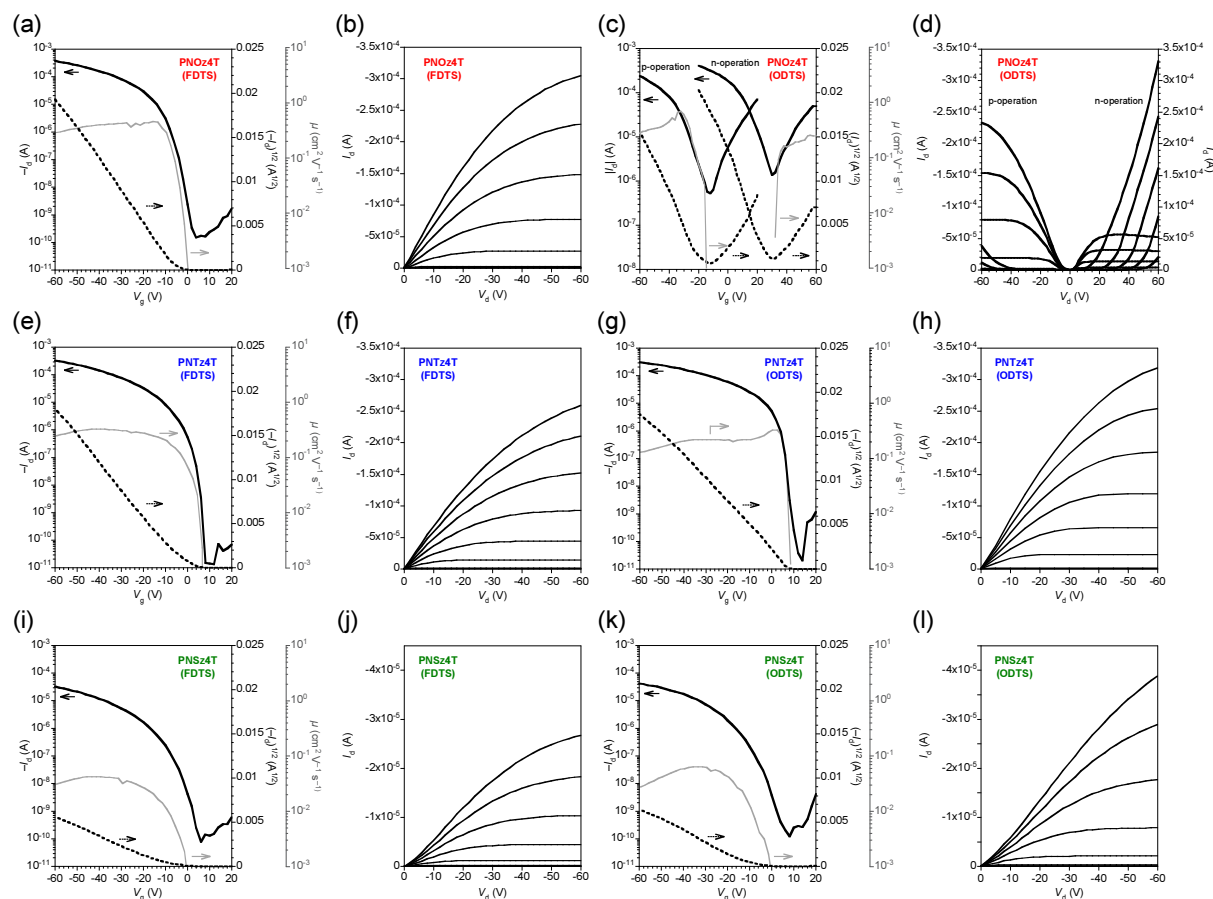
Figure 4-16. Current–voltage characteristics of OFET devices fabricated with PNOz4T (a–d), PNTz4T (e–h), and PNSz4T (i–l). (a, e, i) Transfer curves of OFET devices with the FDTS SAM. (b, f, j) Output curves of OFET devices with the FDTS SAM. (c, g, k) Transfer curves of OFET devices with the ODTS SAM. (d, h, l) Output curves of OFET devices with the ODTS SAM. The light-colored curves depicted with the transfer curves are the dependence of the mobility on the V_g; the hole mobility for p-operation and the electron mobility for n-operation in the case of PNOz4T with the ODTS SAM modified device.

In the transfer curves (Figures 4-16a, c, e, g, i, k) was also plotted the mobility as a function of the gate voltage (V_g). Whereas the mobilities were mostly independent of V_g above the threshold in the FDTS-

treated devices, they were dependent on V_g and were somewhat higher in the lower V_g region in the ODTS-treated devices. It is also noted that, in particular, FDTS-treated devices that use PNOz4T without post-annealing gave a kinked V_g–$(-I_d)^{1/2}$ plot in the transfer characteristics (Figure 4-17) with a larger threshold voltage in negative direction, resulting in the significantly V_g-dependent mobility and larger values. I speculate that, in the devices without post-annealing, the contact between the Au electrode and the polymer film might be poor, which causes too high charge accumulation and the charges would pour out at a higher V_g. The kink, however, disappeared by post-annealing, which is probably due to the improved contacts.
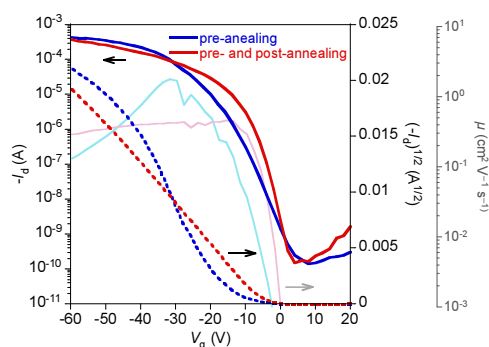
Figure 4-17. I_d vs. V_g curves (solid and dotted lines) and μ vs. V_g curves (light-colored lines) of OFET devices based on PNOz4T. Blue curves stand for the device with the pre-annealed (200 °C) film. Red curves stand for the device with the pre-annealed films annealing at 200 °C after the deposition of the source and drain Au electrodes.

Table 4-5. OFET characteristics of the polymers.

| Polymer	FDTS		ODTS			
	p-channel		p-channel		n-channel	
	μ_h (cm²/Vs)	I_{on}/I_{off}	μ_h (cm²/Vs)	I_{on}/I_{off}	μ_e (cm²/Vs)	I_{on}/I_{off}
PNOz4T	0.55 [0.22 ~ 1.0]	~10^7	0.27 [0.21 ~ 0.45]	~10^3	0.17 [0.10 ~ 0.28]	~10^2
PNTz4T	0.23 [0.18 ~ 0.56]	~10^7	0.15 [0.12 ~ 0.22]	~10^7	–	–
PNSz4T	0.026 [0.016 ~ 0.040]	~10^6	0.040 [0.008 ~ 0.059]	~10^5	–	–
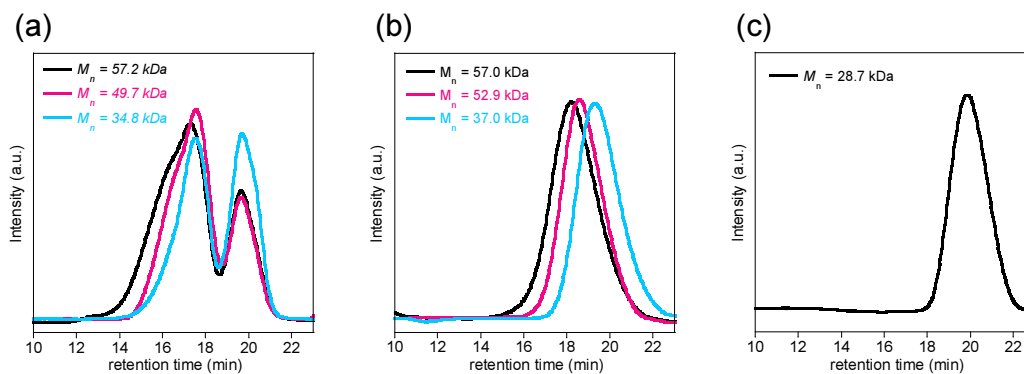
Figure 4-18. GPC charts of PNOz4T (a), PNTz4T (b) and PNSz4T (c). For PNOz4T and PNTz4T, the $M_n = 49.7$ kDa and $M_n = 52.9$ kDa batches were used for all the measurements. Other batches were used for testing the OFET devices to confirm the molecular weight dependency.

Table 4-6. Molecular weight of PNOz4T and PNTz4T.

Polymer	M_n (kDa)[a]	M_w (kDa)[a]	PDI[a]	DP_n[b]
	57.2	416.8	7.3	47.2
PNOz4T	49.7	240.8	4.8	41.0
	34.8	152.1	4.4	28.7
	57.0	152.9	2.7	45.8
PNTz4T	52.9	113.5	2.1	42.5
	37.0	79.8	2.2	29.7

[a]Determined by GPC using polystyrene standard and DCB as the eluent at 140 °C. [b]Based on the repeating unit.
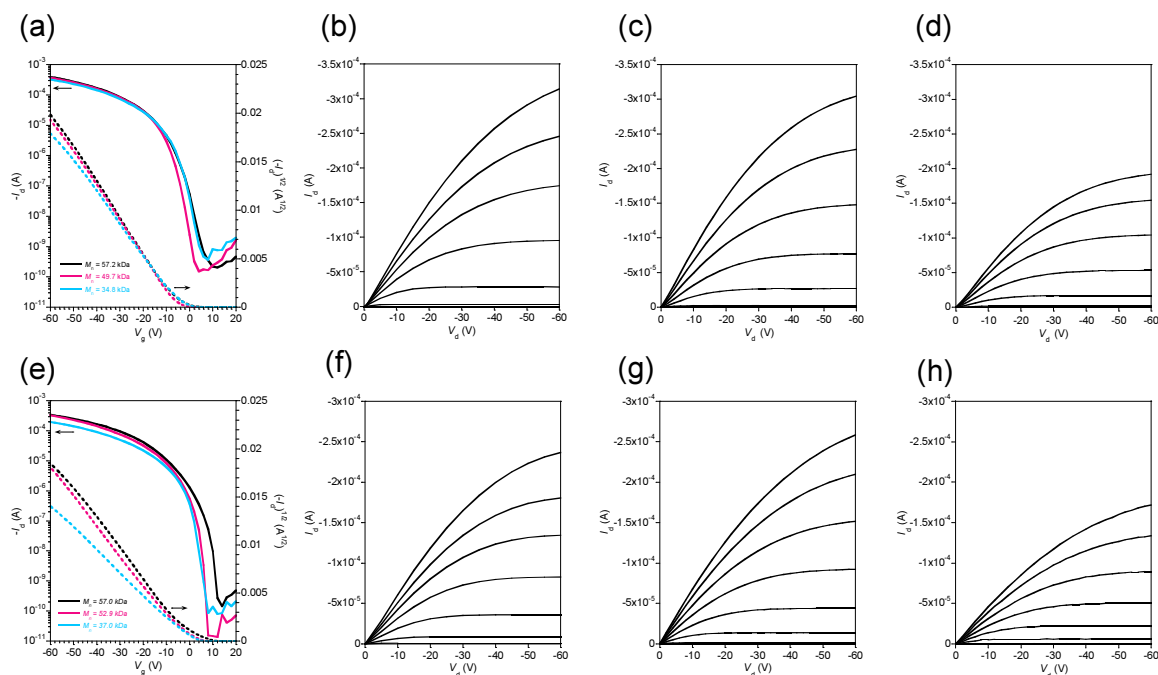
Figure 4-19. Current–voltage characteristics of OFET devices fabricated with PNOz4T (a–d), PNTz4T (e–h). Transfer curves of the OFET devices using PNOz4T with different molecular weights (a), output curves of the devices using PNOz4T with M_n = 57.2 kDa (PDI = 7.3) (b), M_n = 49.7 kDa (PDI = 4.8) (c), M_n = 34.8 kDa (PDI = 4.4) (d). Transfer curves of the device using PNTz4T with different molecular weights (e), output curves of the devices using PNTz4T with M_n = 57.0 kDa (PDI = 2.7) (f), M_n = 52.9 kDa (PDI = 2.1) (g), M_n = 37.0 kDa (PDI = 2.2) (h). see details for the molecular weight in Table 4-6.

Table 4-7. OFET characteristics of the polymers with different molecular weights.

Polymer	M_n (kDa) / PDI	FDTS	
		p-channel	
		μ_h (cm^2/Vs)	I_{on}/I_{off}
PNOz4T	57.2 / 7.3	0.52 [0.24 ~ 0.84]	~10^7
	49.7 / 4.8	0.55 [0.22 ~ 1.0]	~10^7
	34.8 / 3.3	0.34 [0.19 ~ 0.56]	~10^7
PNTz4T	57.0 / 2.7	0.24 [0.17 ~ 0.36]	~10^6
	52.9 / 2.1	0.23 [0.18 ~ 0.56]	~10^7
	37.0 / 2.2	0.16 [0.12 ~ 0.18]	~10^7

**4-3. High-efficiency polymer solar cells with small photon energy loss**

A crucial issue facing polymer-based bulk-heterojunction solar cells (PSCs) is how to manage the energetics of the polymer/fullerene blends in order to maximize short-circuit current density (J_{SC}) and open-circuit voltage (V_{OC}) at the same time and thus the power conversion efficiency (PCE). It is a well-known fact that there is a trade-off between those two parameters and thus, minimizing the trade-off is one of the most crucial issues. A key to resolving the issue in PSCs is to reduce the relatively large photon energy loss (E_{loss}), which is defined by $E_g - eV_{OC}$, where E_g is the optical bandgap of the semiconducting polymer evaluated from the absorption edge.[27-31] The E_{loss} in recently reported high-efficiency PSCs is typically 0.7–1.0 eV,[28] which is larger than those in inorganic solar cells and perovskite solar cells, which are around 0.4–0.5 eV.[29, 30] Very recently, some particular polymers were reported to have small E_{loss}s in PSCs when used in combination with [6,6]-phenyl-C_{61}-butyric acid methyl ester (PC$_{61}$BM) or [6,6]-phenyl-C_{71}-butyric acid methyl ester (PC$_{71}$BM). Bazan and co-workers demonstrated that the use of a pyridylthiadiazole-based polymer reduced E_{loss} in the PSC to ca. 0.6 eV, which leads to a relatively high V_{OC} of 0.86 V even though the polymer has a narrow E_g of 1.47 eV.[28] Shortly thereafter, Janssen and co-workers showed that the use of thiazole-linked diketopyrrolopyrrole (DPP-2Tz) polymers having E_gs of around 1.44–1.53 eV reduced E_{loss} below 0.55 eV, resulting in high V_{OC}s higher than 0.92 V.[31] Although PSCs based on those polymers could potentially afford both high J_{SC} and V_{OC}, J_{SC}s were in fact relatively low and PCEs were limited to 5–6% because of the trade-off.

The trade-off between J_{SC} and V_{OC} is also strongly related to the match of the molecular orbital energy levels between the polymer and fullerene. Given the fundamental working mechanism of PSCs, the realization of both high J_{SC} and V_{OC} requires that the polymer must have both a narrower E_g and a deeper highest occupied molecular orbital (HOMO) energy level.[32] However, this inevitably results in a deeper lowest unoccupied molecular orbital (LUMO) energy level, diminishing the energy offset of the LUMOs between the polymer and fullerene (ΔE_L), which is considered as a driving force for the photoinduced charge separation. This eventually causes a loss of the driving force, in turn being detrimental to the PCE

improvement. In this regard, synthetic chemist face a formidable challenge: to create new semiconducting polymers in order to manage the energetics between polymers and fullerenes and thus to minimize the trade-off.

4-3-1. Evaluation of PCBMs

First, I evaluated the HOMO and LUMO energy levels of PCBM by cyclic voltammetry (CV). Figure 4-20a depicts the cyclic voltammograms of $PC_{61}BM$ and $PC_{71}BM$ in the solution. The HOMO and LUMO energy levels (E_H^{CV} and E_L^{CV}) were determined using the redox onset potential (vs Fc/Fc$^+$) of cyclic voltammograms. E_Hs of $PC_{61}BM$ and $PC_{71}BM$ were -5.85 eV and -5.77 eV, respectively. E_Ls of $PC_{61}BM$ and $PC_{71}BM$ were -3.77 eV and -3.78 eV, respectively. The values for PCBMs agree well with the reported values.[33] Photoelectron spectroscopy in air (PESA) was also carried out using the PCBM thin films to evaluate the HOMO energy levels (E_H^{PESA}) of the PCBMs (Figure 4-20b). E_H^{PESA}s of $PC_{61}BM$ and $PC_{71}BM$ were -6.20 and -6.15 eV, respectively, which were similar tendency with E_H^{CV}. LUMO energy levels (E_L^{opt}) were calculated by the addition of optical band gap (E_g) to E_H^{PESA}s, which were -4.01 and -4.31 eV for $PC_{61}BM$ and $PC_{71}BM$, respectively. The difference between E_L^{CV} and E_L^{opt} can be ascribed to exciton binding energy.[22]
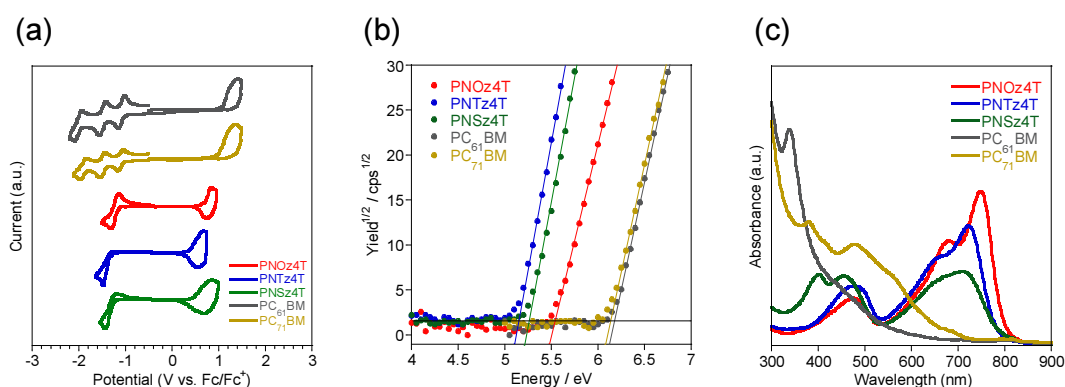

Figure 4-20. Cyclic voltammograms (a), photoelectron spectra (b), UV-vis absorption spectra (c) of PNOz4T, PNTz4T, PNSz4T, $PC_{61}BM$ and $PC_{71}BM$.

Table 4-8. Physicochemical properties of the polymers and PCBMs.

Polymer	E_H^{CV} (eV)[a]	E_L^{CV} (eV)[a]	E_H^{PESA} (eV)[b]	E_L^{opt} (eV)[c]	λ_{edge} (nm)[b]	E_g^{opt} (eV)
PNOz4T	-5.48	-3.65	-5.50	-3.98	815	1.52
PNTz4T	-5.14	-3.46	-5.15	-3.59	793	1.56
PNSz4T	-5.22	-3.55	-5.25	-3.69	792	1.56
PC$_{61}$BM	-5.87	-3.77	-6.20	-4.01	566	2.19
PC$_{71}$BM	-5.77	-3.76	-6.15	-4.31	673	1.84

[a]HOMO (E_H^{CV}) and LUMO (E_L^{CV}) energy levels evaluated using E_{ox} and E_{red}, respectively. [b]HOMO energy level (E_H^{PESA}) evaluated by photoelectron spectroscopy in air. [c]LUMO energy level (E_L^{opt}) calculated by the addition of the optical band gap (E_g) to E_H^{PESA}. [d]Absorption onset. [e]Optical band gap calculated by using λ_{edge}.

Figure 4-21 displays the energy diagrams of PNOz4T, PNTz4T, PNSz4T and PCBMs system using E_H^{CV}s and E_L^{CV}s. It is noted that whereas ΔE_L for PNTz4T (between PCBMs) is 0.31 eV, that for PNOz4T is 0.12 eV, which is much smaller than the widely referenced empirical threshold value of 0.3 eV.[34] This indicates that the driving force of the photoinduced charge separation is reduced in the PNOz4T system compared with the PNTz4T system. Note that, however, the estimation of the energetics based on E_H and E_L evaluated by the measurements on the isolated polymer and PCBMs is considered to neglect the influence of exciton binding energy and other interfacial effects.[22, 35]
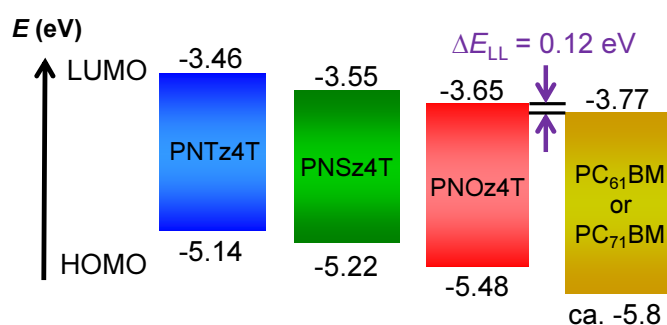
Figure 4-21. Energy diagrams of PNXz4T and PCBMs, where the values were estimated by cyclic voltammetry.

4-3-2. Solar cell properties

The solar cells were fabricated using an inverted architecture, indium–tin-oxide (ITO)/ZnO/polymer:PCBM/MoO$_x$/Ag, where the active layer was spin-coated from the blend solution in CB. Figures 4-22a and 4-22b depict the current density (J)–voltage (V) curves and the external quantum efficiency (EQE) spectra of the cells, respectively, and Table 4-9 summarizes the photovoltaic parameters. The low crystallinity of PNSz4T contribute unfavorable factors for J_{SC} and FF (Figure 4-25c). Consequently, PNTz4TF$_4$ exhibits low PCEs of 1.8% using PC$_{61}$BM and 1.6% using PC$_{71}$BM with an active layer thickness of ca. 80 nm. On the other hands, although the driving force of photoinduced charge separation, ΔE_L, is smaller than the empirical threshold, the PNOz4T cells exhibited fairly high PCEs. In the cells with the PNOz4T to PC$_{61}$BM weight (p/n) ratio of 1:1, a significantly high V_{OC} of 1.0 V was obtained (J_{SC} = 9.6 mA cm^{-2}, FF = 0.59, PCE = 5.6%). It should be mentioned that the V_{OC} of 1.0 V is difficult to be achieved even with middle to wide bandgap polymers (Figure 4-23c). With the increase of the PC$_{61}$BM ratio to 1:1.5–1:3, although V_{OC} was slightly decreased, a marked increase in J_{SC} was observed and PCE was as high as 8.8% (J_{SC} = 14.6 mA cm^{-2}, V_{OC} = 0.97 V, FF = 0.62) at the p/n ratio of 1:3. The difference in PCE between the p/n ratios of 1:2 and 1:3 was marginal. The maximum PCE in the PNOz4T cell was 8.9% (J_{SC} = 14.5 mA cm^{-2}, V_{OC} = 0.96 V, FF = 0.64), which was obtained when PC$_{71}$BM was used at the p/n ratio of 1:2. The observed V_{OC}s of 0.96–1.0 V are higher by more than 0.2 V than those observed for the PNTz4T cells (V_{OC} = 0.71–0.74 V),[12] consistent with the difference in the HOMO energy level.
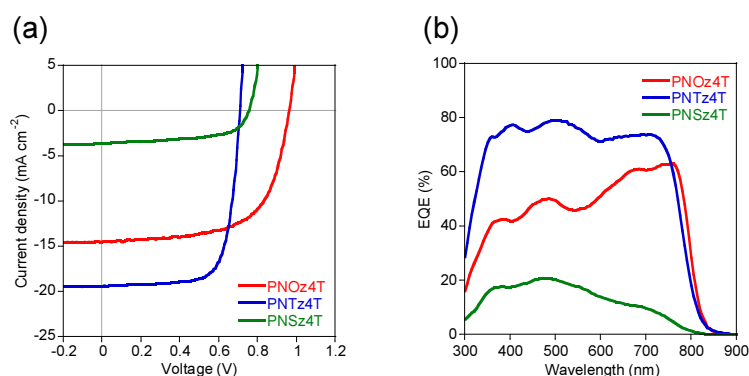
Figure 4-22. J-V curves (a) and EQE spectra (b) of the PNXz4T/PC$_{71}$BM cells with a p/n ratio of 1:2.

Table 4-9. Photovoltaic parameters of the PNXz4T-based cells.

Polymer	PCBM	p/n ratio	J_{SC} (mA cm^{-2})	V_{OC} (V)	FF	PCE (%)
PNOz4T	PC$_{61}$BM	1:3	14.6	0.97	0.62	8.8
	PC$_{71}$BM	1:2	14.5	0.96	0.64	8.9
PNTz4T	PC$_{61}$BM	1:2	18.2	0.73	0.74	9.8
	PC$_{71}$BM	1:2	19.4	0.71	0.73	10.1
PNSz4T	PC$_{61}$BM	1:2	3.8	0.74	0.63	1.8
	PC$_{71}$BM	1:2	3.6	0.75	0.59	1.6
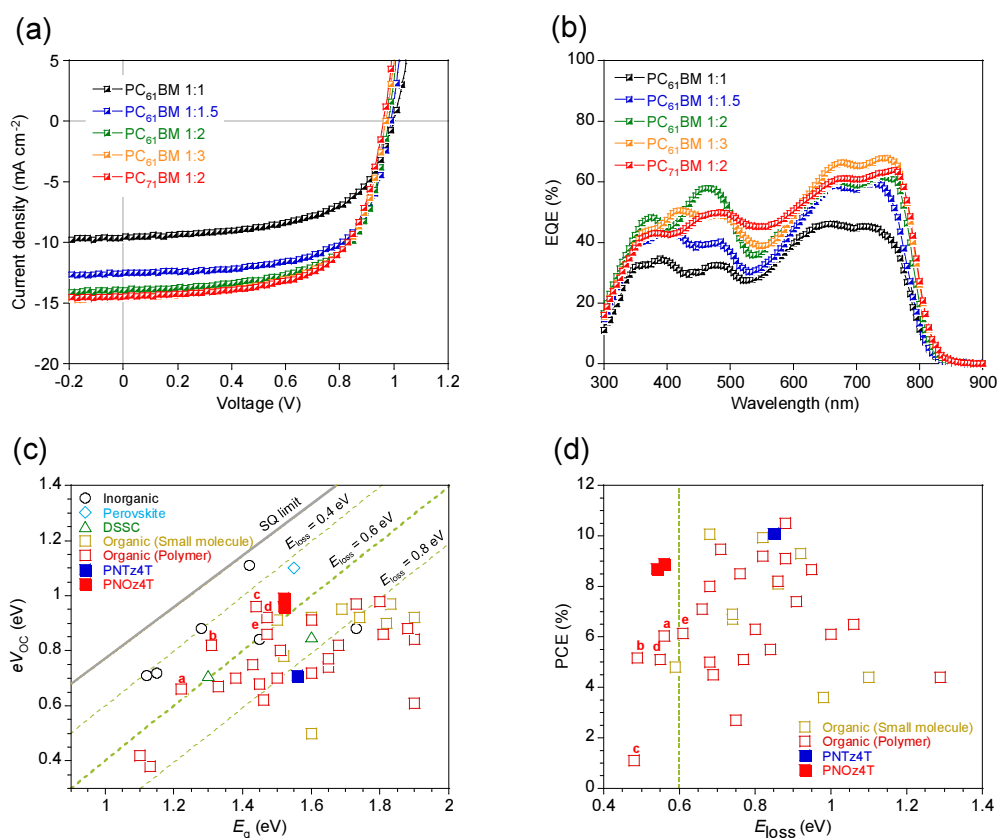
Figure 4-23. (a) J–V curves of PNOz4T/PC$_{61}$BM cells with different polymer to PC$_{61}$BM weight (p/n) ratios and a PNOz4T/PC$_{71}$BM cell with a p/n ratio of 1:2. (b) EQE spectra of PNOz4T/PC$_{61}$BM cells with different polymer to PC$_{61}$BM weight (p/n) ratios and a PNOz4T/PC$_{71}$BM cell with a p/n ratio of 1:2. (c) Plots of eV_{OC} against E_g, which is determined from the absorption onset, for various solar cell systems. The grey line and green dotted line show E_{loss} calculated from the Shockley–Queisser (SQ) theory and E_{loss} = 0.6 eV. (d) Plots of PCE against E_{loss} (= E_g – eV_{OC}) for organic solar cells (small molecules and polymers (PSCs)) extracted from Figure 4-23c. The red squares a–e indicate the polymer systems with $E_{loss} \leq 0.6$ eV.

Table 4-10. Photovoltaic parameters of PNOz4T based solar cells.

PCBM	p/n ratio	thickness (nm)[a]	J_{SC} (mA cm^{-2})[b]	J_{SC}^{EQE} (mA cm^{-2})[c]	V_{OC} (V)	FF	PCE$_{max}$ [PCE$_{ave}$] (%)[d]
PC$_{61}$BM	1:1	195	9.6	10.0	1.0	0.59	5.6 [5.4 ± 0.22]
	1:1.5	185	12.5	12.3	0.99	0.66	8.1 [7.9 ± 0.20]
	1:2	190	14.0	14.1	0.98	0.64	8.7 [8.4 ± 0.25]
	1:3	210	14.6	14.7	0.97	0.62	8.8 [8.5 ± 0.22]
PC$_{71}$BM	1:2	225	14.5	14.5	0.96	0.64	8.9 [8.5 ± 0.20]

[a] Thickness of the active layer. [b] Short-circuit current density observed from the *J–V* measurement. [c] Short-circuit current density calculated from the EQE spectra. [d] PCE$_{max}$: maximum power conversion efficiency, PCE$_{ave}$: average power conversion efficiency with standard deviation from more than 20 devices.

Importantly, as E_g of PNOz4T was 1.52 eV and V_{OC}s of the PNOz4T-based cells were 0.96–1.0 V, E_{loss}s of the PNOz4T/PCBM system were found to be 0.52–0.56 eV, which are significantly reduced from that of the PNTz4T/PCBM system (0.82–0.85 eV)[5, 12] and are even smaller than 0.6 eV that has been referenced as the empirical limit for PSCs.[27] Figure 4-23c depicts the plots of eV_{OC} against E_g for the PNTz4T and PNOz4T systems in comparison with various solar cell systems such as inorganic, perovskite, dye-sensitized (DSSC), small molecule-based organic, and polymer-based organic (PSC) solar cells, in which the lines of E_{loss} estimated by the Shockley–Queisser (SQ) theory[36] and the empirically estimated limit (0.6 eV) are drawn. Figure 4-23d shows the plots of PCE against E_{loss}s for the PNTz4T and PNOz4T systems with other organic systems. These plots were produced referring to the literatures. The red squares of a–e indicate the polymer systems with $E_{loss} \leq 0.6$ eV.[28, 31, 37, 38] It is clear that E_{loss}s of the PNOz4T system are among the lowest values reported so far for PSCs,[28, 31] while the typical values for organic systems are 0.7–1.0 eV (Figure 4-23c). It is noted that E_{loss}s of the PNOz4T system approach the values for inorganic or perovskite solar cells, 0.4–0.5 eV.[29, 30] More importantly, PCEs of the PNOz4T system are in fact the highest values among the organic systems having E_{loss}s ≤ 0.6 eV (Figure 4-23d). Such small

E_{loss}s, as well as the fact that the high V_{OC}s are achievable even with the narrow E_g of 1.52 eV, observed in PNOz4T cells are attributed to the very small ΔE_L of 0.12 eV.

The PNOz4T cells showed EQEs surpassing 60% at the polymer λ_{max} region, except for the cells that used PC$_{61}$BM with the p/n ratio of 1:1. The highest EQE of 66% was obtained when PC$_{61}$BM was used with a p/n ratio of 1:3. These EQE values for the PNOz4T cells were lower than those for the PNTz4T cells (EQE = ~75% at λ_{max}), which reflects the lower J_{SC} despite the fact that PNOz4T has an absorption range, *i.e.*, E_g, similar to that for PNTz4T. This issue will be further discussed later in this paper. We note here that, however, these EQE values are quite high for the polymer/PCBM systems with such a small energy offset, *i.e.* ΔE_L or $E_g - E_{CT}$. For instance, although the system of DPP-2Tz polymers/PC$_{71}$BM was reported to have small ΔE_Ls of 0.09–0.21 eV and provide high V_{OC}s of more than 0.9 V, it only showed low EQEs of 5–40%, which resulted in low J_{SC}s of 2.0–8.8 mA cm^{-2}.[31] Similarly high EQEs with the small energy offset were previously reported by Vandewal and co-workers, in which isoindigo-based polymers with $E_g - E_{CT}$ of ~0.0 eV and ~0.1 eV showed IQE of ~45% (EQE = ~30%) and ~87% (EQE = ~60%).[39] However, in this case, PCEs were limited to 4.5% (V_{OC} = 0.91 V)[40] and 6.3% (V_{OC} = 0.70 V), respectively.[41] Therefore, to the best of our knowledge, demonstrating high PCEs of ~9% with high V_{OC}s of ~1 V, small E_{loss}s, and a small energy offset at the same time, PNOz4T is regarded as quite a unique narrow bandgap polymer.

4-3-3. Charge transport properties

The charge carrier mobility of PNOz4T was evaluated for hole-only devices (ITO/PEDOT:PSS/PNOz4T:PCBM/MoO$_x$/Ag) by using the space-charge-limited current (SCLC) model, where the p/n ratios were 1:3 and 1:2 for PC$_{61}$BM and PC$_{71}$BM, respectively. I could not measure well the charge carrier mobility of PNSz4T. Blend films with PC$_{61}$BM and PC$_{71}$BM exhibited hole mobilities of 2.4 × 10^{-3} cm^2 V^{-1} s^{-1} and 1.7 × 10^{-3} cm^2 V^{-1} s^{-1}, respectively, which are high for semiconducting polymers. To confirm the balance of the charge carrier transport between hole and electron, I also

fabricated electron-only devices using the blend films (ITO/ZnO/PNOz4T:PCBM/LiF/Al) with the same p/n ratios as the hole-only devices. Electron mobility was also of order 10^{-3} cm^2 V^{-1} s^{-1}; it was 2.6×10^{-3} cm^2 V^{-1} s^{-1} and 1.5×10^{-3} cm^2 V^{-1} s^{-1} for the blend films with PC$_{61}$BM and PC$_{71}$BM, respectively. These results indicate that the hole and electron transports are well-balanced in the PNOz4T/PCBM blend films.
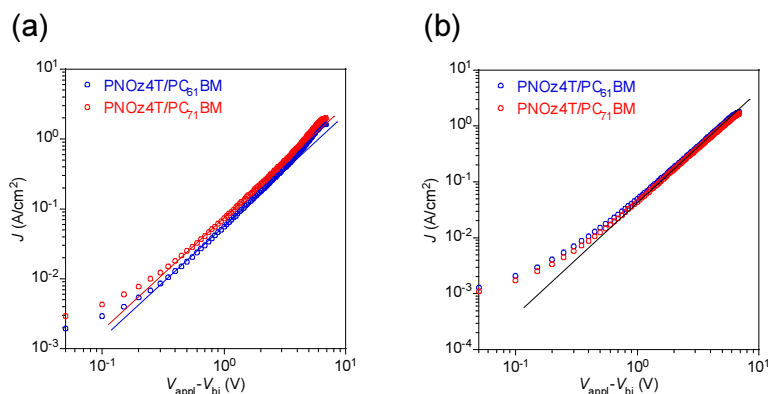

Figure 4-24. *J-V* curves of hole-only devices and electron-only devices of PNOz4T/PCBM films. (a) Hole-only devices: ITO/PEDOT:PSS/PNOz4T:PCBM/MoOx/Ag. (b) Electron-only devices: ITO/ZnO/PNOz4T:PCBM/LiF/Al. The p/n ratios were 1:3 for PC$_{61}$BM and 1:2 for PC$_{71}$BM.

4-3-4. Thin film characterization.

The ordering structure of PNXz4T in the thin film blended with PC$_{61}$BM and PC$_{71}$BM (p/n ratio = 1:2) was investigated by grazing incidence wide-angle diffraction (GIXD) measurements (Figure 4-25).[42] The two-dimensional diffraction (2D GIXD) image provided diffractions corresponding to the lamellar structure, (*h*00), and the π–π stacking structure, (010), at the small angle region and the wide angle region, respectively, which are typical of semiconducting polymers (Figure 4-25).[43] Both the lamellar and the π–π stacking diffractions are present along both the q_z and q_{xy} axes, indicative of the coexistence of edge-on and face-on orientations where the backbone plane stands and lies flat on the substrate, respectively. In PNOz4T, the π–π stacking distance was determined to be 3.5 Å from the cross-sectional profiles of the 2D GIXD image (Figure 4-26), which is narrow for semiconducting polymers. The GIXD study suggests that PNOz4T forms a highly crystalline structure in the blend film, which, together with the presence of

face-on crystallites, is in good agreement with the high out-of-plane mobility and thus the high photovoltaic performance of PNOz4T. On the contrary, only a weak diffraction in the small-angle region was observed for PNSz4T, indicative of an amorphous nature.
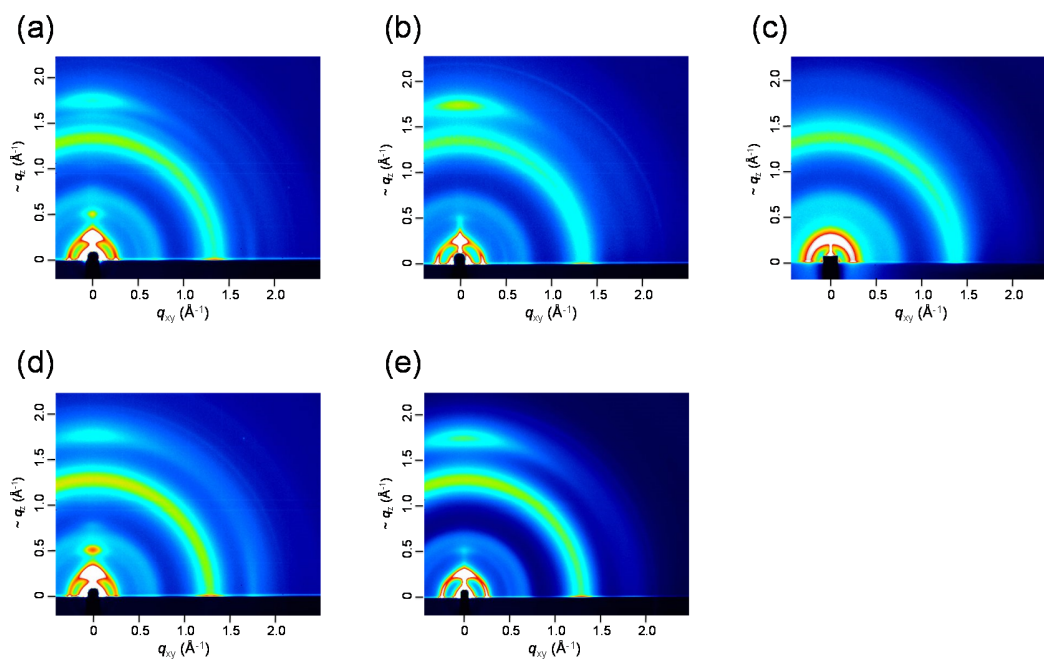
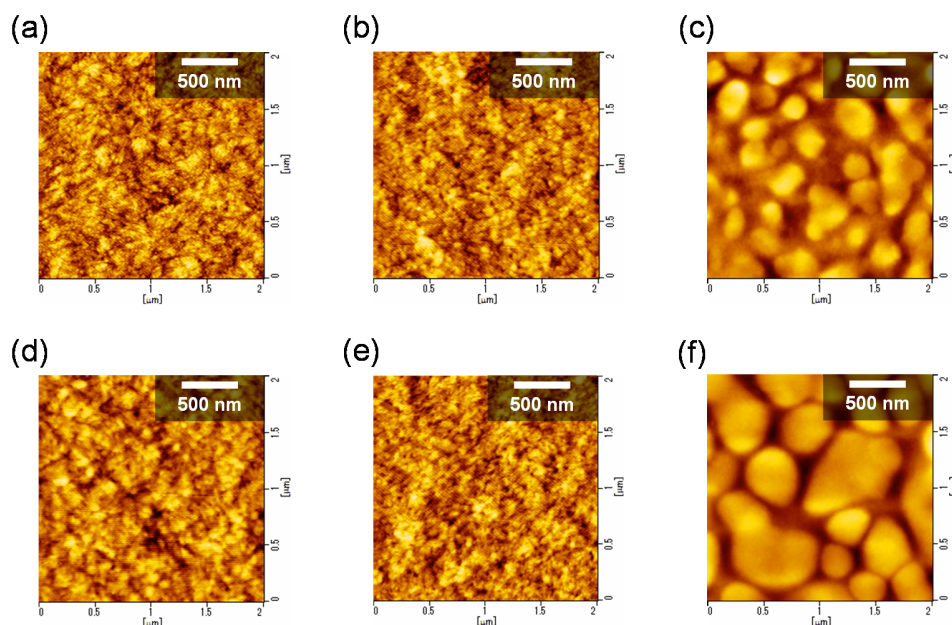**Figure 4-25.** 2D GIXD images of the polymer/PCBM (1:2 wt ratio) films spun on ZnO-coated glass/ITO substrate. PNOz4T/PC$_{61}$BM (a), PNTz4T/PC$_{61}$BM (b), PNSz4T/PC$_{61}$BM (c), PNOz4T/PC$_{71}$BM (d), PNTz4T/PC$_{71}$BM (e).
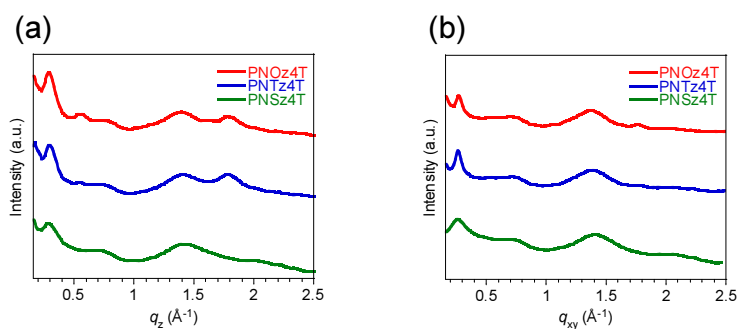

Figure 4-26. The cross-sectional profiles along the q_z (a) and q_{xy} (b) axes of the polymer/PC$_{61}$BM films on ZnO-coated glass/ITO substrate, respectively

The surface morphological structure of polymer/PCBM blend films were investigated by using the atomic force microscopy (AFM). Figure 4-27 displays the topographic AFM images. The obtained root-mean-square roughness (RMS) values are 1.12, 0.96 and 4.58 nm for PNOz4T/PC$_{61}$BM, PNTz4T/PC$_{61}$BM, and PNSz4T/PC$_{61}$BM, respectively. This tendency was similar in polymer/PC$_{71}$BM. PNOz4T and PNTz4T show a texture with well phase-separated domains, which are favorable for efficient charge separation and transport. This results in gives much higher PCE. However, the PNOz4T/PCBM film gave slightly larger domains than the PNTz4T/PCBM film. This is probably because PNOz4T has stronger aggregation property than PNTz4T. On the contrary, PNSz4T blend films afford the greater phase segregation and rougher surfaces.

Transmission electron microscopy (TEM) of PNOz4T/PC$_{71}$BM and PNTz4T/PC$_{71}$BM blend films with the p/n ratio of 1:2 are shown in Figure 4-28. The TEM images revealed good phase separation with bicontinuous networks for both polymer systems.[44] It is noted that the PNOz4T/PC$_{71}$BM film gave relatively large domains compared with the PNTz4T/PC$_{71}$BM film. The domain sizes (fibril widths) of the PNTz4T/PC$_{71}$BM and PNOz4T/PC$_{71}$BM films were roughly 15–30 nm and 20–60 nm, respectively.

Figure 4-27. AFM images of the polymer/PCBM (1:2 wt ratio) films spun on ZnO-coated glass/ITO substrate. PNOz4T/PC$_{61}$BM (a), PNTz4T/PC$_{61}$BM (b), PNSz4T/PC$_{61}$BM (c), PNOz4T/PC$_{71}$BM (d), PNTz4T/PC$_{71}$BM (e), PNSz4T/PC$_{71}$BM (f).

(a)   (b)
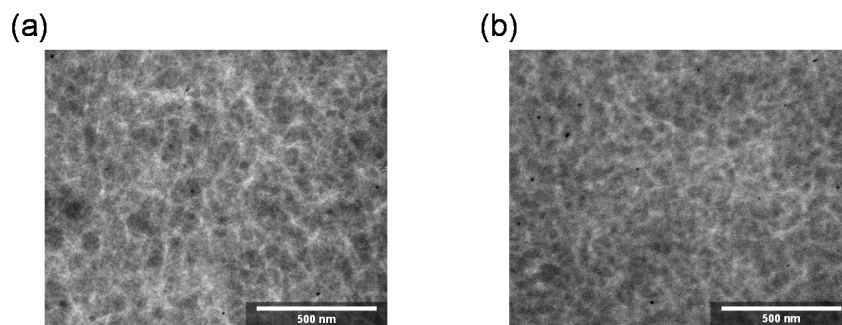
Figure 4-28. TEM images of PNOz4T/PC$_{71}$BM (a) and PNTz4T/PC$_{71}$BM (b) films with the p:n ratio of 1:2.

4-4. Conclusion of chapter 4

I have synthesized oxygen and selenium analogues of naphthobischalcogenadiazole, namely, naphthobisoxadiazole (NOz) and naphthobisselenadiazole (NSz), and the corresponding polymers. I found that NOz and NSz had high electron deficiency compared with the sulfur analogue, naphthobisthiadiazole (NTz), which is different from the trend observed in acenedichalcogenophenes. This is probably because the electron negativity of the chalcogen atom is the dominant factor for the frontier orbital energy levels. It is also found that although all the model compounds, NXz2T, were similarly coplanar in the single crystals, steric repulsion between NXz and the adjacent thiophene rings seems to be larger as the chalcogen atom become heavier. The difference of the steric repulsion can rationalize the difference in the electronic structure of NXz2T-DT and PNXz4T, and the ordering structure of PNXz4T, whereas PNOz4T exhibited bathochromic shift in the absorption and similarly high crystallinity in the film, PNSz4T exhibited hypsochromic shift and amorphous-like structure as compared to PNTz4T. Thanks to the higher electron deficiency, the NOz and NSz-based polymers, PNOz4T and PNSz4T, respectively had deeper LUMO energy levels than the NTz-based polymer, PNTz4T. Notably, the LUMO energy level of PNOz4T was found to be –3.65 eV by electrochemistry and –4.00 eV by spectroscopies, which is around the borderline for allowing ambient n-channel behavior in OFETs. In fact, whereas PNSz4T showed only p-channel behavior, as is the case in PNTz4T, PNOz4T exhibited a p-channel and an ambipolar behavior depending on the surfactant used in OFETs. It is also mentioned that

the mobilities of PNOz4T were significantly higher than those of PNSz4T, which was consistent with the higher crystallinity of PNOz4T. The hole mobility of PNOz4T in the p-channel devices reached 1 cm^2/Vs, which was even higher than that of PNTz4T. In the ambipolar devices, PNOz4T demonstrated well-balanced and relatively high hole and electron mobilities of ~0.5 cm^2/Vs and ~0.3 cm^2/Vs, respectively. I have shown the clear correlation between the chalcogen atom in the NXz unit and the properties of the corresponding polymers.

Although bulk heterojunction solar cells based on the PNSz4T/PC$_{71}$BM blend film gave lower power conversion efficiency (PCE) of ~1.6%, those of PNOz4T/PC$_{71}$BM blend film exhibited as high as 8.9% PCE in single-junction inverted cells, along with remarkably high V_{OC}s of up to ~1 V despite the fact that the polymer had a narrow bandgap of 1.52 eV. I primarily highlighted that E_{loss}s in this system, 0.52–0.56 eV, were found to be among the smallest values for PSCs, which were smaller than the empirical limit of 0.6 eV referenced to date, and were close to the values for inorganic solar cells. Another interesting feature is that, closely related to the small E_{loss}, the energy offset (ΔE_L and $E_g - E_{CT}$) that is a driving force for the photoinduced charge separation is very small. In particular, ΔE_L, a widely referenced important parameter in designing p-type (donor) semiconducting polymers, was 0.12 eV, which is much smaller than the empirical threshold value of 0.3 eV for efficient photoinduced charge separation. Overall, to the best of my knowledge, PNOz4T is the highest performing narrow bandgap polymer in terms of having several unconventional aspects at the same time: V_{OC} of ~1 V and E_{loss} of ~0.5 eV (and almost negligible energy offset), which are among the highest and smallest values for PSCs reported so far, respectively. Collaborative study of charge generation dynamics in comparison with the PNTz4T system revealed that the relatively low EQE (~66%) of the PNOz4T system originates in the relatively large domain size of the blend films and not in the small ΔE_L. Thus, it is expected that further modification of the polymer structure and/or optimization of the morphology of the blend film can still improve EQE and thus J_{SC}. Although further studies are necessary to understand why such a high performance is achievable even

with a small energy offset, our results opens the door to the realization of both high J_{SC} and V_{OC} at the same time, and thus the high PCE such as 15% in single junction cells.

4-5. Experimental section

Synthesis

2,6-Diamino-1,5-dinitronaphthalene (**1**),[14] 1,2,5,6-tetraaminonaphthalene (**3**),[14] 4-(2-decyltetradecyl)-2-trimethylstannylthiophene (**6**),[5] 5,5′-bis(trimethylstannyl)-2,2′-bithiophene (**9**)[45] were synthesized according to the reported procedure, respectively. Even in the hydrochloride form, **3** gradually changes the color from gray to bluish gray in air, which may affect the synthesis of NSz. It is recommended to store in an inert atmosphere. All chemicals and solvents are of reagent grade unless otherwise indicated. THF and toluene were purified by a Glass Contour Solvent System (Nikko Hansen & Co., Ltd.) prior to use. Polymerization was carried out with a microwave reactor (Biotage Initiator). Nuclear magnetic resonance (NMR) spectra were obtained in deuterated chloroform and DCB (for polymers) with TMS as internal reference by using a JNM-ECS400 (JEOL RESONANCE). EI-MS spectra were obtained with a GCMS-QP-2010SE spectrometer (SHIMADZU) using an electron impact ionization procedure (70 eV). The molecular ion peaks of the chlorine-, bromine-, sulfur-, selenium-, or tin-containing compounds showed a typical isotropic pattern, and all the mass peaks are reported based on ^{35}Cl, ^{32}S, ^{79}Br, ^{80}Se, or ^{120}Sn, respectively. Molecular weights were determined by gel permeation chromatography (GPC) by calibrating with polystyrene standards using a TOSOH HLC-8121GPC/HT at 140 °C with DCB as the solvent.

Naphtho[1,2-c:5,6-c′]bis[1,2,5]oxadiazole (NOz)

1,5-Diamino-2,6-dinitronaphthalene (**1**) (5.00 g, 20.1 mmol), 85 % potassium hydroxide (5.3 g, 80.3 mmol), tetrabutylammonium bromide (0.65 g, 2.02 mmol), dichloromethane (100 mL), and water (13.5 mL) were added to a 300 mL three-neck flask. 10% sodium hypochlorite solution (96.0 g, 129.0 mmol)

was added slowly. After the mixture was stirred at room temperature for 0.5 h, the mixture was refluxed for 2 h. While concentrating the solvent, 50 % ethanol aqueous solution was added slowly. After cooling to 0 °C, the precipitate was filtered, and then washed by water and 50% ethanol aqueous solution. The crude product (a mixture of **2a-c**) as yellow solid was dried in vacuo and used without further purification (3.59 g, 73%). The mixture of **2a-c** (3.22 g, 13.2 mmol) was added to 80 mL of ethanol in a flask. After the mixture was cooled to 0 °C, hydroxylamine hydrochloride (3.67 g, 52.8 mmol) and water (16 mL) was added, and then 85 % potassium hydroxide (7.41 g, 112.3 mmol) and water (16 mL) was added successively. The mixture was stirred at room temperature for 1 h, and subsequently was refluxed for 3 h. Water was added slowly to the reaction mixture, which was then cooled to 0 °C. The precipitate was collected by filtration. After washing with water, the crude product was purified by recrystallization from chloroform/ethanol/water to give NOz as orange solid (2.04 g, 73%). ^{1}H NMR (400 MHz, CDCl$_3$): δ 8.52 (d, J = 9.2 Hz, 2H), 8.09 (d, J = 9.2 Hz, 2H). ^{13}C NMR (100 MHz, CDCl$_3$): δ 148.9, 147.5, 128.6, 122.9, 117.4. EI-MS (70 eV) m/z 212 (M$^+$). Anal. Calcd for C$_{10}$H$_4$N$_4$O$_2$: C, 56.61; H, 1.90; N, 26.41. Found: C, 56.60; H, 2.09; N, 26.21.

Naphtho[1,2-c:5,6-c′]bis[1,2,5]selenadiazole (NSz)

1,2,5,6-Tetraaminonaphthalene tetrahydrochloride (0.50 g, 1.50 mmol) and pyridine (7.8 g) were added to a 300 mL three-neck flask. After cooling to 0 °C, seleninyl chloride (1.10 g, 6.63 mmol) was added dropwise. The solution was heated to 70 °C, and stirred for 2 h. Water was added dropwise into the reaction mixture, which was then cooled to 0 °C. The resulting precipitate was filtered, washed by water and isopropanol, and dried under vacuum. The crude product was purified by recrystallization from DCB to give NSz as dark yellow solid (345 mg, 68%). ^{1}H NMR (400 MHz, DCB-d_4, 150 °C): δ 8.63 (d, J = 9.3 Hz, 2H), 7.76 (d, 2H, J = 9.3 Hz). EI-MS (70 eV) m/z 340 (M$^+$). Anal. Calcd for C$_{10}$H$_4$N$_4$Se$_2$: C, 35.53; H, 1.19; N, 16.57. Found: C, 35.37; H, 1.18; N, 16.45.

5,10-Dibromonaphtho[1,2-c:5,6-c′]bis[1,2,5]oxadiazole (4)

NOz (2.25 g, 10.6 mmol) was dissolved in concentrated sulfuric acid (112.5 g) in a 200 mL three-neck flask. NBS (5.66 g, 31.8 mmol) was added in several portions over the period of 1 h, and then the reaction mixture was stirred for 24 h at room temperature. The reaction mixture was poured into cold water, and the resulting precipitate was filtered. The collected product was washed with water, $NaHCO_3$ aq., ethanol and THF, which was then purified by recrystallization from chloroform/isopropanol to give **4** as yellow solid (2.92 g, 75%). ^1H NMR (400 MHz, $CDCl_3$): δ 8.68 (s, 2H). ^{13}C NMR (100 MHz, $CDCl_3$): δ 149.5, 146.7, 130.6, 122.6, 1110.9. EI-MS (70 eV) m/z 370 (M^+). Anal. Calcd for $C_{10}H_2Br_2N_4O_2$: C, 32.47; H, 0.54; N, 15.14. Found: C, 32.63; H, 0.59; N, 15.09.

5,10-Dibromonaphtho[1,2-c:5,6-c′]bis[1,2,5]selenadiazole (5)

NSz (3.00 g, 8.87 mmol) was dissolved in concentrated sulfuric acid (150 g) in a 200 mL three-neck flask. NBS (4.74 g, 26.6 mmol) was added in several portions over the period of 1 h, and then the reaction mixture was stirred for 6 h at room temperature. The reaction mixture was poured into cold water, and the resulting precipitate was filtered. The collected product was washed with water, $NaHCO_3$ aq., ethanol and THF. The residue was then stirred in hot DCB, filtered and dried in vacuo, giving **5** as dark yellow solid (3.66 g, 83%). ^1H NMR (400 MHz, DCB-d_4, 150 °C): δ 8.81 (s, 2H). EI-MS (70 eV) m/z 496 (M^+). Anal. Calcd for $C_{10}H_2Br_2N_4Se_2$: C, 24.22; H, 0.41; N, 11.30. Found: C, 24.21; H, 0.47; N, 11.27.

5,10-Bis(4-(2-decyltetradecyl)thiophen-2-yl)naphtho[1,2-c:5,6-c′]bis[1,2,5]oxadiazole (NOz2T-DT)

4 (1.02 g, 2.76 mmol), 4-(2-decyl)tetradecyl-2-(trimethylstannyl)thiophene (**6**) (4.02 g, 6.89 mmol), and 136 mL of toluene were added to a 200 mL three-neck flask and purged with argon for 40 min. Tetrakis(triphenylphosphine)palladium(0) (127 mg, 0.110 mmol) was added, and then the reaction mixture was refluxed for 16 h. After cooling to room temperature, KF aq. was added and the mixture was extracted with toluene. The organic layer was washed with water, and then dried over anhydrous $MgSO_4$.

The solvent was removed by vacuum evaporation, and the residue was purified by column chromatography on silica gel with hexane-dichloromethane (3:1), followed by recrystallization from ethyl acetate to give NOz2T-DT as orange solid (2.68 g, 93%). ^{1}H NMR (400 MHz, CDCl$_3$): δ 8.57 (s, 2H,), 8.08 (s, 2H), 7.12 (s, 2H), 2.65 (d, J = 6.9 Hz, 4H), 1.77-1.65 (m, 2H), 1.37-1.18 (m, 80H), 0.86 (t, J = 6.7 Hz, 12H). ^{13}C NMR (100 MHz, CDCl$_3$): δ 148.0, 147.7, 144.1, 136.6, 132.1, 124.3, 124.0, 121.8, 121.5, 38.9, 35.1, 33.3, 31.9, 30.0, 29.7, 29.4, 26.6, 22.7, 14.1. ESI-MS m/z 1050 [M+H]$^+$. Anal. Calcd for C$_{66}$H$_{104}$N$_4$O$_2$S$_2$: C, 75.52; H, 9.99; N, 5.34. Found: C, 75.33; H, 10.02; N, 5.20.

5,10-Bis(4-(2-decyltetradecyl)thiophen-2-yl)naphtho[1,2-c:5,6-c′]bis[1,2,5]selenadiazole   **(NSz2T-DT)**

5 (537 mg, 1.083 mmol), **6** (1.39 g, 2.38 mmol), and 55 mL of toluene were added to a 100 mL three-neck flask and purged with argon for 40 min. Tetrakis(triphenylphosphine)palladium(0) (50.0 mg, 0.043 mmol) was added, and then the reaction mixture was refluxed for 16 h. After cooling to room temperature, KF aq. was added and the mixture was extracted with toluene. The organic layer was washed with water, and then dried over anhydrous MgSO$_4$. The solvent was removed by vacuum evaporation, and the residue was purified by column chromatography on silica gel with hexane-dichloromethane (2:1), followed by recrystallization from ethyl acetate to give NSz2T-DT as purple solid (1.02 g, 80%). ^{1}H NMR (400 MHz, CDCl$_3$): δ 9.00 (s, 2H), 8.00 (d, J = 1.2 Hz, 2H), 7.09 (s, 2H), 2.65 (d, J = 6.8 Hz, 4H), 1.77-1.67 (m, 2H), 1.40-1.17 (m, 80H), 0.86 (t, J = 6.9 Hz, 12H). ^{13}C NMR (100 MHz, CDCl$_3$): δ 158.5, 157.9, 142.8, 138.8, 130.1, 128.0, 126.3, 123.7, 123.4, 39.0, 35.2, 33.4, 31.9, 30.1, 29.7, 29.7, 29.4, 26.7, 22.7, 14.1. ESI-MS m/z 1178 [M+H]$^+$. Anal. Calcd for C$_{66}$H$_{104}$N$_4$S$_2$Se$_2$: C, 67.43; H, 8.92; N, 4.77. Found: C, 67.34; H, 8.95; N, 4.65.

5,10-Bis(5-bromo-4-(2-decyltetradecyl)thiophen-2-yl)naphtho[1,2-c:5,6-c′]bis[1,2,5]oxadiazole (7)

NOz2T-DT (2.68 g, 2.56 mmol) and 210 mL of THF were added to a 300-mL three-neck flask and cooled to 0 °C. NBS (1.08 g, 6.09 mmol) was added, and the reaction mixture was stirred for 18 h at room temperature. NaHCO$_3$ aq. was added, and the mixture was extracted with toluene. The organic layer was washed with brine, and then dried over anhydrous MgSO$_4$. The solvent was removed by vacuum evaporation, and the residue was purified by column chromatography on silica gel with hexane-dichloromethane (2:1), followed by twice recrystallization from ethyl acetate to give **7** as red solid (2.72 g, 88%). ^{1}H NMR (400 MHz, CDCl$_3$): δ 8.44 (s, 2H), 7.92 (s, 2H), 2.60 (d, J = 7.1Hz, 4H), 1.83-1.72 (m, 2H), 1.44-1.16 (m, 80H), 0.86 (t, J = 6.8 Hz, 12H). ^{13}C NMR (100 MHz, CDCl$_3$): δ 147.8, 147.3, 143.6, 136.2, 131.6, 123.2, 121.5, 121.5, 114.2, 38.6, 34.3, 33.4, 31.9, 30.0, 29.7, 29.4, 26.6, 22.7, 14.1. ESI-MS m/z 1208 [M+H]$^+$. Anal. Calcd for C$_{66}$H$_{102}$N$_4$O$_2$S$_2$: C, 65.65; H, 8.51; N, 4.64. Found: C, 65.54; H, 8.54; N, 4.52.

5,10-Bis(5-bromo-4-(2-decyltetradecyl)thiophen-2-yl)naphtho[1,2-c:5,6-c′]bis[1,2,5]selenadiazole (8)

NSz2T-DT (223 mg, 0.190 mmol) and 14 mL of THF were added to a 50 mL three-neck flask and cooled to 0 °C. NBS (71.0 mg, 0.399 mmol) was added, and the reaction mixture was stirred for 3 h at room temperature. NaHCO$_3$ aq. was added, and the mixture was extracted with toluene. The organic layer was washed with brine, and then dried over anhydrous MgSO$_4$. The solvent was removed by vacuum evaporation, and the residue was purified by column chromatography on silica gel with hexane-dichloromethane (2:1), followed by twice recrystallization from ethyl acetate to give **8** as purple solid (203 mg, 80%). ^{1}H NMR (400 MHz, CDCl$_3$): δ 8.81 (s, 2H), 7.75 (s, 2H), 2.59 (d, J = 7.2 Hz, 4H), 1.84-1.73 (m, 2H), 1.43-1.16 (m, 40H), 0.85 (t, J = 6.8 Hz, 6H). ^{13}C NMR (100 MHz, CDCl$_3$): δ 158.0, 157.3, 141.9, 138.2, 128.7, 126.9, 126.0, 122.2, 113.9, 38.7, 34.4, 33.4, 31.9, 30.1, 29.7, 29.7, 29.4, 26.6, 22.7,

14.1. ESI-MS *m/z* 1335 [M$^+$+H]. Anal. Calcd for C$_{66}$H$_{102}$Br$_2$N$_4$S$_2$Se$_2$: C, 59.45; H, 7.71; N, 4.20. Found: C, 59.40; H, 7.74; N, 4.07.

PNOz4T

7 (120.7 mg, 0.10 mmol), **9** (49.2 mg, 0.10 mmol), tetrakis(triphenylphosphine)palladium(0) (2.30 mg, 2 μmol) and toluene (4 mL) were added in a 5 mL reaction vessel. The vessel was purged with argon and subsequently sealed. The vessel was put into a microwave reactor and heated at 140 °C for 24 min. After cooling to room temperature, the reaction mixture was poured into a mixture of methanol (100 mL) and concentrated hydrochloric acid (10 mL), and then vigorously stirred for 6 h at room temperature. The precipitate was filtered and subjected to sequential Soxhlet extraction with methanol, hexane, chloroform to remove low molecular weight fraction. The residue was extracted with CB, which was reprecipitated in methanol. The precipitate was filtered and dried in vacuo, yielding PNOz4T (114 mg, 94%) as metallic purple solid. GPC (DCB, 140 °C): M_n = 49.7 kDa, M_w = 240.8 kDa, PDI = 4.8. ^{1}H NMR (400 MHz, DCB-d_4, 150 °C): δ 8.51 (s, 2H), 8.22 (s, 2H), 7.25 (m, 2H), 7.24 (m, 2H), 2.97 (m, 4H), 2.01 (m, 2H), 1.18-1.58 (m, 80H), 0.84 (m, 12H). Anal. Calcd for C$_{74}$H$_{106}$N$_4$O$_2$S$_4$: C, 73.34; H, 8.82; N, 4.62. Found: C, 73.10; H, 8.78; N, 4.38.

PNSz4T

8 (66.7 mg, 0.05 mmol), **9** (24.6 mg, 0.05 mmol), tetrakis(triphenylphosphine)palladium(0) (1.15 mg, 1 μmol), and toluene (2 mL) were added to a 2 mL reaction vessel. The vessel was purged with argon and subsequently sealed. The vessel was put into a microwave reactor and heated at 180 °C for 48 min. After cooling to room temperature, the reaction mixture was poured into a mixture of methanol (100 mL) and concentrated hydrochloric acid (10 mL), and then vigorously stirred for 6 h at room temperature. The precipitate was filtered and subjected to sequential Soxhlet extraction with methanol, hexane, chloroform to remove low molecular weight fraction. The residue was extracted with CB, which was reprecipitated

in methanol. The precipitate was filtered and dried in vacuo, yielding PNSz4T (45 mg, 67%) as metallic dark purple solid. GPC (DCB, 140 °C): M_n = 28.7kDa, M_w = 60.6 kDa, PDI = 2.1. ^{1}H NMR (400 MHz, DCB-d_4, 150 °C): δ 9.10 (s, 2H), 8.27 (s, 2H), 7.25 (m, 2H), 7.22 (m, 2H), 3.00 (m, 4H), 2.05 (m, 2H), 1.17-1.63 (m, 80H), 0.83 (m, 12H). Anal. Calcd for $C_{74}H_{106}N_4S_4Se_2$: C, 66.44; H, 7.99; N, 4.19. Found: C, 66.12; H, 8.27; N, 3.77.

5,10-Bis(4-methylthiophen-2-yl)naphtho[1,2-c:5,6-c′]bis[1,2,5]oxadiazole (NOz2T)

4 (185 mg, 0.500 mmol), 4-methyl-2-trimethylstannylthiophene (300 mg, 1.15 mmol), and 25 mL of toluene were added to a 50 mL three-neck flask and purged with argon for 40 min. Tetrakis(triphenylphosphine)palladium(0) (23.0 mg, 0.020 mmol) was added, and then the reaction mixture was refluxed for 16 h. After cooling to room temperature, KF aq. was added and the mixture was extracted with toluene. The organic layer was washed with water, and then dried over anhydrous MgSO$_4$. The solvent was removed by vacuum evaporation, and the residue was purified by column chromatography on silica gel with chloroform, followed by recrystallization from chloroform/ethyl acetate to give NOz2T as red solid (152 mg, 75%). For the X-ray crystal structural analysis, NOz2T-Me was further purified by sublimation. ^{1}H NMR (400 MHz, CDCl$_3$): δ 8.56 (s, 2H), 8.07 (d, 2H, J = 1.2 Hz), 7.13 (t, 2H, J = 1.2 Hz), 2.39 (d, 6H, J = 1.2 Hz). EI-MS (70 eV) m/z 404 (M$^+$). Anal. Calcd for $C_{20}H_{12}N_4O_2S_2$: C, 59.39; H, 2.99; N, 13.85. Found: C, 59.39; H, 3.03; N, 13.86.

5,10-Bis(4-methylthiophen-2-yl)naphtho[1,2-c:5,6-c′]bis[1,2,5]selenadiazole (NSz2T)

5 (496 mg, 1.00 mmol), 4-methyl-2-trimethylstannylthiophene (601 mg, 2.30 mmol), and 40 mL of toluene were added to a 50 mL three-neck flask and purged with argon for 40 min. Tetrakis(triphenylphosphine)palladium(0) (46.0 mg, 0.040 mmol) was added, and then the reaction mixture was refluxed for 16 h. After cooling to room temperature, KF aq. was added and the mixture was extracted with toluene. The organic layer was washed with water, and then dried over anhydrous MgSO$_4$.

The solvent was removed by vacuum evaporation, and the residue was purified by recrystallization from toluene/ethanol to give NSz2T as purple solid (500 mg, 94%). For the X-ray crystal structural analysis, NSz2T-Me was further purified by sublimation. ^{1}H NMR (400 MHz, CDCl$_3$): δ 9.05 (s, 2H), 8.03 (d, 2H, J = 1.2 Hz), 7.10 (t, 2H, J = 1.2 Hz), 2.40 (d, 6H, J = 1.2 Hz). EI-MS m/z 532 (M$^+$). Anal. Calcd for C$_{20}$H$_{12}$N$_4$S$_2$Se$_2$: C, 45.29; H, 2.28; N, 10.56. Found: C, 45.21; H, 2.30; N, 10.59.

Instrumentation

Cyclic voltammograms were recorded on a ALS Electrochemical Analyzer Model 612D with the three electrode system consisting of a platinum disc working electrode (φ = 3 mm), a platinum wire counter electrode, and an Ag/AgCl reference electrode in a benzonitrile (for NXz), dichloromethane (for NXz2T), or acetonitrile (for polymers) containing tetrabutylammonium hexafluorophosphate (0.1 M) at a scan rate of 100 mVs^{-1}. NXz and NXz2T were measured in solution and the polymers were measured in thin film. Polymer thin films were cast from DCB solutions on the ITO, which was then connected to the working electrode. All the potentials were calibrated with the half-wave potential of the ferrocene/ferrocenium redox couple measured under identical condition. Photoelectron spectra were recorded on a Model AC-2 photoelectron spectrometer (Riken Keiki Co., Ltd.) in air. Ionization potentials were determined from the onset potentials of the photoelectron spectra. UV-vis absorption spectra were recorded on a Shimadzu UV-3600 spectrometer. PL spectra were measured using a Quantaurus-QY absolute PL quantum yields measurement system (Hamamatsu Photonics). Differential scanning calorimetry (DSC) analysis was carried out with an EXSTAR DSC7020 (SII Nanotechnology, Inc.) at a cooling and heating rate of 10 °C min^{-1}.

Single crystal X-ray analysis

Single crystals of NXz2T for X-ray structural analysis were obtained by a physical vapor transport method.[46] The X-ray crystal structure analyses were made on a Rigaku R-AXIS RAPID (Cu Kα radiation,

$\lambda = 1.54187$ Å, graphite monochromator, $T = 93$ K). The structure was solved by the direct methods.[47, 48] Non-hydrogen atoms were refined anisotropically, and hydrogen atoms were included in the calculations but not refined. All calculations were performed using the crystallographic software package CrystalStructures 4.0.[48]

Crystallographic data for NOz2T: $C_{20}H_{12}N_4O_2S_2$ (404.46), red plate, $0.90 \times 0.20 \times 0.01$ mm^3, *monoclinic*, space group $P2$1/n, $a = 4.74630(10)$, $b = 10.0444(2)$, $c = 17.8813(3)$ Å, $\beta = 96.1637(13)°$, $V = 847.54(3)$ Å^3, $Z = 2$, $R = 0.0451$ for 1293 observed reflections ($I > 2\sigma(I)$) and 128 variable parameters, $wR2 = 0.1195$ for all data (1553).

Crystallographic data for NTz2T: $C_{20}H_{12}N_4S_4$ (436.58), red plate, $0.80 \times 0.50 \times 0.1$ mm^3, *monoclinic*, space group $C2$/c, $a = 11.7955(15)$, $b = 8.5619(9)$, $c = 18.814(2)$ Å, $\beta = 106.7224(13)°$, $V = 1819.7(4)$ Å^3, $Z = 4$, $R = 0.0398$ for 1576 observed reflections ($I > 2\sigma(I)$) and 128 variable parameters, $wR2 = 0.1123$ for all data (2068).

Crystallographic data for NSz2T: $C_{20}H_{12}N_4S_2Se_2$ (530.38), red plate, $0.80 \times 0.15 \times 0.01$ mm^3, *monoclinic*, space group $P2$1/n, $a = 8.8022(2)$, $b = 4.6030(10)$, $c = 22.6036(4)$ Å, $\beta = 90.6026(8)°$, $V = 915.77(3)$ Å^3, $Z = 2$, $R = 0.0364$ for 1540 observed reflections ($I > 2\sigma(I)$) and 128 variable parameters, $wR2 = 0.1057$ for all data (1657).

OFET fabrication and evaluation

OFET devices were fabricated in a bottom-gate-top-contact configuration on a heavily doped n$^+$-Si(100) wafer with 200-nm-thickness thermally grown SiO$_2$ ($C_i = 17.3$ nFcm^{-2}). The Si/SiO$_2$ substrates were ultrasonicated with water for three min thrice, and acetone and isopropanol for 5 min, respectively, and rinsed in boiled isopropanol for 10 min, and then were subjected to UV-ozone treatment for 30 min. The cleaned substrates were then treated by 1H,1H,2H,2H-perfluorodecyltriethoxysilane (FDTS) or octadecyltriethoxysilane (ODTS) as follows. For FDTS, the substrates were left in a Teflon container with several drops of FDTS and then the container was heated to 120 °C for 2h in the desiccator. The FDTS-

treated substrates were ultrasonicated with acetone and isopropanol for 5 min, respectively, and rinsed in boiled isopropanol for 10 min. For ODTS, a solution of ODTS in trichloroethylene (3 mM) was spin-coated onto the substrates at a rate of 3000 rpm for 15 sec followed by hydrolysis in a closed container in the presence of ammonia hydroxide solution for 24 h. After the hydrolysis, the substrates were rinsed with water, acetone and boiling isopropanol, respectively. In a glove box under nitrogen atmosphere, polymer thin films were spin-coated from hot DCB or CB/DCB mixed or CB/TCB mixed solutions (3 gL^{-1}) at 1000 rpm for 10 sec and then 2500 rpm for 35 sec. The polymer films were annealed at 200 ºC for 30 min under nitrogen. On top of the polymer thin films, gold drain and source contact electrodes (thickness: 80 nm) with the channel length and width of 40 μm and 1500 μm, respectively, were deposited in vacuum through shadow masks.

Current-voltage characteristics of the OFET devices were measured at room temperature under ambient conditions (relative humidity: 30~40%) with a Keithley 4200-SCS semiconductor parameter analyzer. Threshold voltages of the devices were estimated from the transfer plots by extrapolating the square root of the drain current to the horizontal axis. Hole and electron field-effect mobilities were extracted from the square root of the drain current in the saturation regime (V_d = –60 V) by using the following equation,

$$I_d = (WC_i/2L) \, \mu \, (V_g\text{-}V_{th})^2$$

where, L and W are channel length and width, respectively, and C_i is capacitance of the gate insulator. The average hole and electron mobilities and threshold voltages were obtained over more than 10 devices.

Materials for OPV

PC$_{61}$BM and PC$_{71}$BM were purchased from Frontier Carbon.

Solar cell fabrication and measurements

ITO substrates were pre-cleaned sequentially by sonicating in a detergent bath, de-ionized water, acetone, and isopropanol at room temperature, and in a boiled isopropanol bath, each for 10 min. Then, the substrates were subjected to UV/ozone treatment at room temperature for 20 min. The pre-cleaned ITO substrates masked at the electrical contacts were coated with ZnO precursor by spin coating (3000 rpm for 30 s) a precursor solution prepared by dissolving zinc acetate dehydrate (0.5 g) and ethanolamine (0.14 mL) in 5 mL of 2-methoxyethanol. They were then baked in air at 200 ºC for 30 min, rinsed with acetone and isopropanol, and dried in a glove box. The photoactive layers were deposited in a glove box (KOREA KIYON, KK-011AS-EXTRA) by spin coating: the CB solution containing 4–5 g L^{-1} of the polymer sample with respective amount of $PC_{71}BM$ was kept at 140 °C for 30 min, and the hot solution was directly spin-coated on the substrate at 600 rpm for 20 s. The thin films were transferred into a vacuum evaporator (ALS Technology, E-100J) connected to the glove box. MoO_x (7.5 nm) and Ag (100 nm) were deposited sequentially by thermal evaporation under $\sim 10^{-5}$ Pa, where the active area of the cells was 0.16 cm^2.

J–V characteristics of the cells were measured with a Keithley 2400 source measure unit in nitrogen atmosphere under 1 Sun (AM1.5G) conditions using a solar simulator (SAN-EI Electric, XES-40S1). The light intensity for the J–V measurements was calibrated with a reference PV cell (Konica Minolta AK-100 certified by the National Institute of Advanced Industrial Science and Technology, Japan). Temperature dependence of the J–V characteristics was measured with a direct-current voltage and current source/monitor (Advantest, R6243) in a vacuum prober system (ALS Technology, VPS3-50) under the illumination from a 100 W Xe lamp (Asahi Spectra, LAX-C100) equipped with a uniform illumination lens unit (Asahi Spectra, RLQL80-0.5). EQE spectra were measured with a spectral response measuring system (Soma Optics, Ltd., S-9241). The thickness of the active layer was measured with an AlphaStep® D-100 surface profiler (KLA Tencor).

Thin film characterization

2D GIXD experiments were conducted at SPring-8 on beamline BL46XU. The samples were irradiated with an X-ray energy of 12.39 keV (λ = 1 Å) at a fixed incident angle of 0.12° through a Huber diffractometer, and the GIXD patterns were recorded on a 2D image detector (Pilatus 300K). The samples were prepared under the same condition used for the OFET and OPV fabrication. The GIWAXD patterns were recorded with a two-dimensional image detector (Pilatus 300K). TEM measurements were performed using a JEOL JEM-1230 instrument. The blend films for the TEM measurement were prepared in the same manner as actual devices but on PEDOT:PSS-coated ITO substrates. Then, the substrates were transferred to TEM grids using the contact film-transfer method.[49, 50] AFM measurements were carried out with actual devices using a Nanocute scanning probe microsope system (SII Nanotechnology, Inc.).

4-6. References

1) Zhang, M.; Tsao, H. N.; Pisula, W.; Yang, C.; Mishra, A. K.; Müllen, K. *J. Am. Chem. Soc.* **2007**, *129*, 3472–3473.

2) Blouin, N.; Michaud, A.; Gendron, D.; Wakim, S.; Blair, E.; Neagu-Plesu, R.; Belletête, M.; Durocher, G.; Tao, Y.; Leclerc, M. *J. Am. Chem. Soc.* **2008**, *130*, 732–742.

3) Zhou, E.; Cong, J.; Hashimoto, K.; Tajima, K. *Macromolecules* **2013**, *46*, 763–768.

4) Mataka, S.; Takahashi, K.; Ikezaki, Y.; Hatta, T.; Tori-I, A.; Tashiro, M. *Bull. Chem. Soc. Jpn.* **1991**, *64*, 68–73.

5) Osaka, I.; Shimawaki, M.; Mori, H.; Doi, I.; Miyazaki, E.; Koganezawa, T.; Takimiya, K. *J. Am. Chem. Soc.* **2012**, *134*, 3498–3507.

6) Wang, M.; Hu, X.; Liu, P.; Li, W.; Gong, X.; Huang, F.; Cao, Y. *J. Am. Chem. Soc.* **2011**, *133*, 9638–9641.

7) Osaka, I.; Abe, T.; Shimawaki, M.; Koganezawa, T.; Takimiya, K. *ACS Macro Lett.* **2012**, 437-440.

8) Osaka, I.; Kakara, T.; Takemura, N.; Koganezawa, T.; Takimiya, K. *J. Am. Chem. Soc.* **2013**, *135*, 8834–8837.

9) Yang, T.; Wang, M.; Duan, C.; Hu, X.; Huang, L.; Peng, J.; Huang, F.; Gong, X. *Energy Environ. Sci.* **2012**, *5*, 8208–8214.

10) Liu, Y.; Zhao, J.; Li, Z.; Mu, C.; Ma, W.; Hu, H.; Jiang, K.; Lin, H.; Ade, H.; Yan, H. *Nat. Commun.* **2014**, *5*, 5293.

11) Kawashima, K.; Miyazaki, E.; Shimawaki, M.; Inoue, Y.; Mori, H.; Takemura, N.; Osaka, I.; Takimiya, K. *Polym. Chem.* **2013**, *4*, 5224–5227.

12) Vohra, V.; Kawashima, K.; Kakara, T.; Koganezawa, T.; Osaka, I.; Takimiya, K.; Murata, H. *Nat. Photon.* **2015**, *9*, 403–408.

13) Zhang, Z.; Lin, F.; Chen, H.-C.; Wu, H.-C.; Chung, C.-L.; Lu, C.; Liu, S.-H.; Tung, S.-H.; Chen, W.-C.; Wong, K.-T.; Chou, P.-T. *Energy Environ. Sci.* **2015**, *8*, 552–557.

14) Imai, K.; Kurihara, M.; Mathias, L.; Wittmann, J.; Alston, W. B.; Stille, J. K. *Macromolecules* **1973**, *6*, 158–162.

15) Matthews, J. R.; Niu, W.; Tandia, A.; Wallace, A. L.; Hu, J.; Lee, W.-Y.; Giri, G.; Mannsfeld, S. C. B.; Xie, Y.; Cai, S.; Fong, H. H.; Bao, Z.; He, M. *Chem. Mater.* **2013**, *25*, 782–789.

16) Kawabata, K.; Osaka, I.; Nakano, M.; Takemura, N.; Koganezawa, T.; Takimiya, K. *Adv. Electron. Mater.* **2015**, *DOI: 10.1002/aelm.201500039*.

17) Nakano, M.; Mori, H.; Shinamura, S.; Takimiya, K. *Chem. Mater.* **2012**, *24*, 190–198.

18) Nakano, M.; Niimi, K.; Miyazaki, E.; Osaka, I.; Takimiya, K. *J. Org. Chem.* **2012**, *77*, 8099–8111.

19) Nakano, M.; Shinamura, S.; Houchin, Y.; Osaka, I.; Miyazaki, E.; Takimiya, K. *Chem. Commun.* **2012**, *48*, 5671–5673.

20) Chen, Z.; Wannere, C. S.; Corminboeuf, C.; Puchta, R.; Schleyer, P. v. R. *Chem. Rev.* **2005**, *105*, 3842–3888.

21) Katritzky, A. R.; Jug, K.; Oniciu, D. C. *Chem. Rev.* **2001**, *101*, 1421–1450.

22) Bredas, J.-L. *Mater. Horiz.* **2014**, *1*, 17–19.

23) Rivnay, J.; Mannsfeld, S. C. B.; Miller, C. E.; Salleo, A.; Toney, M. F. *Chem. Rev.* **2012**, *112*, 5488–5519.

24) DeLongchamp, D. M.; Kline, R. J.; Jung, Y.; Lin, E. K.; Fischer, D. A.; Gundlach, D. J.; Cotts, S. K.; Moad, A. J.; Richter, L. J.; Toney, M. F.; Heeney, M.; McCulloch, I. *Macromolecules* **2008**, *41*, 5709–5715.

25) Rogers, J. T.; Schmidt, K.; Toney, M. F.; Kramer, E. J.; Bazan, G. C. *Adv. Mater.* **2011**, *23*, 2284–2288.

26) Kobayashi, S.; Nishikawa, T.; Takenobu, T.; Mori, S.; Shimoda, T.; Mitani, T.; Shimotani, H.; Yoshimoto, N.; Ogawa, S.; Iwasa, Y. *Nat Mater* **2004**, *3*, 317–322.

27) Veldman, D.; Meskers, S. C. J.; Janssen, R. A. J. *Adv. Funct. Mater.* **2009**, *19*, 1939–1948.

28) Wang, M.; Wang, H.; Yokoyama, T.; Liu, X.; Huang, Y.; Zhang, Y.; Nguyen, T.-Q.; Aramaki, S.; Bazan, G. C. *J. Am. Chem. Soc.* **2014**, *136*, 12576–12579.

29) King, R. R.; Bhusari, D.; Larrabee, D.; Liu, X.-Q.; Rehder, E.; Edmondson, K.; Cotal, H.; Jones, R. K.; Ermer, J. H.; Fetzer, C. M.; Law, D. C.; Karam, N. H. *Prog. Photovolt.: Res. Appl.* **2011**, *19*, 797–812.

30) Green, M. A.; Ho-Baillie, A.; Snaith, H. J. *Nat. Photon.* **2014**, *8*, 506–514.

31) Li, W.; Hendriks, K. H.; Furlan, A.; Wienk, M. M.; Janssen, R. A. J. *J. Am. Chem. Soc.* **2015**, *137*, 2231–2234.

32) Thompson, B. C.; Fréchet, J. M. J. *Angew. Chem. Int. Ed.* **2008***, 47*, 58–77.

33) Larson, B. W.; Whitaker, J. B.; Wang, X.-B.; Popov, A. A.; Rumbles, G.; Kopidakis, N.; Strauss, S. H.; Baltalina, O. V. *J. Phys. Chem.* **2013**, *C 117*, 14958–14964.

34) Scharber, M. C.; Mühlbacher, D.; Koppe, M.; Denk, P.; Waldauf, C.; Heeger, A. J.; Brabec, C. J. *Adv. Mater.* **2006**, *18*, 789–794.

35) Bredas, J.-L.; Norton, J. E.; Cornil, J.; Coropceanu, V. *Acc. Chem. Res.* **2009**, *42*, 1691–1699.

36) Shockley, W.; Queisser, H. J. *J. Appl. Phys.* **1961**, *32*, 510–519.

37) Jung, J.-W.; Liu, F.; Russell, T. P.; Jo, W.-H. *Energy Environ. Sci.* **2012**, *5*, 6857–6861.

38) Jung, J.-W.; Jo, J.-W.; Liu, F.; Russell, T. P.; Jo.W.-H. *Chem. Commun*. **2012**, *48*, 6933–6935.

39) Vandewal, K.; Ma, Z.; Bergqvist, J.; Tang, Z.; Wang, E.; Henriksson, P.; Tvingstedt, K.; Andersson, M. R.; Zhang, F.; Inganäs, O. *Adv. Funct. Mater.* **2012**, *22*, 3480–3490.

40) Ma, Z.; Wang, E.; Vandewal, K.; Andersson, M. R.; Zhang, F. *Appl. Phys. Lett.* **2011**, *99*, 143302.

41) Wang, E.; Ma, Z.; Zhang, Z.; Vandewal, K.; Henriksson, P.; Inganäs, O.; Zhang, F.; Andersson, M. R. *J. Am. Chem. Soc.* **2011**, *133*, 14244–14247.

42) Rivnay, J.; Mannsfeld, S. C. B.; Miller, C. E.; Salleo, A.; Toney, M. F. *Chem. Rev.* **2012**, *112*, 5488–5519.

43) Osaka, I.; Takimiya, K. *Polymer* **2015**, *59*, A1–A15.

44) Huang, Y.; Kramer, E. J.; Heeger, A. J.; Bazan, G. C. *Chem. Rev.* **2014**, *114*, 7006–7043.

45) Seitz, D. E.; Lee, S.-H.; Hanson, R. N.; Bottaro, J. C. *Synth. Commun.* **1983**, *13*, 121–128.

46) Laudise, R. A.; Kloc, C.; Simpkins, P. G.; Siegrist, T. *J. Cryst. Growth*. **1998**, 187, 449–454.

47) SHELXL (SHELX97): G. M. Sheldrick Programs for the refinement of crystal structures. University of Goettingen, Germany, **1997**.

48) CrystalStructure. Version 4.0., Rigaku Corporation, Tokyo, Japan, **2011**.

49) Wei, Q.; Tajima, K.; Hashimoto, K. *ACS Appl. Mater. Interfaces* **2009**, *1*, 1865–1868.

50) Tada, A.; Geng, Y.; Wei, Q.; Hashimoto, K.; Tajima, K. *Nat. Mater.* **2011**, *10*, 450–455.

Chapter 5

Concluding Remarks

In previous chapters, I have shown the improvement of photovoltaic properties of polymer-based solar cells through materials development using naphthobischalcogenadiazole (NXz) and device engineering.

In chapter 2, I demonstrated that single junction solar cells of PNTz4T with an inverted architecture afforded PCEs as high as 10.1%, where the active layer thickness was ~300 nm, which is two to three times as thick as that for the typical OPVs. This is most likely due to the high crystallinity and the face-on orientation that PNTz4T formed in the films blended with PCBM, resulting in higher J_{SC} without a loss of FF. The improved performance on inverted cells is probably due to the large population of polymer crystallites with a face-on orientation and the favorable distribution of edge-on and face-on crystallites along the film thickness, which results in a reduction in charge recombination and efficient charge transport.

In chapter 3, I introduced fluorine atoms on the polymer backbone, the bithiophene moiety, of PNTz4T. The fluorinated polymers, PNTz4TF2 and PNTz4TF4 exhibited both deeper HOMO and LUMO energy levels than PNTz4T. Improved PCEs, compared to PNTz4T cells, of up to 10.5% was observed in PNTz4TF2 cells.

In chapter 4, I synthesized an oxygen and a selenium analogues of PNTz4T, namely, PNOz4T and PNSz4T. Clear correlations between the chalcogen atom and the properties of the corresponding polymers were observed. PNOz4T with a narrow bandgap of 1.52 eV led to high V_{OC} of ~1V and high PCE of ~9%, resulting in photon energy loss as small as ~0.5 eV, which is much smaller than that of typical polymer systems (0.7-1.0 eV).

In this thesis, I synthesized a series of semiconducting polymers using NXz, which provided several unconventional properties (narrow E_g, deep HOMO level, high crystallinity and face-on orientation at the same time). The use of the polymers in OPVs, together with careful device engineering, demonstrated one of the highest performances in the OPV area. I found that high efficiency have been achieved using a

thick active layer measuring (∼300 nm), which is far thicker than the typical thickness for OPVs and is beneficial for practical use. In addition, no solvent additives, such as 1,8-diiodooctane or 1-chloronaphthalene, were indeed necessary for optimizing the cell properties. These results are most probably due to the highly ordered polymer structure in the active layer, in which a highly crystalline structure with short π–π stacking distance and the favorable face-on orientation are achieved. I also found that the photon energy loss, an inherent issue in OPVs, can be solved, and that the charges can be generated beyond the working principle.

I believe that these insightful findings regarding the HOMO–LUMO control of polymer by design would open the door to the realization of both high J_{SC} and V_{OC} at the same time in OPVs. This thesis will contribute to the further advance of organic photovoltaics in the near future.

List of Publications

(1) "5,10-Diborylated naphtho[1,2-*c*:5,6-*c'*]bis[1,2,5]thiadiazole: a ready-to-use precursor for the synthesis of high-performance semiconducting polymers"

<u>Kazuaki Kawashima</u>, Eigo Miyazaki, Masafumi Shimawaki, Yuki Inoue, Hiroki Mori, Noriko Takemura, Itaru Osaka and Kazuo Takimiya, *Polym. Chem.*, **2013**, *4*, 5224–5227.

(2) "Efficient inverted polymer solar cells employing favourable molecular orientation"

Varun Vohra, <u>Kazuaki Kawashima</u>, Takeshi Kakara, Tomoyuki Koganezawa, Itaru Osaka, Kazuo Takimiya and Hideyuki Murata, *Nat. Photon.*, **2015**, *9*, 403–409.

(3) "Effect of Chalcogen Atom on the Properties of Naphthobischalcogenadiazole-Based π-conjugated Polymers"

<u>Kazuaki Kawashima</u>, Itaru Osaka and Kazuo Takimiya, *Chem. Mater.*, **2015**, *27*, 6558–6570.

(4) "High-efficiency polymer solar cells with small photon energy loss"

<u>Kazuaki Kawashima</u>, Yasunari Tamai, Hideo Ohkita, Itaru Osaka and Kazuo Takimiya, *Nat. Commun.*, **2015**, *6*, 10085.

Other papers not included in this thesis

(5) "Selective Substitution of Hex_2SiFC1 for the Preparation of Polymers with Two Different Alternate π-Electron Systems Linked by Hex_2Si Units"

Joji Ohshita, <u>Kazuaki Kawashima</u>, Arihiro Iwata, Heqing Tang, Miho Higashi and Atsutaka Kunai, *Z. Naturforschung, B,* **2004**, *59*, 1332–1336.

Acknowledgements (謝辞)